Spin-orbit optomechanics of space-variant birefringent media

Davit Hakobyan

université de BORDEAUX

SWINBURNE UNIVERSITY OF TECHNOLOGY

THÈSE EN COTUTELLE

Présentée pour obtenir le grade de

DOCTEUR
DE L'UNIVERSITÉ DE BORDEAUX
ET DE L'UNIVERSITÉ DE TECHNOLOGIE DE SWINBURNE

ÉCOLE DOCTORALE DES SCIENCES PHYSIQUES DE L'INGÉNIEUR

FACULTÉ DES SCIENCES, DE L'INGÉNIERIE ET TECHNOLOGIE

SPÉCIALITÉ : LASER, MATIÈRE ET NANOSCIENCES

Par

Davit HAKOBYAN

Sujet :

Spin-orbit optomechanics of space-variant birefringent media

Soutenue le 15 juin 2016 devant la Commission d'examen :

Mme PRUVOST, Laurence	Directrice de recherche	Présidente
M. GUILLON, Marc	Maître de conférences	Rapporteur
M. LAI, Ngoc Diep	Maître de conférences	Rapporteur
M. GLÜCKSTAD, Jesper	Professeur des universités	Examinateur
M. BRASSELET, Etienne	Chargé de recherche	Directeur de thèse
M. JUODKAZIS, Saulius	Professeur des universités	Co-Directeur de thèse

À mes parents
Amur et Susanna

Acknowledgments

First all, I would like to express my sincere appreciation to Etienne Brasselet, who initiated and supervised my doctoral studies carried in Laboratoire Ondes et Mati‘ere d'Aquitaine, CNRS, University of Bordeaux. I admire his scientific aptitudes and abilities and skills to create a very singular team I had pleasure to be a part of. I express my gratitude to him for his kindness and valuable advises. Special thanks for transferring me an experimental touch and rigor.

Equally, I express my deep appreciation to Saulius Juodkazis who co-supervised the research carried in joint agreement with Swinburne University of Technology. Special thanks for providing a warm welcome in Centre of Micro-Photonics and for all his supportive instructs.

I express my gratitude to Marc Guillon and Ngoc Diep Lai for kindly accepting to be reporter of this manuscript, thanks for your detailed reports. I express my appreciation to Jesper Glückstad and Laurence Pruvost for accepting me to be examiners for the manuscript. Thanks to all the jury members for their attention and interest for this work, in particular thanks for the elaborated questions and comments during the defense.

I would like also to take this opportunity to thank to all coauthors who have contributed in the carried research and related publications, it was a great pleasure to work with them. Equally, I thank all my team members for kindly sharing equipment and time with me. As well as I express my thankfulness to the administrative, mechanical and electronic staff of Bordeaux University and Swinburne University of Technology for their benevolent and professional attitude. Let me also thank to my friends and family for their perpetual support.

This study has been carried out with financial support from the French State, managed by the French National Research Agency (ANR) in the frame of the investments for the future Programme IdEx Bordeaux– reference ANR-10-IDEX-03-02; I express my gratefulness to all involved people.

Declaration

I, Davit HAKOBYAN, declare that this thesis titled, **"Spin-orbit optomechanics of space-variant birefringent media"** is my own work conducted under supervision of Dr. Etienne BRASSELET and Prof. Saulius JUODKAZIS. I confirm that:

- Thesis contains no material which has been accepted for the award to the candidate of any other degree or diploma, except where due reference is made.
- Thesis contains contains no material previously published or written by another person except where due reference is made, which is always clearly attributed.
- Where the work is based on joint research or publications, discloses the relative contributions of the respective workers or authors.

Davit HAKOBYAN
Laboratoire Ondes et Matière d'Aquitaine (UMR5798),
Université de Bordeaux, CNRS
351 Cours de la Libération
33405 Talence
FRANCE
Centre for Micro-Photonics
Faculty of Science, Engineering and Technology
Swinburne University of Technology
John St, Hawthorn VIC 3122
AUSTRALIA
Date: 15th, June, 2016

Titre : Optomécanique des milieux biréfringents inhomogènes pilotée par l'interaction spin-orbite de la lumière

Résumé : Ce travail consiste en l'étude de phénomènes optomécaniques en d'interaction spin-orbite de la lumière, en utilisant des milieux inhomogènes et anisotropes comme systèmes modèles, différents types de systèmes matériels étant considérés en pratique. En particulier, nous avons utilisé des défauts de cristaux liquides nématiques pour lesquels nous avons identifié expérimentalement d'un couple optique de nature spin-orbite conduisant à des modifications de champ d'orientation moléculaire du cristal liquide. Aussi, grâce à l'utilisation de verres nanostructurés artificiellement permettant un contrôle de l'interaction spin-orbite à la demande, nous mettons en évidence un phénomène de couple optique inverse qui est l'analogue angulaire des forces optiques dites négatives. Cet effet optomécanique contre-intuitif est démontré expérimentalement, d'une manière indirecte, grâce à la mise en place de diverses expériences de décalage en fréquence Doppler associées aux degrés de liberté de rotation. Enfin, nous présentons nos tentatives en vue de réaliser expérimentalement l'observation directe d'un couple optique inverse. Plusieurs options sont envisagées, qui comprennent à la fois des approches à base de matériaux métalliques ou diélectriques. De manière générale, cela implique la miniaturisation des systèmes considérés, ce qui est effectué à la fois à l'échelle millimétrique et micrométrique.

Mots clés : Moment angulaire de la lumière, Vortex optiques, Interaction spin-orbite de la lumière, Optomécanique, Milieux anisotropes et inhomogènes, Cristaux liquides, Nanofabrication

---

Title: Spin-orbit optomechanics of space-variant birefringent media

Abstract: This work focuses on angular optomechanics driven by the spin-orbit interaction of light, using inhomogeneous and anisotropic media as model systems and different kinds of such material systems are considered in practice. In particular, we use nematic liquid crystal defects and report on the direct experimental observation of spin-orbit optical radiation torque that leads to distortion of molecular orientation pattern of the defects. Then, by using solid-state spin-orbit couplers of arbitrary order made of artificially nanostructured glasses, we unveil an optical torque reversal phenomenon that is the angular counterpart of so-called optical negative forces. This counterintuitive optomechanical effect is experimentally retrieved, in an indirect manner, via rotational Doppler frequency shift experiments. Finally, we report on our attempts to build up an experimental framework allowing the direct observation of optical torque reversal. Several options are considered, which include both metallic and dielectric approaches and involve sample miniaturization that has been explored at the millimeter and micrometer scale.

Keywords: Optical angular momentum, Optical vortices, Spin-orbit interaction of light, Optomechanics, space-variant anisotropic media, Liquid crystals, Nanofabrication

---

Unité de recherche

Labartoire Ondes et Matiére d'Aquitaine (UMR 5798), Université de Bordeaux, PAC Talence Bât A4, 351 Cours de la Libération, 33405 Talence cédex, France

Centre for Micro-Photonics (H74), Swinburne University of Technology, John Street PO Box 218 Hawthorn, VIC, 3122 Australia

Résumé en français

Cette thèse est dédiée à l'optomécanique angulaire par l'interaction entre une lumière structurée et une matière structuré. Dans le chapitre 1, nous présentons les principaux éléments de notre étude. À savoir, dans la partie 1.1 nous introduisons la notion de moment angulaire de la lumière qui a deux contributions distinctes : une partie "spin" associée au degré de liberté de polarisation de la lumière, et une partie "orbitale" associée à la distribution spatiale des degrés de liberté de la lumière. Nous présentons également les conditions dans lesquelles ces deux sortes de moments angulaires sont transférées à la matière. Dans la partie 1.2 nous démontrons comment les moments angulaires orbital et de spin interagissent entre eux lorsque la lumière se propage à l'intérieur d'un matériau aux propriétés optiques anisotropes et non homogènes. Ces intéractions, dites "intéractions spin-orbite" de la lumière, a des conséquences tant sur le champ lumineux lui même que sur la matière. En particulier, nous discutons de la génération de vortex optique piloté par l'intéraction spin-orbite avec des éléments biréfringent non homogène azimutalement et revoyons les diverses approches de structurations possibles de matériaux qui ont été élaborés au cours de la dernière décennie. D'autre part, dans la partie 1.3 nous voyons les conséquences mécaniques possibles de l'interaction spin-orbit optique. Tout ceci établit le contexte scientifique de ce travail dont les motivations principales et le plan sont présentés dans la partie 1.4.

Dans le chapitre 2, nous présentons une manifestation mécanique expérimentale : l'intéraction spin-orbite induit un couple optique dans le faisceau. Nous définissons nos exigences pour l'observation de ce couple dans la partie 2.1, où nous discutons du choix du milieu de couplage spin-orbite et de ses conditions d'observation. En particulier, nous présentons les défauts de type ombilics présents dans les couches de cristaux liquides nématiques, qui ont l'avantage de former spontanément un milieu biréfringent dont l'axe optique présente une structuration azimutale. Dans la

partie 2.2 nous présentons les principes de notre étude et proposons d'évaluer notre analyse expérimentale grâce à la manipulation de la biréfringence du cristal liquide par le champ électrique. Ensuite nous présentons le changement d'orientation moléculaire du cristal liquide provoqué par l'interaction spin-orbite de la lumière, soit une observation directe des effets optomécaniques de l'interaction spin-orbite. Plus précisément nous étudions l'orientation moléculaire des défauts de cristaux liquides de charge topologique $m = \pm 1$, en fonction de l'état de polarisation du faisceau incident et de la pureté du vortex optique généré. Enfin dans la partie 2.3, nous présentons nos tentatives en vue d'ouvrir nos recherches sur d'autres charges topologiques, $m \neq \pm 1$, en utilisant d'autres types de défauts de cristaux liquides appelés disclinations.

Dans le chapitre 3 nous élargissons l'étude des propriétés optomécanique spin-orbite aux défauts de charges topologiques $|m| \neq 1$ en utilisant des lames de verre structurées artificiellement par laser femtoseconde. De telles lames peuvent être trouvées dans le commerce ou être conçues spécifiquement pour obtenir toute charge topologique. Nous avons choisi de limiter notre étude aux charges topologiques $m = \{1/2, 1, 3/2\}$, avec un retard de phase biréfringent homogène $\Delta = \pi$. En effet ce choix nous permet d'aborder le couple optique inverse en passant d'une charge topologique $m = 1/2$ à $m = 3/2$, à moment angulaire optique de spin incident fixé. Dans la partie 3.1 nous introduisons le concept de couple optique "gauche" et établissons une analogie avec les forces optiques dites "négatives". Ensuite nous présentons les lames de phase biréfringentes et notre approche expérimentale pour mettre en évidence le couple gauche à partir d'un faisceau polarisé circulairement dans la partie 3.2. Puis, dans la partie 3.3, nous présentons une démonstration expérimentale basée sur la figure d'interférence entre deux faisceaux (un colinéaire l'autre non) et analysons le couple quantitativement et sa dépendance à tous les paramètres concernés. Dans la partie 3.4 nous présentons une approche expérimentale simplifiée avec un unique faisceau polarisé linéairement. Enfin, nous généralisons le couple gauche aux valeurs de retard de phase de biréfringence et états de polarisation incident arbitraires dans la partie 3.5.

Dans le chapitre 4 nous présentons les essais expérimentaux d'observation du couple optique gauche de façon directe. Dans la partie 4.1 nous discutons de potentielles méthodes d'amélioration pour l'évaluation de la rotation des éléments

optiques d'intéraction spin-orbite induite par le couple optique. Nous présentons nos essais expérimentaux sur des échantillons de structuration azimutale de la biréfringence à l'échelle millimétrique dans la partie 4.2, correspondant à une miniaturisation des échantillons macroscopiques utilisés précédemment. Ensuite, dans la partie 4.3, nous présentons le design, la fabrication et caractérisation de la structuration de micro-structures métalliques qui pourraient être de nouveaux candidats dans notre projet. Les performances optiques des échantillons fabriqués sont expérimentalement évaluées et discutées pour une potentielle implémentation optomécanique. Nous concluons ce chapitre par la partie 4.4, où nous ouvrons une option d'échantillon purement diélectrique à échelle micrométrique qui serait probablement celui qui permettrait une observation directe du couple optique inverse. Nous faisons état de nos premières tentatives de fabrication et des difficultés à prévoir en pratique auxquelles il faudra tenir compte afin d'atteindre l'objectif initial.

Contents

CHAPTER 1

Light angular momenta and their interaction

The thesis is dedicated to angular optomechanics in the presence of interplay between structured light and structured (space-variant) matter. In this chapter, we present the primary ingredients of our study. Namely, in section 1.1 we introduce the angular momentum of light that has two distinct contributions: a "spin" part associated with the polarization degree of freedom of light, and an "orbital" part associated with the spatial degrees of freedom of light. We also introduce the conditions under which these two kinds of angular momentum are transferred to matter. In section 1.2 we demonstrate how the optical spin and orbital angular momenta can interact as light propagates inside optically inhomogeneous and anisotropic media. Such so-called "spin-orbit interaction" of light has consequences, both on the light field itself and on matter. Particularly, we discuss the spin-controlled generation of optical vortices using azimuthally varying birefringent elements and review the various material structuring approaches that have been developed during the last decade. On the other hand, in section 1.3 we overview possible mechanical consequences of optical spin-orbit interaction. All this sets the background of this work, whose main motivations and outlines are summarized in section 1.4.

1.1 Light angular momenta and its transfer to matter

A light field is described either as an electromagnetic wave or as quantized particles, the photons. It is characterized by speed of light c, wavelength λ, wavevector

spectrum[1] $\{\mathbf{k}\}$ and its associated amplitude, phase, and polarization distributions. A plane wave, with wavevector $\mathbf{k}$ and angular frequency ω, propagating in free space carries $\hbar\omega$ energy and $\hbar\mathbf{k}$ linear momentum per photon. This holds too for light beams whose wavevector spectrum is not too broad, in other words in the limit of the paraxial approximation. Paraxial approximation assumes that spatial variations of the light field take place over distances that are large enough with respect to wavelength $\lambda = 2\pi/k$, (see for example Ref. [1]). Mathematically it can be expressed by inequalities

$$\frac{\partial A}{\partial z} \ll kA \qquad \frac{\partial^2 A}{\partial z^2} \ll k^2 A\,, \tag{1.1}$$

where A is the field amplitude and z is spatial coordinate along the propagation direction of the wave.

Besides energy and linear momentum, light may also carry angular momentum that consists of two contributions: spin angular momentum related to the polarization state and orbital angular momentum related to the spatial properties of the light. Indeed, careful examination of the angular momentum reveals that there are two types of rotations involved in light fields: one is linked to the vectorial nature of the field (polarization) and the other is linked to the optical phase spatial distribution. In particular, under the paraxial approximation, the spin and orbital angular momentum can be formally separated i.e., the total angular momentum can be expressed as the sum of spin and orbital angular momentum. In addition, when light field interacts with matter it may transfer its angular momentum to it. We discuss the above issues hereafter.

1.1.1 Spin angular momentum

Let us consider a fully polarized monochromatic plane wave with angular frequency ω and wavevector k propagating in vacuum along the z axis, with $(\mathbf{x}, \mathbf{y}, \mathbf{z})$ the orthonormal Cartesian basis. The complex electric field lies in $(\mathbf{x}, \mathbf{y})$ plane and is described by

$$\mathbf{E} = E_0 e^{-i(\omega t - kz)}\,\mathbf{e}\,, \tag{1.2}$$

[1] Referring to its plane waves content.

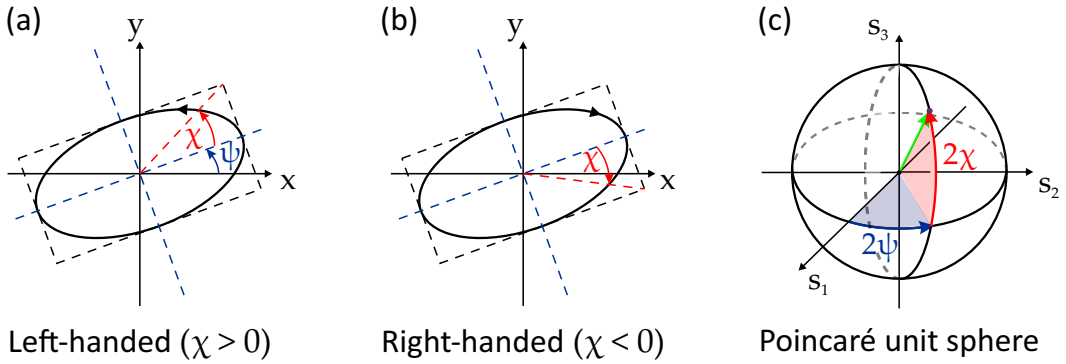

FIGURE 1.1: (a) Left- ($\chi > 0$) and (b) right- ($\chi < 0$) handed polarization ellipses. (c) Geometrical representation of fully polarized light identified by ψ and χ angles on the Poincaré unit sphere with the reduced Stokes parameters (s_1, s_2, s_3) as axes.

where E_0 is the amplitude and $\mathbf{e}$ is a unit vector that represents the polarization state. In general, $\mathbf{e}$ is a complex vector that can be described as

$$\mathbf{e} = (\cos\psi\cos\chi - i\sin\psi\sin\chi)\mathbf{x} + (\sin\psi\cos\chi + i\cos\psi\sin\chi)\mathbf{y}\,, \tag{1.3}$$

where ψ and χ angles are linked to the so-called polarization ellipse. Polarization ellipse refers to the curve described by the tip of the electric vector of electromagnetic field as time goes by, at a given point in space. The polarization ellipse is defined by two angles: (i) the azimuth angle ψ between its major axis and the $\mathbf{x}$ axis[2], and (ii) the ellipticity angle χ, $\tan\chi$ being the signed ratio between minor and major axes of polarization ellipse, as illustrated Fig. 1.1(a). We opt for the convention that labels polarization state as left-handed (respectively right-handed) when the tip of the electrical vector describes an ellipse that rotates counterclockwise (respectively clockwise) when observer looks at the source; i.e. $0 < \chi \leq \pi/4$ and $-\pi/4 \leq \chi < 0$, respectively (see Fig. 1.1(a,b)). Such convention is consistent with helix handedness that is formed with electrical vector and propagation direction at any given instant, $\mathbf{E}(\mathbf{r}, t_0)$ (see Fig. 1.2).

[2]This implies that angles ψ and $\psi + \pi$ are equivalent.

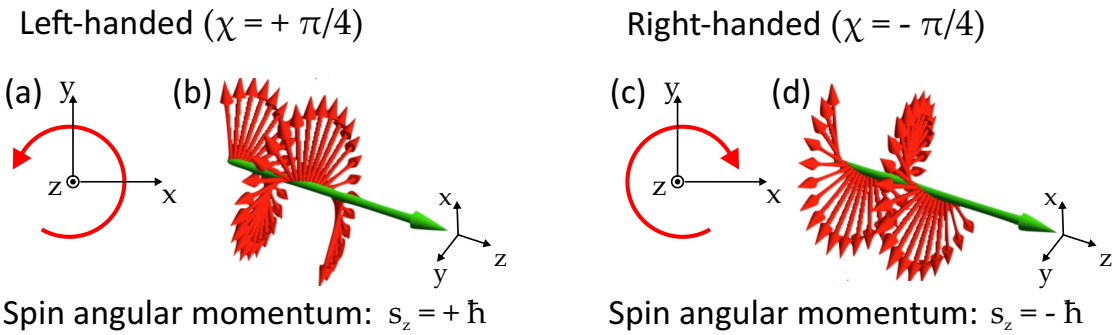

FIGURE 1.2: (a) Illustration of counterclockwise rotation (observer looks at the source) of the electric field vector tip in a plane transverse to the propagation direction given by z axis and (b) snapshot of the electrical field vector left-handed helix corresponding to left-handed circular polarization state. (c,d) Same as (a,b) for right-handed circular polarization state.

A practical representation of the polarization state is given by the Stokes vector $\mathbf{S} = (S_0, S_1, S_2, S_3)$ defined following (see Ref. [2])

$$\begin{aligned} S_0 &= |E_x|^2 + |E_y|^2 \,, \\ S_1 &= |E_x|^2 - |E_y|^2 \,, \\ S_2 &= 2\mathrm{Re}(E_x^* E_y) \,, \\ S_3 &= 2\mathrm{Im}(E_x^* E_y) \,. \end{aligned} \tag{1.4}$$

Then, introducing the reduced Stokes vector $\mathbf{s} = (S_1, S_2, S_3)/S_0$, any polarization state can be univocally associated with a point on the surface of the unit sphere, in the frame (s_1, s_2, s_3), called the Poincaré sphere. Indeed, the polarization state coordinates on the Poincaré sphere are (Fig. 1.1 (c))

$$\begin{aligned} s_1 &= \cos 2\psi \, \cos 2\chi \,, \\ s_2 &= \sin 2\psi \, \cos 2\chi \,, \\ s_3 &= \sin 2\chi \,. \end{aligned} \tag{1.5}$$

The equatorial line of the Poincaré sphere, $\chi = 0$, represents linearly polarized light with all possible azimuth angles, the "north" and "south" poles represent left and right circular polarization states $\chi = \pm\pi/4$, and all other points refer to elliptical polarization state.

Another representation of the polarization state of light is the one of Jones. It introduces unit vectors to describe an arbitrary polarization state. In the (x, y) basis the Jones representation of a polarization state, defined by angles ψ and χ, is expressed as

$$\mathbf{e} = \begin{pmatrix} \cos\psi\cos\chi - i\sin\psi\sin\chi \\ \sin\psi\cos\chi + i\cos\psi\sin\chi \end{pmatrix}. \tag{1.6}$$

the Jones representation is particularly useful when analyzing polarization changes as light passes through optical elements. Namely, the action of an optical element on polarization can be described by 2×2 matrix.

Regardless of the polarization state representation when the electric vector of light field rotates, polarized light carries well defined spin angular momentum, which can be related to the polarization state, more precisely to the third Stokes parameter. This was unveiled in 1909 by Poynting with the analogy of the wave motion of rotating shaft [3]. Indeed, in general, spin angular momentum projection on the field propagation direction is $s_z = s_3\hbar$ per photon, $\hbar = h/2\pi$ being the reduced Plank's constant. In particular $s_z = \sigma\hbar$, $\sigma = \pm 1$, for circular polarization, as illustrated in Fig. 1.2. Importantly, circular polarization states form an orthonormal basis to describe polarization, and this is a prime choice in this work, where we will refer to circular polarization Jones vectors as

$$\mathbf{e}_\sigma = \frac{1}{\sqrt{2}} \begin{pmatrix} 1 \\ i\sigma \end{pmatrix}. \tag{1.7}$$

1.1.2 Orbital angular momentum

Besides the intrinsic spin contribution to angular momentum that is related to the polarization, there is a contribution related to the spatial distribution of phase and referred as orbital angular momentum. To describe it, plane wave is no longer an appropriate tool. Instead, a beam (finite spatial extent) should be considered. This can be done in a general manner in the framework of paraxial approximation, by exploring a complete basis of solutions of the paraxial Helmholtz equation. Different options are possible, and in order to discuss an orbital angular momentum of an intrinsic nature [4], it is relevant to choose Laguerre-Gaussian basis. Indeed, any polarized light beam that propagates along z axis can be described in

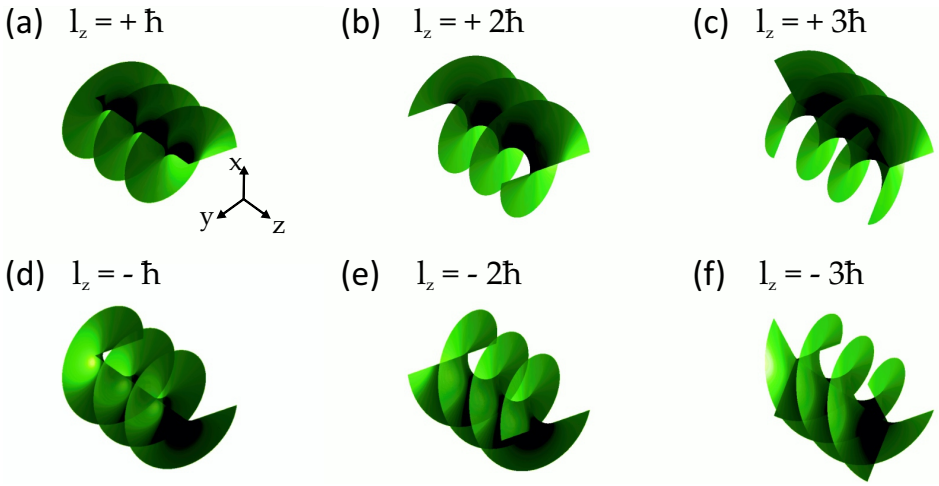

FIGURE 1.3: Illustration of surfaces of constant phase (wavefronts) corresponding to waves that carry on-axis phase singularities with topological charge $\ell = \pm 1$ (a,d), $\ell = \pm 2$ (b,e) and $\ell = \pm 3$ (c,f) and associated orbital angular momentum projections along the propagation direction, $l_z = \ell\hbar$ per photon.

Laguerre-Gaussian basis as

$$\mathbf{E} = \sum_{\ell,p,\sigma} E_0^{(\ell,p)} u_{\ell,p}(r,z) e^{i\ell\varphi} e^{-i(\omega t - kz)} \mathbf{e}_\sigma \,, \tag{1.8}$$

where,

$$\begin{aligned} u_{\ell,p}(r,z) = \frac{w_0}{w(z)} \left[\frac{r}{w(z)}\right]^{|\ell|} \exp\left[-\frac{r^2}{w^2(z)}\right] L_p^{|\ell|}\left(\frac{2r^2}{w^2(z)}\right) \\ \exp\left[\frac{ikr^2 z}{2(z^2+z_{\mathrm{R}}^2)}\right] \exp\left[-i(2p+|\ell|+1)\zeta(z)\right] \,, \end{aligned} \tag{1.9}$$

where, $w(z) = w_0\sqrt{1+(z/z_R)^2}$ is the beam radius at z, w_0 being beam waist at $z = 0$, $z_R = \pi w_0^2/\lambda$ is the Rayleigh distance, λ being the wavelength, $\zeta(z) = \arctan(z/z_R)$ is the Gouy phase for the Gaussian field, and $L_p^{|\ell|}$ are the generalized Laguerre polynomials with the radial index p and the azimuthal index is ℓ.

The choice of beam description is justified by noting that[3] Allen and coauthors [5] unveiled that beams with amplitude proportional to $\exp(i\ell\varphi)$ carry $\ell\hbar$ orbital

[3]Taking into account the convention adopted here for the complex representation of the electric field.

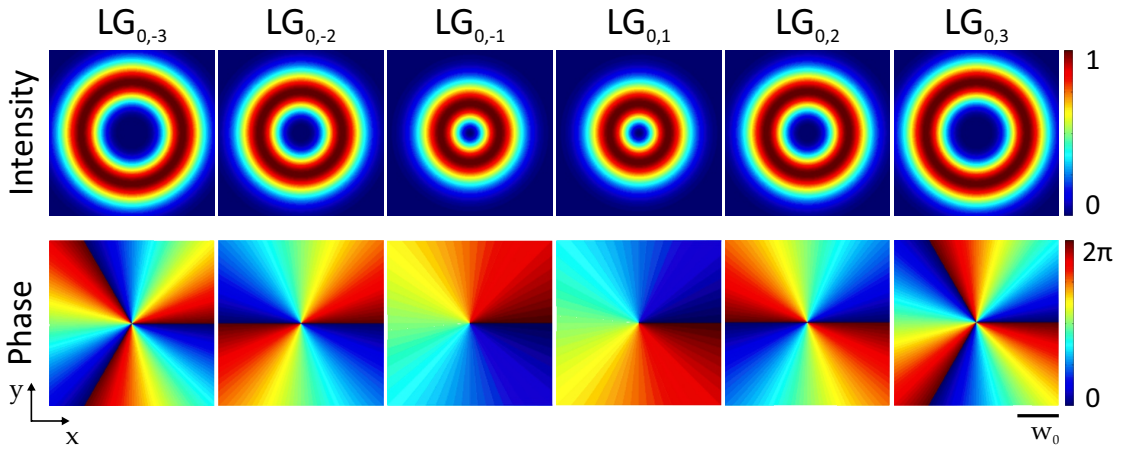

FIGURE 1.4: Normalized intensity and phase transverse distributions of fundamental Laguerre-Gaussian profiles observed in the transverse plane at $z = 0$ for the values $\ell = \{\pm 1, \pm 2, \pm 3\}$ and $p = 0$.

angular momentum per photon along the beam axis, where ℓ is an integer and φ is the polar angle in the plane orthogonal to the beam propagation direction. The $\exp(i\ell\varphi)$ factor indicates that the phase varies by $2\pi\ell$ along a closed circle around the beam axis in a transverse plane. However, at $r = 0$ (the center of the beam), the phase is undefined, referring to it as optical singularity of topological charge ℓ, which implies that the amplitude of the transverse field is null on axis in order to preserve field well defined. In general, beams endowed with phase singularities are called optical vortex beams. Such beams are widely explored in the domain of so-called singular optics that encompass the study of singularities of electromagnetic field [6]. Corresponding equiphase surfaces (wavefronts) are helicoids that revolve clockwise or counterclockwise depending on the sign of the ℓ as illustrated in Fig. 1.3 for the $\ell = \{\pm 1, \pm 2, \pm 3\}$. Note that left-handed (respectively right-handed) helicoid corresponds to the positive (respectively negative) values of the ℓ.

In our study we consider the Laguerre-Gaussian beams with zero radial index number $p = 0$. The intensity and phase transverse distributions of Laguerre-Gaussian beams are shown in Fig. 1.4 for $p = 0$ and $\ell = \{\pm 1, \pm 2, \pm 3\}$. Doughnut shaped intensity transverse distributions result from on-axis phase singularity are valid at any propagation distance and straightforward to observe in practice. On the other hand singular phase structure is generally assessed experimentally

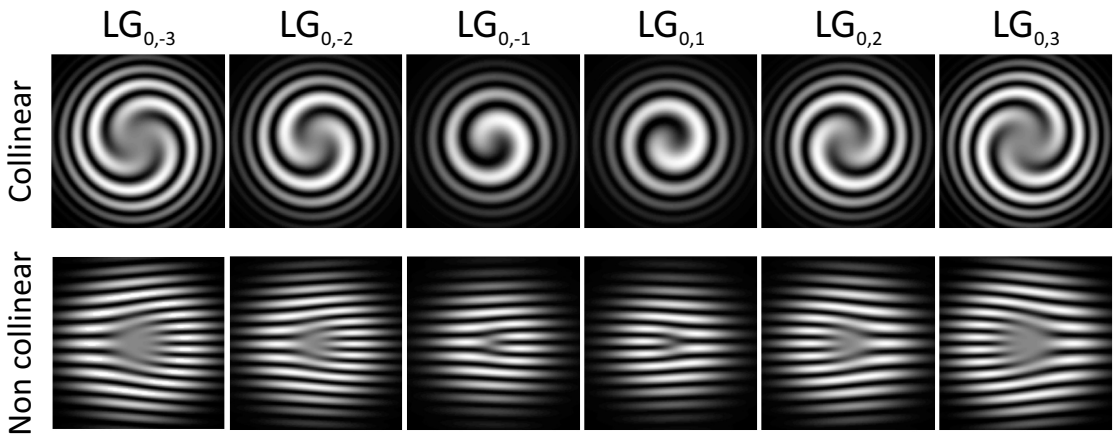

FIGURE 1.5: ℓ-arm spiraling (ℓ-fork fringing) interference patterns revealing the presence of on-axis optical phase singularity, obtained with on-axis (off-axis) coherent superposition of vortex beam with reference Gaussian beam of equivalent beam diameter and power at observation plane for the values of $\ell = \{\pm 1, \pm 2, \pm 3\}$ and $p = 0$.

by indirect observations using interferometry. A practical example consists to superpose a vortex beam with a collinear and coherent reference Gaussian beam. This leads to spiraling pattern, as illustrated in first row of Fig. 1.5, whose number of spiraling arms is equal to $|\ell|$, while their handedness is associated with the sign of ℓ. Importantly, the handedness of spiraling arm for a given ℓ also depends on the relative sign of wavefront curvature of superposed vortex and reference Gaussian beams. Note that to form such pattern relative wavefront curvature between two beams is required. Another example is non-collinear superposition of vortex and reference Gaussian beam that leads to non-axisymmetric fringing pattern formation referred as ℓ-fork pattern, as illustrated in second row of Fig. 1.5. The "fork" slits number is equal to the $|\ell|$, while its direction is associated with the sign of ℓ. Importantly, the pattern handedness depends on the geometry of non collinear superposition, and the straightness of fringes depends on plane-wave-like profiles (smooth curvature) of the superposed beams.

1.1.3 Angular momentum transfer to matter

As said above, in the limit of the paraxial approximation, the total angular momentum of light field along the propagation axis z, j_z, may be formally divided to the sum of two contributions [5], spin and orbital angular momentum parts. In

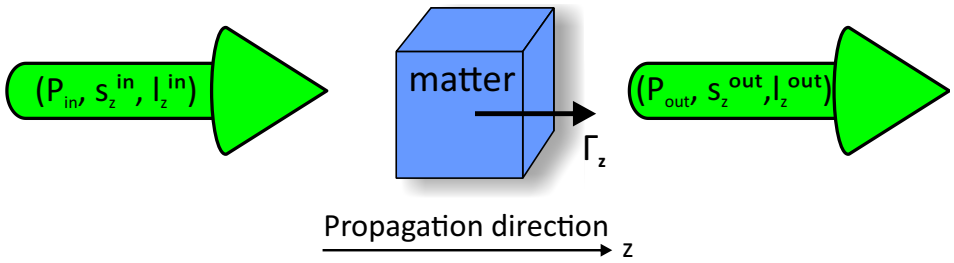

FIGURE 1.6: Illustration of general light-matter interaction process involving angular momentum exchanges, which results in torque exerted by light on matter.

the case of Laguerre-Gaussian beam with azimuthal axis index ℓ it can be expressed by the following form

$$j_z = s_z + l_z \,, \tag{1.10}$$

where $s_z = \sin(2\chi)\hbar$ and $l_z = \ell\hbar$ are respectively optical spin and orbital angular momentum per photon [7]. In what follows we focus on the mechanical consequences of light-matter interaction in presence of angular momentum.

In general, light-matter interaction is associated with exchanges of energy, linear momentum, and angular momentum between light and matter. In particular, angular momentum exchanges between light and matter is red by definition related to the existence of optical torque. General picture of light-matter angular momentum exchange process is outlined in Fig. 1.6. Recalling principles of mechanics, the total angular momentum of an isolated system is, by definition, conserved, since there is no external torque applied to the system. In other words, the torque exerted by light on matter is exactly balanced by the torque exerted by matter on light. Hence, the torque $\mathbf{\Gamma}$ exerted by light on the matter is evaluated by considering the balance of the angular momentum of light before and after interaction with matter. Namely,

$$\mathbf{\Gamma} = -\frac{d\mathbf{J}^{\text{light}}}{dt} \,. \tag{1.11}$$

where $\mathbf{J}^{\text{light}}$ is total angular momentum of light field. Next step is to distinguish various processes that may lead to optical radiation torque. In fact these processes can be classified into two categories, *dissipative* or *non dissipative*.

Dissipative processes. For simplicity, let us consider circularly polarized paraxial beam propagating along z axis that carries $\sigma\hbar$ spin and $\ell\hbar$, orbital angular momentum per photon, and is normally incident on homogeneous isotropic absorbing

object[4]. Let us consider the balance of angular momentum per photon

$$\text{Input field} \begin{cases} P_{\text{in}}\,, \\ s_z^{\text{in}} = \sigma\hbar\,, \\ l_z^{\text{in}} = \ell\hbar\,, \end{cases} \qquad \text{Output field} \begin{cases} P_{\text{out}} \leq P_{\text{in}}\,, \\ s_z^{\text{out}} = \sigma\hbar\,, \\ l_z^{\text{out}} = \ell\hbar\,. \end{cases}$$

For incident beam of power P_{in} noting that number of incident photon per unit time is $P_{\text{in}}/\hbar\omega$, torque exerted by light beam equals

$$\Gamma_z^{\text{abs}} = \frac{P_{\text{in}}}{\hbar\omega}(\sigma+\ell)\hbar - \frac{P_{\text{out}}}{\hbar\omega}(\sigma+\ell)\hbar \tag{1.12}$$

introducing parameter $a = \frac{P_{\text{in}}-P_{\text{out}}}{P_{\text{in}}}$ as fraction of absorbed photons

$$\Gamma_z^{\text{abs}} = \frac{aP_{\text{in}}}{\omega}(\sigma+\ell)\,. \tag{1.13}$$

The torque expression indicate additive behavior for the transfer of the spin and orbital angular momentum. Figure 1.7 illustrates the torque dependence on $\sigma+\ell$ for the values of $\ell = \{\pm1, \pm2, \pm3\}$ and for different absorbtion rates corresponding to $a = \{0, 1/2, 1\}$.

There are several reports on experimental observations of optical torques that solely result from light absorption. For instance in Ref. [8] Friese et al. report on spin angular momentum transfer to trapped micron scale absorbing particles that rotate under elliptically polarized Gaussian beam. In Ref. [9] He et al. report on orbital angular momentum transfer to trapped micron scale absorbing particles under linearly polarized Laguerre-Gaussian beam. In Ref. [10] Friese et al. report on the angular momentum transfer including both spin and orbital contributions to trapped micron scale particles under circularly polarized Laguerre-Gaussian beams. Importantly, the latter works demonstrate that spin and orbital angular momentum of light contribute in an independent and additive manner. In addition, such observations illustrate the mechanical equivalence of spin and orbital angular momentum in dissipative process, which has also been addressed in Ref. [11].

Non dissipative processes. Let us consider the case of spin angular momentum

[4]It is assumed that object has transverse size much larger than the beam waist.

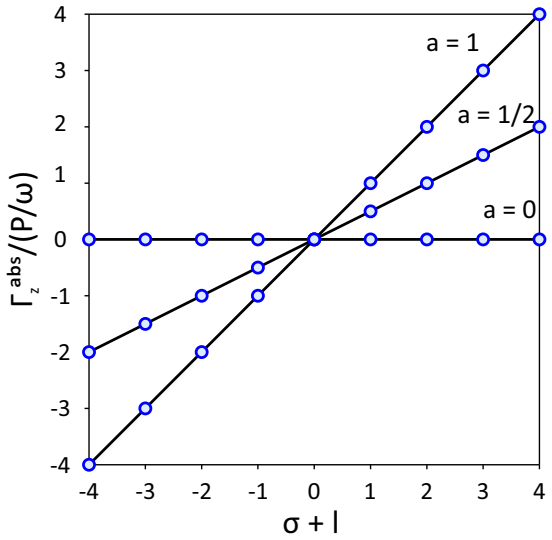

FIGURE 1.7: Optical radiation torque dependence on $\sigma + \ell$ exerted on homogeneous isotropic absorbing object by incident circularly polarized beam with on-axis phase singularity. Different absorbtion rates $a = \{0, 1/2, 1\}$ are considered.

transfer to birefringent media causing polarization changes in light field. Without loss of generality we consider circularly polarized plane wave normally incident on homogeneous and transparent uniaxial slab characterized with a uniform birefringent phase retardation Δ[5]. The latter may be linked to the polarization ellipse angle χ (see Eq.(29) section 1.4 [2]). The output field emerged from the slab can be expressed in the circular basis in the following form[6], up to unimportant phase factor

$$\mathbf{E}_{\text{out}} = E_0 \left[\cos(\Delta/2)\, \mathbf{e}_\sigma + i \sin(\Delta/2)\, \mathbf{e}_{-\sigma}\right] . \tag{1.14}$$

Considering angular momentum balance per photon: note that angular momentum scales to square of the amplitude of the light field,

$$\text{Input field} \begin{cases} P_{\text{in}} = P\,, \\ s_z^{\text{in}} = \sigma\hbar\,, \\ l_z^{\text{in}} = 0\,, \end{cases} \qquad \text{Output field} \begin{cases} P_{\text{out}} = P\,, \\ s_z^{\text{out}} = \cos^2(\Delta/2)\ \sigma\hbar - \sin^2(\Delta/2)\ \sigma\hbar\,, \\ l_z^{\text{out}} = 0\,. \end{cases}$$

[5]We assume object that is larger than the beam waist ensuring that object interacts with full transverse section of beam.

[6]For more detailed analysis see section 1.2 for the more general case of inhomogeneous uniaxial slab.

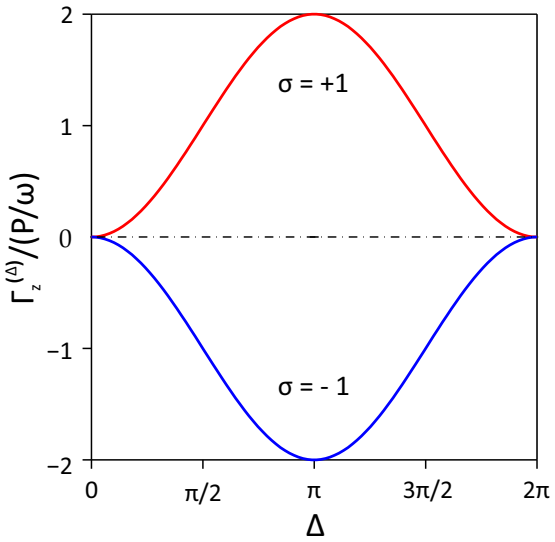

FIGURE 1.8: Optical radiation torque dependence on birefringent phase retardation $0 \leq \Delta \leq 2\pi$ exerted on homogeneous uniaxial media by normally incident circularly polarized field, for both left- and right-handed circular polarization states.

Balance of angular momentum gives

$$\Gamma_z^{(\Delta)} = \frac{P}{\hbar\omega}\,\sigma\hbar - \frac{P}{\hbar\omega}\left[\cos^2(\Delta/2)\,\sigma\hbar - \sin^2(\Delta/2)\,\sigma\hbar\right], \tag{1.15}$$

that is

$$\Gamma_z^{(\Delta)} = \frac{\sigma P}{\omega}[1-\cos(\Delta)]. \tag{1.16}$$

In Fig. 1.8 we illustrate the torque behavior over birefringent phase delay range $0 \leq \Delta \leq 2\pi$, for both left- and right-handed input circular polarization states $\sigma = \pm 1$. Interestingly, such dependence is true for whatever ℓ topological charge value of incident field, since uniform slab does not perturb transverse spatial distribution of phase.

There are several experimental reports on angular momentum transfer to matter that involves birefringent media. A pioneering work dates to 1936, from Beth, who measured spin angular momentum transfer to a torsional pendulum made of centimetre-sized half-wave plate ($\Delta = \pi$) via the detection of angular deflection induced by circularly polarized light [12]. Latter, in Ref. [13] Santamato et al. demonstrated spin angular momentum transfer to a nematic liquid crystal film that acts as light-induced birefringent plate through a nonlinear orientational process. In

turn, this leads to collective molecular precession of liquid crystal molecules around the beam axis (above a threshold power). This was generalized in 1990 to elliptically polarized light that leads to the appearance of precession-rotation regimes for the liquid crystal orientational dynamics [14]. Interestingly, the microscopic version of the original Beth's experiment was reported in 1998 by transferring spin angular momentum to birefringent calcite micro particles [15], via direct observation of rotation of the particles.

The orbital angular momentum can also be transferred to transparent media implying possibility of angular manipulation of transparent and isotropic objects. This was first demonstrated by realignment of rod-like glass objects using Gaussian beams with elliptical intensity profiles, as reported in Ref. [16]. On the other hand, in Ref. [17], Piccrillo et al. report on the spin and orbital angular momentum transfer to nematic liquid crystals also using Gaussian beam with elliptical intensity distributions. The rotation of hollow spherical silica particles by orbital angular momentum transfer using high order Bessel beams is reported in Ref. [18]. Also, the spin and orbital angular momentum transfer induced rotation of birefringent calcite particles was reported in Ref. [4] via optical trapping on- or off-axis of a polarized Laguerre-Gaussian beam. In the latter work, the mechanical equivalence between spin and orbital angular momentum transfer is also discussed.

1.2 Spin-orbit interaction of light

1.2.1 Principle: the case of space-variant birefringent slabs

Considering light propagation in free space, both spin angular momentum and orbital angular momentum are independently conserved, in the framework of paraxial approximation. This is no longer true in general when light propagates in material system. Indeed, spin angular momentum and orbital angular momentum can interact in presence of either optical anisotropy or optical inhomogeneity (or both), hence light field rotational degree of freedom couples to its spatial degrees of freedom.

Let us consider locally anisotropic transparent uniaxial slab with thickness L whose orientation of the optical axis is defined by the angle ψ with respect to the

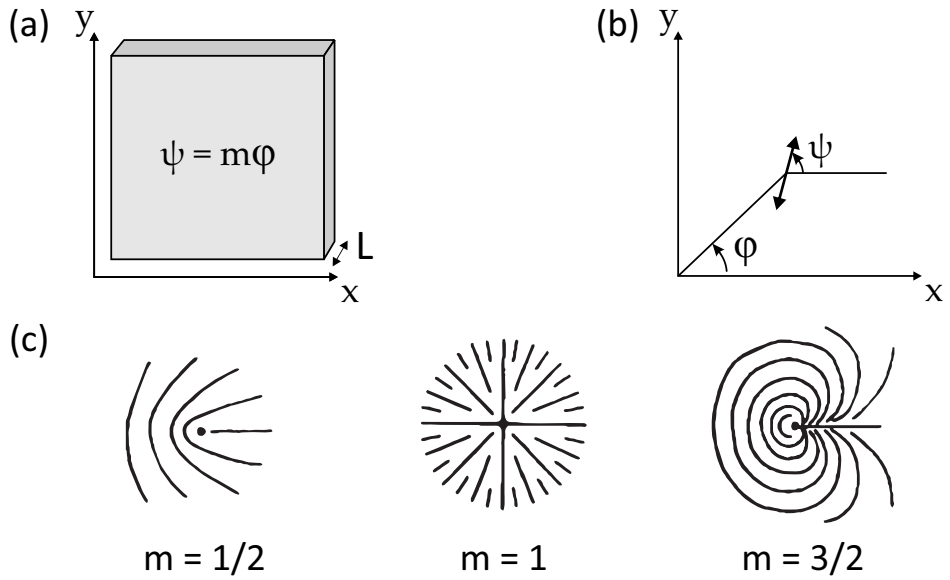

FIGURE 1.9: (a) Azimuthally varying birefringent slab with thickness L, (b) illustration of ψ and φ angles, and (c) examples of the optical axis azimuthal distribution of the form $\psi(\varphi) = m\varphi + \varphi_0$, for $m = \{1/2, 1, 3/2\}$.

x axis as

$$\psi(\varphi) = m\varphi + \varphi_0 \tag{1.17}$$

where φ is the azimuthal angle in the (x, y) plane, and m is the topological charge associated with the singularity of the material optical axis located at $r = 0$, and φ_0 is a constant. The m is half-integer which implies continuous azimuthal variation since $\psi \leftrightarrow \psi + \pi$. Let us consider a circularly polarized monochromatic plane wave with angular frequency ω and wavevector k impinging at normal incidence. The complex representation of such field is

$$\mathbf{E}_{\text{in}} = E_0\, e^{-i(\omega t - kz)}\, \mathbf{e}_\sigma\,. \tag{1.18}$$

Assuming the input facet of the slab located at the plane $z = 0$, and neglecting diffraction, the output light field at $z = L$ is obtained in the laboratory frame using the Jones calculus,

$$\mathbf{E}_{\text{out}} = E_0\, e^{-i\omega t}\, \hat{\mathbf{R}}_z(-\psi) \begin{pmatrix} e^{ikn_\parallel L} & 0 \\ 0 & e^{ikn_\perp L} \end{pmatrix} \hat{\mathbf{R}}_z(\psi)\, \mathbf{e}_\sigma\,, \tag{1.19}$$

where $n_\parallel$ and $n_\perp$ are the refractive indices along and perpendicular to the optical axis, respectively. $\hat{\mathbf{R}}_z(\psi)$ is two dimensional rotation matrix that operates as rotation around z axis by an angle ψ with respect to the x axis in the laboratory frame.

$$\hat{\mathbf{R}}_z(\psi) = \begin{pmatrix} \cos\psi & \sin\psi \\ -\sin\psi & \cos\psi \end{pmatrix}. \tag{1.20}$$

Introducing the total birefringent phase delay of the slab, $\Delta = k(n_\parallel - n_\perp)L$ and expressing in the circular polarization basis for the output we find following

$$\mathbf{E}_{\text{out}} = E_0 e^{-i\omega t} e^{ikn_\perp L} e^{i\Delta/2} \left[\cos(\Delta/2)\,\mathbf{e}_\sigma + i\sin(\Delta/2)\,e^{i2\sigma m\varphi}\,\mathbf{e}_{-\sigma}\right]. \tag{1.21}$$

Hence, the transmitted field is the sum of two orthogonal circularly polarized components that depend essentially on the phase delay Δ. Importantly, the component with circular polarization state orthogonal to that of the incident one, (i.e. the term proportional to $\mathbf{e}_{-\sigma}$), carries an optical phase singularity with topological charge $\ell = 2\sigma m$. That is to say an optical vortex has been generated via spin-orbit interaction of light.

To characterize optical vortex generation process we introduce the quantity

$$\eta = \frac{|\mathbf{E}_{\text{out}} \cdot \mathbf{e}_\sigma|^2}{|\mathbf{E}_{\text{out}}|^2} = \sin^2(\Delta/2), \tag{1.22}$$

which refers to the relative weight of the circularly polarized output field component carrying the optical vortex. By construction $0 \le \eta \le 1$ and one may refer to this quantity as the purity of optical vortex generation process. Importantly, pure vortex state generation requires slab birefringence phase retardation $\Delta = \pi\ [2\pi]$ condition. In that case, optical vortex generation can be described in the circular polarization basis $(\mathbf{e}_+, \mathbf{e}_-)$, the output field up to the phase factor $e^{ikn_\perp L}e^{i\Delta/2}$ equals

$$\mathbf{E}_{\text{out}} = \mathbf{J}_{(m)}\mathbf{E}_{\text{in}} \tag{1.23}$$

where by the Jones matrix is given as

$$\mathbf{J}_{(m)} = \begin{pmatrix} 0 & e^{-2im\varphi} \\ e^{+2im\varphi} & 0 \end{pmatrix}. \tag{1.24}$$

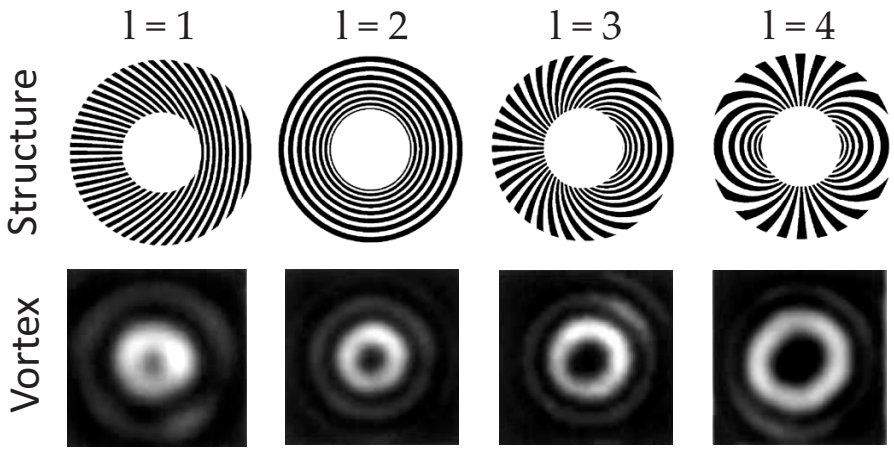

FIGURE 1.10: Illustration of geometry of the subwavelength gratings and corresponding generated optical vortex intensity transverse distributions for topological charges $\ell = \{1, 2, 3, 4\}$. Adapted from Ref. [19].

In addition, we note that if the initial beam carries also orbital angular momentum, the output field (1.21) will include additional factor $\exp(i\ell\varphi)$, which implies that in the process orbital angular momentum per photon changes by an amount of $2\sigma m\hbar$, considering half wave-plate condition of birefringence phase delay.

Next, we briefly overview development of fabrication of such space-variant birefringent optical elements since the pioneering demonstration by Biener and coauthors in 2002, in mid-infrared domain (wavelength 10.6μm) [19]. In that work subwavelength gratings were used to achieve azimuthal structuring of the plane, thereby generating optical vortices (see Fig. 1.10).

1.2.2 State of the art

As spin controlled generators of helical beams that carry well defined orbital angular momentum, space-variant birefringent elements have become of major interest since early demonstration by Biener et al. [19]. After that work, various strategies have been developed to fabricate such optical elements and improve their characteristics. In 2006, Marrucci and coauthors [21] reported on liquid crystal slabs operating in the visible domain in the particular case $m = 1$ (see Fig. 1.11). This was made possible by appropriate alignment technique of the liquid crystal molecules [20], hence the optical axis, in the bulk of a liquid crystal slab. Since then, many surface and bulk liquid crystal alignment techniques have been

developed [22, 23, 24, 25, 26] that nowadays give access to arbitrary topological charge m. Practically, such optical elements are now commercially available and often referred as "q-plates".

Quite naturally, the progresses of fabrication lead to the space miniaturization of such elements from macroscopic to microscopic scale. In particular, first microscopic spin-orbit optical vortex generators proposed by Brasselet and coauthors [27] were based on natural, technology-free approach. Authors used liquid crystal droplets that behave as a mono and polychromatic vortex generator endowed with self-alignment and omnidirectional features (see Fig. 1.12). This development has triggered the use of liquid crystal defect based systems as natural [28] or self-engineered [29] spin-orbit couplers. Noticeably, the extreme sensitivity of liquid crystals to the external fields also led to the realization of microscopic azimuthally patterned birefringent structures based on electrical [30, 31], magnetic [32], optical [33, 34, 35, 36, 37], electro-optical [38, 39], and thermal [40] approaches.

Above we have focused on liquid crystal based approaches of the space-variant birefringent spin-orbit scattering elements yet solid options have also been widely developed during the last decade. In Ref. [41] Beresna et al. report on fabrication of space-variant birefringent elements based on direct femtosecond laser writing technique. Indeed, self-assembled nanostructures are formed in the bulk of silica glass with in-plane slow (fast) axis oriented perpendicular (parallel) to the nanograting wavevector, which induces form birefringence to the structure [42]. Quite recently surface approaches also have been proposed using electron (ion) beam lithography techniques [43, 44], however limited with modest vortex generation efficiency values.

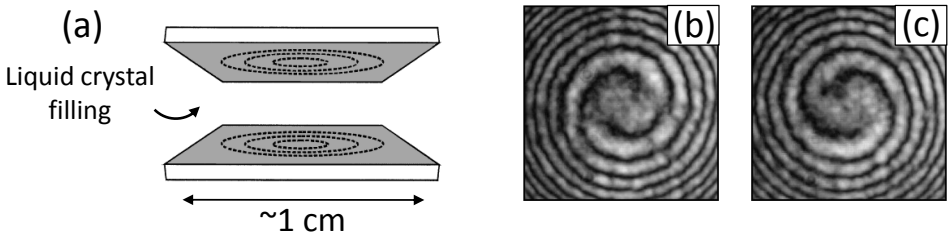

FIGURE 1.11: (a) Illustration of the liquid crystal cell, the concentric lines correspond to the optical axis distribution of structure for m = 1. (b,c) Identification of the generated optical vortex beam using interferometry, for left- and right-handed input circular polarization states. (a) Adapted from Ref. [20], (b,c) adapted from Ref. [21]

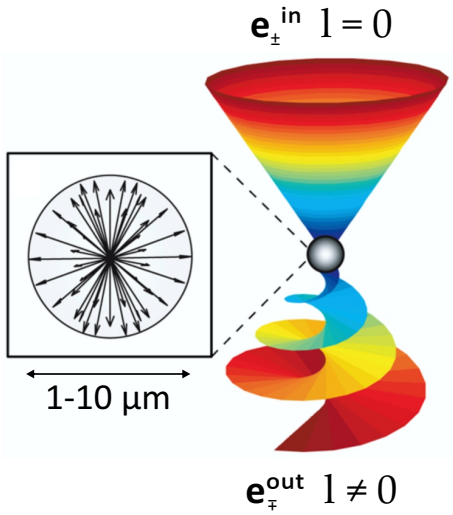

FIGURE 1.12: (a) Illustration of optical vortex generation of from radial nematic crystal droplet optically trapped in circularly polarized tweezers. Inset depicts the tree dimensional radial distribution of the optical axis inside the liquid crystal droplet. Adapted from Ref. [27]

1.3 Optical radiation torque driven by spin-orbit interaction

Apart from polarization controlled optical vortex generation, spin-orbit interaction of light may also have consequences on matter itself. Let us refer to the spin-orbit interaction in the case of space-variant birefringent element presented in previous section and discuss the interaction considering angular momentum transfer to matter.

We consider circularly polarized plane wave normally incident on space-variant birefringent slab with the topological charge m and birefringent phase retardation Δ. Recalling Eq. (1.21), for the angular momentum balance we have

$$\text{Input field} \begin{cases} P_{\text{in}} = P\,, \\ s_z^{\text{in}} = \sigma\hbar\,, \\ l_z^{\text{in}} = 0, \end{cases} \qquad \text{Output field} \begin{cases} P_{\text{out}} = P\,, \\ s_z^{\text{out}} = \left[\cos^2(\Delta/2)\,\sigma - \sin^2(\Delta/2)\,\sigma\right]\hbar\,, \\ l_z^{\text{out}} = 2\sigma m \sin^2(\Delta/2)\hbar\,. \end{cases}$$

This leads to an optical torque

$$\Gamma_z^{\mathrm{soi}(\sigma)} = 2\frac{P}{\omega}\sigma(1-m)\sin^2(\Delta/2)\ . \tag{1.25}$$

We note that Eq. (1.25) is independent of the orbital momentum that incident light may carry. It is interesting to analyze the behavior of such torque depending on material topology; illustrated in Fig. 1.13 for the pure vortex generation case ($\Delta = \pi$). Indeed, depending on the material topological charge m, the torque can have reversed sign to that of incident spin angular momentum. This occurs when $m > 1$. For of $m = 1$ the torque vanishes, which is a consequence of the rotational invariance of the slab optical axis azimuthal distribution along z, and for $m < 1$ the exerted torque has similar direction as incident spin angular momentum.

More generally, optical radiation torque expression in the case of an elliptically polarized incident field is obtained from previous considerations for circular polarization recalling that elliptically polarized light, characterized by ellipticity angle χ, can be decomposed in circular polarization basis following

$$\mathbf{e} = \frac{1}{\sqrt{2}}(\cos\chi + \sin\chi)\mathbf{e}_+ + \frac{1}{\sqrt{2}}(\cos\chi - \sin\chi)\mathbf{e}_-\ . \tag{1.26}$$

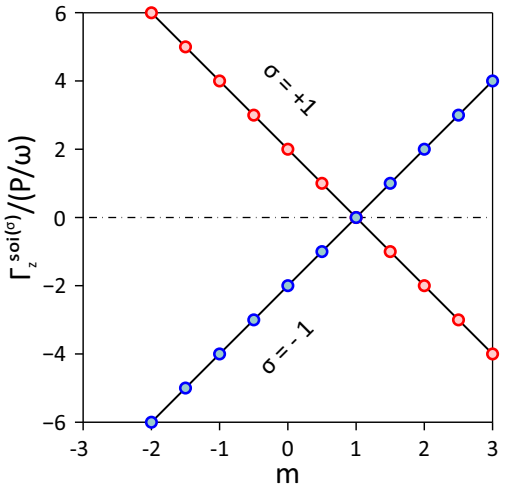

FIGURE 1.13: Optical radiation torque exerted by incident circularly polarized Gaussian beam on azimuthally varying birefringent plate characterized by $\Delta = \pi$ and $-3 \le m \le 3$.

Then, from Eq. (1.25) and (1.26) we obtain

$$\Gamma_z^{\mathrm{soi}} = \frac{1}{2}\Big[(1+\sin 2\chi)\Gamma_z^{\mathrm{soi}(+)} + (1-\sin 2\chi)\Gamma_z^{\mathrm{soi}(-)}\Big], \tag{1.27}$$

hence,

$$\Gamma_z^{\mathrm{soi}} = 2\frac{P}{\omega}\sin(2\chi)(1-m)\sin^2(\Delta/2)\ . \tag{1.28}$$

As a result, the spin-orbit torque behavior versus material topology remains unaltered (up to the factor $\sin 2\chi$) with respect to the case of circularly polarized incident field.

1.4 Motivation and outlook of the thesis

In contrast to the consequences of the optical spin-orbit interaction on the light itself, which is now well developed in the context of the optical vortex generation, its mechanical consequences on matter was experimentally unexplored at the beginning of this thesis. **In fact this was the main motivation of our work: to address experimentally spin-orbit optomechanics**. For this purpose we restricted ourselves to the particular case of azimuthally varying birefringent structures presented in the section 1.2. In turn, Eq. (1.28) is the key equation of the manuscript.

In chapter 2, we discuss spin-orbit optomechanics using nematic liquid crystal defects. Indeed, as mentioned in section 1.2, liquid crystal topological defects locally behave as self-engineered, spin-orbit couplers. Importantly, liquid crystals are also well known to be sensitive to external fields, including light. By construction liquid crystal defects are therefore good candidates to observe mechanical consequences of optical spin-orbit interaction on matter. We report on light induced distortions of the director field that describes the spatial distribution of the local averaged molecular orientation, in presence of spin-orbit interaction of light. In particular, we have studied the role of the birefringent phase retardation and of topological charge m of the liquid crystal defect ($m = \pm 1$).

In chapter 3, we report an attempt to extend the results regarding the topological charge of material defect. This is done by using solid space-variant birefringent macroscopic slabs. Such macroscopic spin-orbit optical elements are commercially available and can be prepared to have arbitrary value of m. In particular, this has allowed us to explore the case $m > 1$ that leads to optical torque reversal with respect to the sign of the incident spin angular momentum carried by light. However, those observations of the optical radiation torque reversal have been restricted to indirect identification via the so called rotational Doppler effect.

In chapter 4, we report on experimental attempts and discuss our developments towards direct observation of optical radiation torque reversal. The main idea is to implement miniaturized versions of space-variant birefringent plates. The later consisting of submicron-thick space variant birefringent nanostructured films, metallic or dielectric that have been fabricated using nanofabrication tools. We

present optical and material characterization of these structures and also the first steps towards the realization of the planned direct spin-orbit optomechanical experiment at the micron scale, which remains an open challenge at the present day.

CHAPTER 2

Optomechanics of liquid crystal defects

In the first chapter we have presented light spin and orbital angular momenta, their interaction, and pointed out some consequences of spin-orbit interaction on both light and matter. In this chapter we report on experimental mechanical manifestation of spin-orbit interaction driven optical radiation torque using nematic liquid crystal defects. We define our requirements for spin-orbit interaction torque observation in section 2.1, where we discuss our choice of spin-orbit coupling media and conditions of torque observation. In particular, we present the umbilical texture found in nematic liquid crystal films that offer spontaneously formed space-variant birefringent structures. In section 2.2 we present principles of our study and propose to benchmark our experimental analysis benefiting from electrically tunable birefringence properties of liquid crystals. Then, we report on distortion of molecular orientation of liquid crystal umbilical defects in presence of spin-orbit interaction of light, namely the direct observation of spin-orbit optomechanics. More precisely, we investigate the spin-orbit optomechanics of liquid crystal defects with topological charge $m = \pm 1$, depending on incident beam polarization state and on electrically tunable optical vortex generation purity. Finally, in the section 2.3 we report on an attempt to extend our investigations to other values of topological charges, $m \neq \pm 1$, by using other kind of liquid crystal defects known as disclinations.

2.1 Towards optical torque observation

2.1.1 Why liquid crystal defects?

To observe spin-orbit interaction driven optical radiation torque manifestation we must choose system that (i) couples light angular momenta and (ii) is sensitive to optical torques. As we have discussed in the section 1.2, space-variant birefringent structures are typical example of spin-orbit couplers, hence, the challenge is to find azimuthally varying birefringent media that is optomechanically responsive. It turns out that liquid crystal defects have all properties to do the "job".

First, as reviewed in section 1.2, we recall that liquid crystal defects are widely implemented as spin-orbit couplers. Starting with the study reported in Ref. [27] our team has been involved in the developments of liquid crystal-defects-based optical vortex generators using different techniques. For instance, in Refs. [30, 31] the liquid crystal defects are generated using external electric field, which provides a self-engineering system that is realizable in practice without additional fabrication and serves as efficient spin-orbit coupler. Later, in Ref. [29] a natural strategy to create spin-orbit couplers has been reported based on liquid crystal defects that occur in nematic films with planar anchoring ("director" is parallel to the film plane). Second, these birefringent structures are transparent over optical wavelengths and are sensitive to external fields, including light. In turn, different phenomena driven by optical radiation torque can be observed in liquid crystals. An example is optically induced molecular reorientation, which occurs in nematic cells and is referred as optical Fréedericksz transition [45]. In addition, liquid crystal defects may be generated by optical torque itself as reported in Refs. [46, 34]. Quite naturally, considering promising characteristics of liquid crystals for spin-orbit interaction torque manifestation and expertise of our team, we choose the liquid crystal defects as spin-orbit couplers for optomechanical observations.

In general, liquid crystals are characterized by the absence of long range positional order, which is typical to liquids, and by the presence of long range orientational order, which is typical to solids. In particular, in nematic liquid crystals, which generally consists of elongated molecules, molecules tend to be locally parallel to each other though without positional order. We describe material

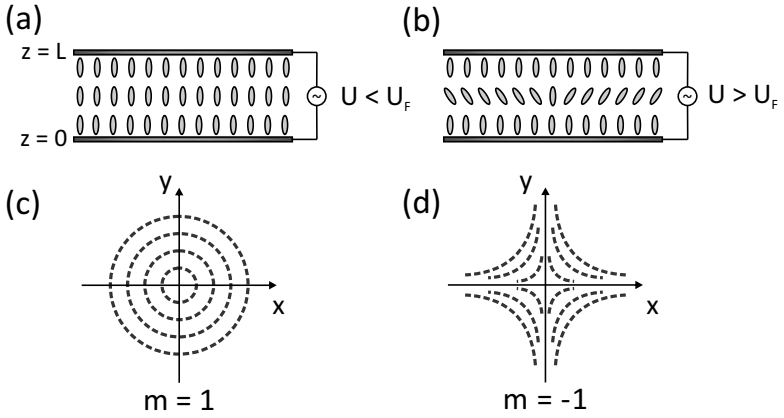

FIGURE 2.1: (a,b) Illustration of side view of nematic liquid crystal ($\epsilon_a < 0$) film of thickness L with homeotropic anchoring below (a) and above (b) the Fréedericksz threshold voltage. (c,d) Illustration of optical axis transverse profile in the plane of the film corresponding umbilical defects with topological charges $m = \pm 1$, respectively.

orientational structure with the unit vector $\mathbf{n}$ referred as director that represents mean local orientation of molecules, with the equivalence $\mathbf{n} \leftrightarrow -\mathbf{n}$ [47]. In addition, liquid crystals are known to exhibit different kinds of topological defects depending on the considered mesophase, bulk and surface environment. In practice, topological defects can be singular or non-singular. In the former case, the liquid crystal order parameter [48] (which quantifies how aligned is liquid crystal) drops to zero over very small spatial scale (typically few nanometers, see [48]): the director is undefined (i.e. singular) at such places. Away from singular defect the order parameter grows until it reaches its value that corresponds to the uniform nematic phase and director gradients emerge around the defect that is characterized by its topology, which indicates the director field organisation in the vicinity of the defect. On the other hand, non-singular defects preserve the orientational order parameter and the director field is defined everywhere, even at the location of the defect. This is made possible by relaxing the elastic gradients associated with a given defect topology owing to an escape of the director field in to the third dimension [48]. A basic example of non-singular defects is the one we propose to use, which are called umbilical defects and that we describe in what follows.

2.1.2 Umbilical defects: orientational structure

Umbilical defects (in short, umbilics) are non-singular topological defects that spontaneously appear in nematic liquid crystals with negative dielectric anisotropy at low frequencies (typically 1-10kHz) in homeotropic films (director at rest is orthogonal to the film plane $\mathbf{n} = |\mathbf{z}|$ see Fig. 2.1(a)) under applied electric field along normal to the film. Since dielectric anisotropy is negative the liquid crystal orientational configuration at rest is stable below a threshold voltage U_F that is of the order of a few volts in practice. Above U_F, the director field is reoriented in the plane of the film owing to an electric torque (Fig. 2.1(b)). Since the reorientation plane is azimuthally degenerate, such reorientation leads to the spontaneous formation of defects of opposite topological charges $m = \pm 1$ (see Fig. 2.1(c,d)). These structures were reported in [49, 50] and mathematically described in [51]. Following the notations introduced in Ref. [31] we experimentally describe the director field of the umbilical defects using Cartesian coordinate system related with the basis $(\mathbf{x}, \mathbf{y}, \mathbf{z})$ by the following form

$$\mathbf{n} = (\sin\vartheta\cos\psi, \sin\vartheta\sin\psi, \cos\vartheta) \tag{2.1}$$

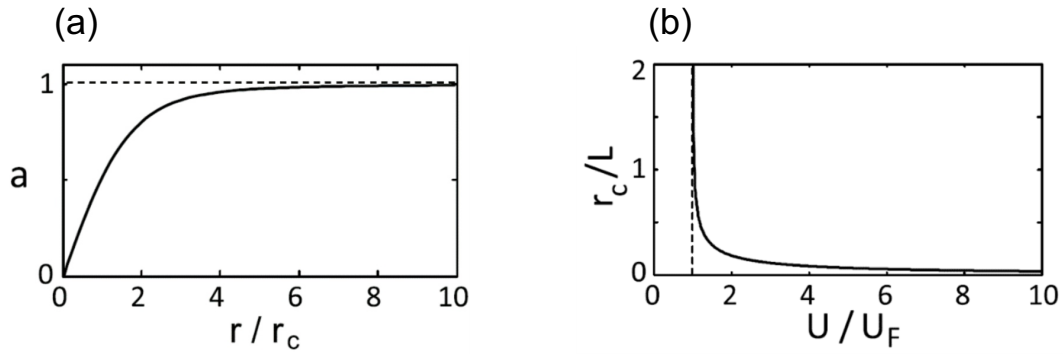

FIGURE 2.2: (a) Calculated reduced amplitude a of the tilt angle θ in the vicinity of defect ($r = 0$). (b) Calculated reduced core radius r_c/L dependence over reduced voltage U/U_F. Adapted from Ref. [31].

where ψ is the director orientation angle with respect to x axis, ϑ is director tilt angle with the z axis. These angles are defined as

$$\psi = m\varphi + \varphi_0\,, \tag{2.2}$$

$$\vartheta(r,z) = \theta_\infty a(r)\sin\left(\pi\frac{z}{L}\right), \tag{2.3}$$

where φ is the azimuthal angle, φ_0 is constant, and $m = \pm 1$ is topological charge of the defect, while r is the radial coordinate ($r = \sqrt{x^2+y^2}$) and L is the thickness of the film, $0 \le a(r) \le 1$ is the reduced tilt amplitude and θ_∞ is the asymptotic value of θ corresponding to large values of r. The latter is defined as [31]

$$\theta_\infty = [2(\tilde{U}^2-1)/(K_1/K_3 - \tilde{U}^2\epsilon_a^\Omega/\epsilon_\parallel^\Omega]^{1/2} \tag{2.4}$$

where $\tilde{U} = U/U_F$ is the reduced voltage and K_1 (K_3) is Frank's elastic constant associated with the splay (respectively bend) deformation [47] and $\epsilon_a^\Omega = \epsilon_\parallel^\Omega - \epsilon_\perp^\Omega$ is the dielectric anisotropy related with the $\epsilon_{\parallel,\perp}^\Omega$ dielectric permittivities along and perpendicular to the director $\mathbf{n}$ at the frequency Ω of the applied voltage. Finally, the reduced tilt amplitude $a(r)$ satisfies a second order differential equation (see Eq.(5) Ref. [31]), whose numerical solution is presented in Fig. 2.2(a) versus the reduced radius r/r_c. The parameter r_c is the defect core radius that is expressed as

$$r_c = \frac{L}{\pi}\left(\frac{K}{K_3}\right)^{\frac{1}{2}}(\tilde{U}^2-1)^{-\frac{1}{2}}, \tag{2.5}$$

where, K is the effective elastic constant that depends on the Frank's elastic constants, defect topological charge m and constant angle φ_0. The dependence of the r_c over reduced voltage U/U_F is shown in Fig. 2.2(b). The total phase retardation related to the birefringence of the defects is expressed by the following form

$$\Delta(r) = \frac{2\pi}{\lambda}\int_0^L [n_e(r,z) - n_\perp]dz, \tag{2.6}$$

where the $n_\perp$ is the refractive index of the ordinary wave and $n_e(r,z)$ is the refractive index of extraordinary wave given by form

$$n_e(r,z) = \frac{n_\parallel n_\perp}{\left[n_\parallel^2 \cos^2\vartheta(r,z) + n_\perp^2 \sin^2\vartheta(r,z)\right]^{\frac{1}{2}}}. \tag{2.7}$$

With the knowledge of both the director field topology $m = \pm 1$ and the spatial distribution of birefringent phase delay $\Delta(r)$ we are thus formally equipped to address spin-orbit interaction of light and its mechanical consequences. Before doing so, hereafter we present practical observations of umbilics and their actual ability to operate as spin-orbit optical elements.

2.1.3 Umbilical defects: experimental identification

In practice, umbilical defects are easily identified by observations between crossed linear polarizers as shown in Fig. 2.3(a), where we observe assembly of both $m = \pm 1$ defects represented as dark cross pattern. The centers of crosses correspond to the defect locations while dark lines correspond to locations where the projection of the director in the film plane is oriented parallel to the direction of one of the two crossed polarizers. However, as such, this does not allow to distinguish topological charges of the defects. There are several methods available for the identification of topological charge of defects. A simple one consists to rotate the pair of polarizers. The relative sense of rotation of the dark cross with respect to that of the polarizers identifies topological charge of defect. A clockwise rotation of the dark cross pattern, while polarizers are rotated clockwise, corresponds to defect of topological charge $m = +1$, Fig. 2.3(b). On the other hand, counterclockwise rotation of the dark cross pattern, while polarizers are rotated clockwise, corresponds to defect of topological charge $m = -1$, Fig. 2.3(c).

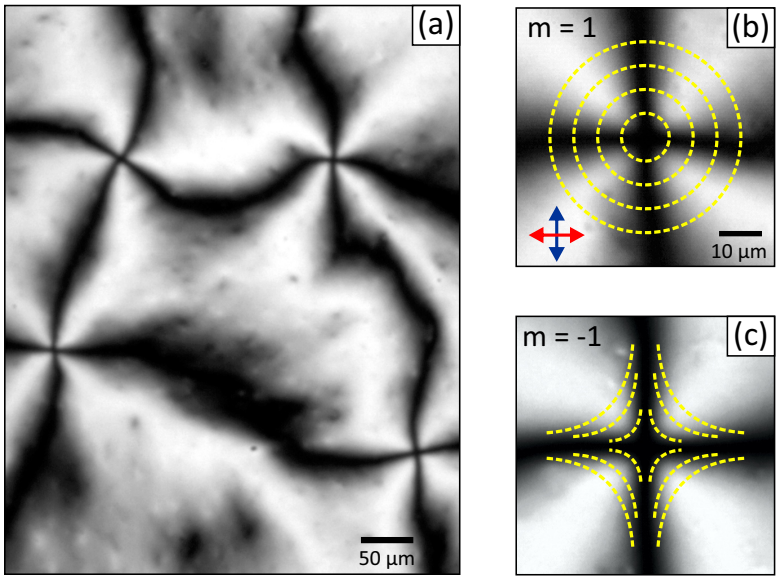

FIGURE 2.3: (a) Image of umbilical defects assembly of topological charge $m = \pm 1$ observed between crossed linear polarizers using incoherent illumination. (b,c) Images of isolated umbilical defects of topological charge $m = \pm 1$ between crossed linear polarizers; dashed lines correspond to director orientation in the plane of the film, arrows to polarizers orientation. $L = 10$ μm homeotropic cell filled with MLC-2079 liquid crystal.

2.1.4 Umbilics as spin-orbit vortex generators

In practice we have used $L = 10\ \mu$m thick liquid crystal commercial cell with with ITO electrode and homeotropic alignment. The cell was filled with MLC-2079 liquid crystal, which is characterized by the negative dielectric anisotropy $\epsilon_a^\Omega = \epsilon_\parallel^\Omega - \epsilon_\perp^\Omega = -6.1$ with the $\epsilon_\parallel^\Omega = 4.1$ and $\epsilon_\perp^\Omega = 10.2$ at frequency $\Omega = 1$ kHz and Fréedericksz threshold voltage $U_F = 1.83\ V_{\rm rms}$ defined by $U_F = \pi[K_3/(\epsilon_0|\epsilon_a^\Omega)]^{1/2}$, where the ϵ_0 is the vacuum dielectric permittivity. In practice, we found $U_F \simeq 1.90\ V_{\rm rms}$ at working frequency $\Omega = 2$ kHz. We obtain isolated umbilical defects by first, applying high voltage $U \simeq 10U_F$ that causes a dense generation of umbilical defects of topological charge $m = \pm 1$, and then the sample is left for relaxation for a few hours while maintaining applied voltage $U \geq U_F$. During that time, annihilation dynamics of opposite sign topological defects occur [52]. Finally, we are left with a few umbilical defects at fixed locations in the film area.

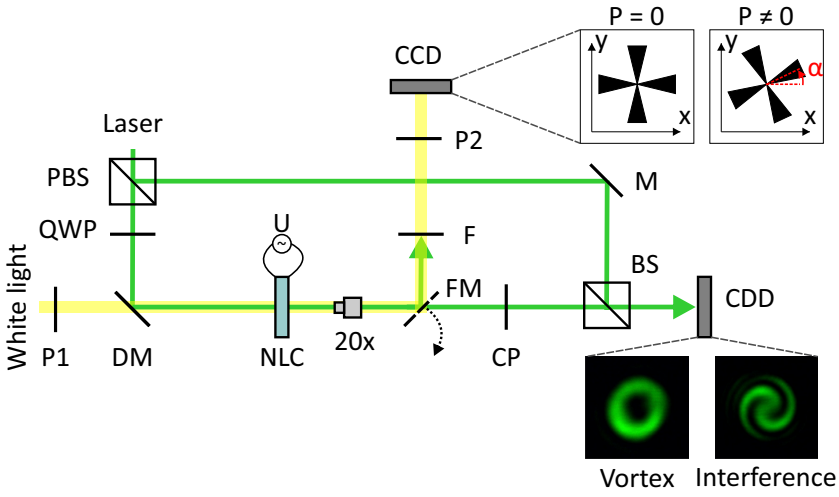

FIGURE 2.4: Scheme of experimental setup, P1 and P2 linear polarizers, DM dichroic mirror with reflection band 330-550nm and transmission band 584-700 nm, F longpass filter which blocks light with wavelength shorter than the cut-off wavelength 590 nm, M mirror, FM mirror on flip mount, PBS polarizing beam splitter and QWP quarter-wave plate, CP is circular polarizer. A moderately focused circularly polarized Gaussian beam is normally incident on a homeotropic NLC cell and a collimated white light is used to image the defects. Upper inset corresponds to defect cross pattern twist angle configuration for the case $m = -1$ and incident light circular polarization state $\sigma = 1$, lower insets observation of output vortex and its interference with Gaussian reference beam.

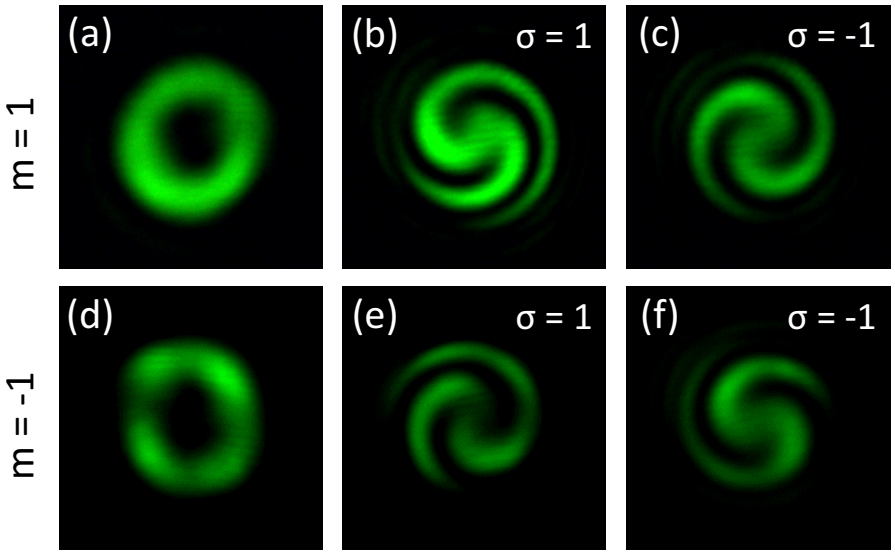

FIGURE 2.5: (a,d) Optical vortex intensity transverse profiles corresponding to the umbilical defects of topological charge $m = \pm 1$, (b,c) and (e,f) interference patterns revealing on-axis phase singularities of vortex beams obtained by collinear and coherent superposition of output vortices with co-circularly polarized Gaussian field, corresponding to the umbilical defects of topological charge $m = \pm 1$ and incident light field circular polarization $\sigma = \pm 1$.

Following the experimental setup shown in Fig. 2.4, we are able to observe umbilics between crossed linear polarizers while illuminating them on-demand using a Gaussian laser beam at 532 nm. In particular, observation of optical vortex generation is made following the framework presented in section 1.2. Namely, we set the polarization of the incident Gaussian beam on the liquid crystal film to circular ($\mathbf{e}_\sigma$) and we place a circular polarizer at the output of the liquid crystal film, which selects orthogonal ($\mathbf{e}_{-\sigma}$) circularly polarized component of the output beam. Then, we tuned the applied voltage to achieve maximum efficiency for the optical vortex generation. Indeed, following equations presented in previous section, birefringence phase retardation associated with defects depends on the applied voltage and the distance the defect location, namely $\Delta = \Delta(r, U)$. In particular, if the laser beam waist w_0 on the sample is larger enough than the core radius r_c the beam "sees" almost a uniform birefringence, $\Delta = \Delta(U)$. In that case, appropriate tuning of the applied voltage allows reaching the half-wave plate condition $\Delta = \pi\ [2\pi]$ that gives optimal vortex generation, $\eta = 1$ (see Eq (2.8)). In practice, we set $w_0 \simeq 30\ \mu$m and

we obtain maximal optical vortex generation efficiency at $U = 2.18\ V_{\mathrm{rms}}$, which gives $r_c \simeq 3.3\ \mu$m (see Eq. (2.5)), with purity parameter equal to $\eta(U)_{\max} \simeq 87\ \%$ for all defects. Obtained purity corresponds to a practical trade-off between the need for $w_0 >> r_c$ and the finite distance ($\approx 150\ \mu$m) between two defects that prevents for using arbitrarily large values of w_0. However, this is not a serious drawback since it merely reduces the expected spin-orbit torque by the multiplying factor 0.87 (Eq (2.8)).

The transverse intensity distributions of optical vortices are presented in Fig. 2.5(a,d), which correspond to defect topological charges $m = \pm 1$. One can note that the intensity distributions are not axisymmetric as the Rapini's [51] description would suggest. This can be explained partly by non ideal centering of the incident beam on the defect, but this argument is not enough to explain observed four-fold rotational symmetry of the contracircular intensity pattern for $m = -1$ (Fig. 2.5(d)). The latter is explained by recalling that umbilics with $m = -1$ involve both splay and twist elastic distortion of the director (see Fig. 2.3(c)). This is not accounted by Rapini's approach, however, recent theoretical studies provide with detailed discussion of such axisymmetry breaking [53].

Experimentally, the singular phase pattern underlying doughnut-shape intensity patterns shown in Fig. 2.5(a,d) are revealed by interferometry. This is done by introducing a reference arm with the same circular polarization state and superposed with the output beam (collinear superposition). As introduced in section 1.1, we observe spiralling patterns that correspond to an optical phase singularity of topological charge $2\sigma m$, with $2m$-arm spirals twisting clockwise or counterclockwise consistent with the sign of product σm, as illustrated in Fig. 2.5 (b,c) and (e,f) respectively for both $m = \pm 1$ defects and $\sigma = \pm 1$ incident beam circular polarization states.

2.2 Principle of the optomechanical study

2.2.1 General statements

In principle, once spin-orbit interaction is at play, we expect to observe an optical torque driven reorientation of the liquid crystal molecules, which should

correspondingly lead to the deformation of the dark cross pattern observed between crossed linear polarizers that are associated with orientational transverse profile of liquid crystal defects. For this purpose, we introduce the dark cross (in short, the cross) tilt angle α that corresponds to azimuthal angle with respect to the x direction as illustrated in Fig. 2.4. Recalling the expression of the spin-orbit interaction driven torque (see section 1.3)

$$\Gamma_z^{\mathrm{soi}(\sigma)} = 2\frac{P}{\omega}\sigma(1-m)\sin^2\left(\frac{\Delta}{2}\right) = 2\frac{P}{\omega}\sigma(1-m)\eta\,. \tag{2.8}$$

where η is the optical vortex generation purity parameter, we will analyze the dynamics of cross pattern for both defects $m = \pm 1$ over the range of the incident light beam power P considering both $\sigma = \pm 1$ incident circular polarization states.

As a first step we propose to benchmark our study by analyzing dynamics of cross for the case of $\Delta \simeq 2\pi$. Indeed, this corresponds to zero torque configuration independently of the material topology or incident beam polarization state. Therefore this will provide us with a "reference" experiment for which the result is qualitatively expected from angular momentum balance. Then, the case $\Delta \simeq \pi$, which corresponds to maximal torque configuration, can be addressed in a comparative manner with respect to the reference experiment. We further refer to the above mentioned configurations as minimal η_{min} and maximal η_{max} optical vortex generation cases.

2.2.2 Spin-orbit optomechanics reference experiment

The experimental protocol consists selecting an umbilical defect of topological charge $m = \pm 1$ and illuminating it with left/right-handed ($\sigma = \pm 1$) circularly polarized Gaussian beam. Then, as the incident beam power P is increased, the dark cross images of illuminated defect are collected in situ. Importantly, we note that the initial voltage ensuring $\eta = \eta_{\mathrm{min}}$ at $P = 0$ no longer provides $\eta = \eta_{\mathrm{min}}$ when $P \neq 0$. This is due to the fact that the electric field of the laser beam, which lies in the plane of film (recalling moderate focusing is used), tends to reorient the director in the plane of the film since the dielectric anisotropy is positive at optical frequencies. Consequently, Δ is changed optically, which de-tunes the defect from

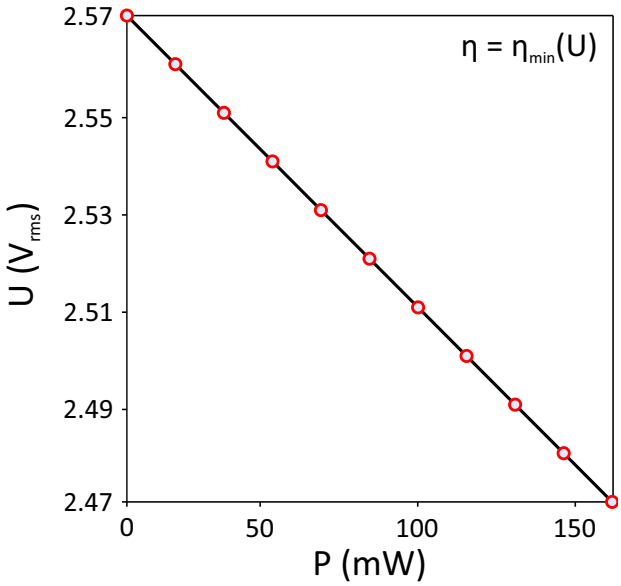

FIGURE 2.6: External electrical voltage dependence versus incident light beam power while maintaining the minimal optical vortex generation, i.e. $\eta = \eta_{\min}$. These results do not depend on the umbilical defect topological charge $m = \pm 1$.

expected operation mode characterized by $\eta = \eta_{\min}$. Still, this can be compensated by reducing the applied voltage as the beam power increases. This is done for every P and the results, which are independent on topological charge m, are shown in Fig. 2.6.

Finally, the obtained sequences of images corresponding to the defects $m = \pm 1$ as a function of the incident beam power over the range $0 - 150$ mW for both left- and right-handed circular polarization states are shown in Fig. 2.7. Qualitatively, from mere visual inspection of the latter figure we conclude to no visible effect whatever the incident power, the incident helicity and considered defect. These demonstrations are consistent with the expected zero net optical torque when $\eta = 0$ (see Eq. (2.8)), hence no orientational transverse profile modifications.

Still, we have addressed the phenomenon quantitatively, by reproducing the experiments with several defects (four pairs of defects with $m = \pm 1$) and measuring the angle α via image processing. This angle is evaluated using the correlation coefficient $C(\alpha)$ between cross pattern images at zero power and power P, an example is presented in the Fig. 2.8(b,c). We present the results in Fig. 2.8(a) where markers are experimental values, solid lines are linear fitting lines and bars

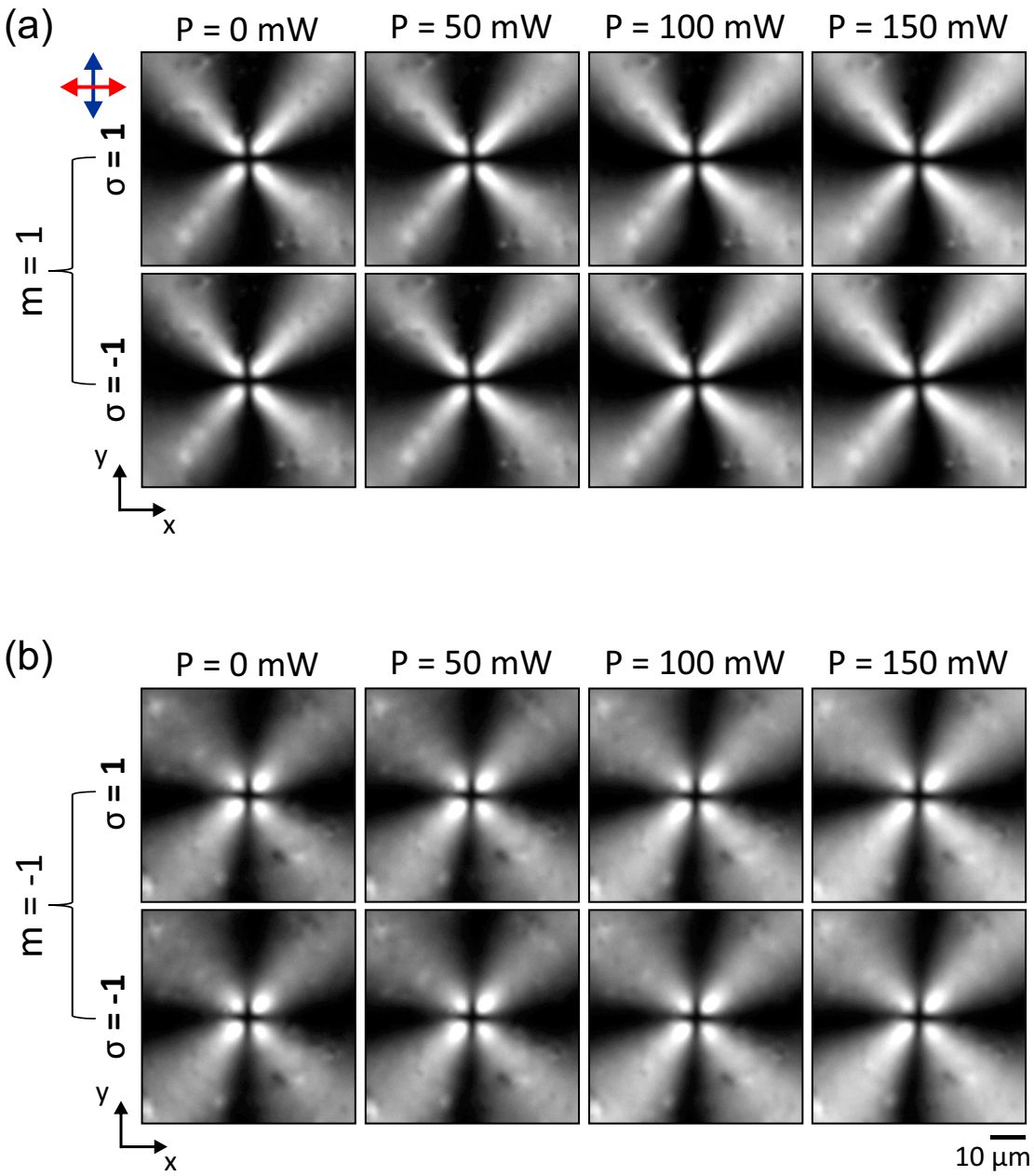

FIGURE 2.7: Dark cross patterns under crossed linear polarizers versus beam power for normally incident circularly polarized Gaussian beam, in the case of the minimal optical vortex generation purity $\eta_{\min} \simeq 0$, for both $m = \pm 1$ topological charges and $\sigma = \pm 1$ incident polarization states. Arrows correspond to the crossed linear polarizer orientations.

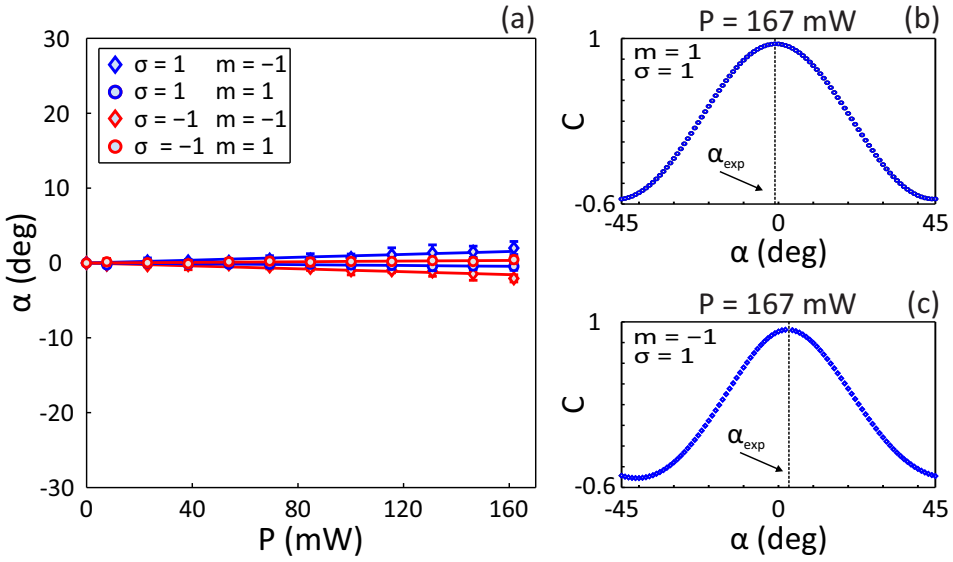

FIGURE 2.8: (a) Cross pattern tilt angle α versus beam power with the illustration of the standard deviation (four pairs of defects $m = \pm 1$) and linear fitting that correspond to minimal vortex generation $\eta_{\min} \simeq 0$, for both $m = \pm 1$ topological charges and two orthogonal incident circular polarization states $\sigma = \pm 1$. (b,c) Example of α evaluation with correlation coefficient $C(\alpha)$ between cross images at $P = 0$ and $P = 167$ mW corresponding to left-handed ($\sigma = 1$) input polarization for both $m = \pm 1$, respectively.

correspond to standard deviation of data. The magnitude of α does not exceed few degrees, $|\alpha| \leq 3°$ over the explored range of optical power, independently of the defect topological charge and incident light polarization state. Such residual tilt of the cross may be linked to inhomogeneous distribution of birefringent phase retardation $\Delta(r)$ associated with defects or the fact that 2π configuration is not preserved rigourously. It could also be attributed to the fact that expected zero net torque is however associated with non zero optical angular momentum deposition along the beam propagation direction as the light passes through the sample. Indeed, qualitatively, when $\Delta = 2\pi$, the first half of the sample (along z direction) experiences a torque $\Gamma_{z,1}^{\mathrm{soi}(\sigma)} = 2\frac{P}{\omega}\sigma(1-m)$ while the second part experiences a torque with same magnitude and opposite sign $\Gamma_{z,1}^{\mathrm{soi}(\sigma)} = -\Gamma_{z,2}^{\mathrm{soi}(\sigma)}$. Consequently, we could expect a twist of director field along the z axis that affects the propagation of light, hence crossed-polarizers imaging. Practically, thus we consider observed effects as experimental "baseline" when probing spin-orbit optomechanical response.

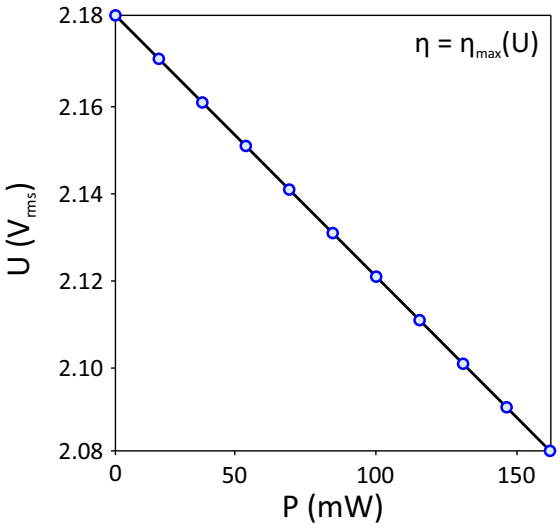

FIGURE 2.9: External electrical voltage dependence versus incident light beam power while maintaining the maximal optical vortex generation, i.e. $\eta = \eta_{\max}$. These results do not depend on the umbilical defect topological charge $m = \pm 1$.

2.2.3 Optimal spin-orbit optomechanics

Once the reference experiment is done, we can consider maximal optical vortex generation purity case, by setting applied voltage to obtain ideally birefringence phase retardation condition $\Delta(U) = \pi$ that gives $\eta = \eta_{\max}$. Similarly to the case $\eta = \eta_{\min}$, we need to decrease the applied voltage as the beam power increases, to maintain the condition $\eta = \eta_{\max}$, which is summarized in Fig. 2.9. Likewise to the previous analysis we have selected isolated umbilical defects topological charge $m = \pm 1$ and performed power study for both, $\sigma = \pm 1$, incident circularly polarized cases, collecting the cross images of defects observed between crossed linear polarizers. Figure 2.10 summarizes the observations. Strikingly, the latter figure indicates slight changes for $m = 1$ while drastic modifications are observed for $m = -1$, where cross is significantly tilted as beam power increases.

Qualitatively, from Eq. (2.8), the modest effect for $m = 1$ can be explained from the fact that net optical torque is zero in that case. On the other hand one expects non-zero net optical torque proportional to power for the $m = -1$. To assess the effect quantitatively we have measured the tilt angle α by reproducing experiments with several pairs of defects $m = \pm 1$. Figure 2.11 summarizes the results, where markers correspond to the experimental data, solid lines to linear fitting lines, and

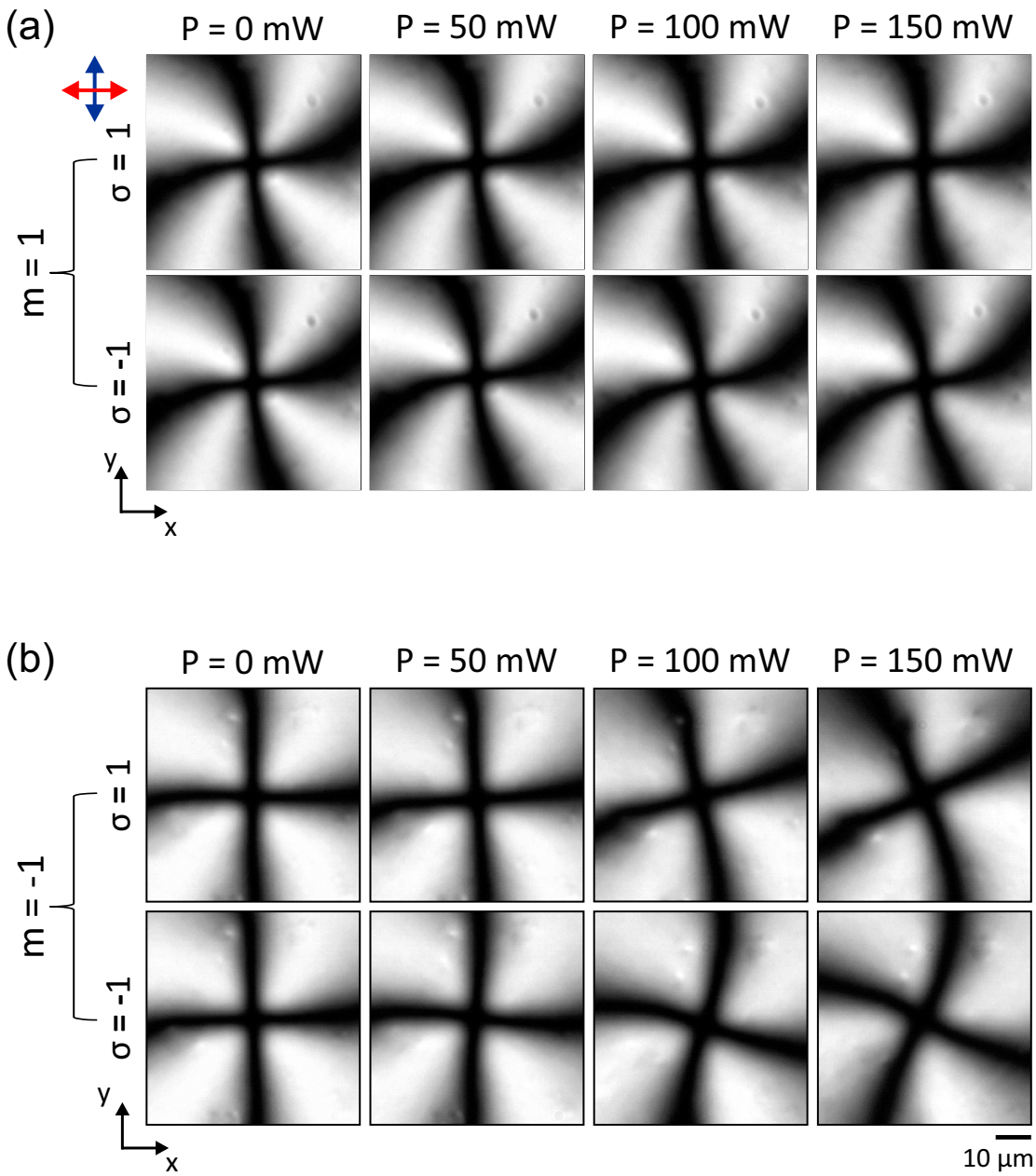

FIGURE 2.10: Dark cross patterns under crossed linear polarizers versus beam power for normally incident circularly polarized Gaussian beam, in the case of the maximal optical vortex generation purity $\eta_{\max} \simeq 87$ %, for both $m = \pm 1$ topological charges and $\sigma = \pm 1$ polarization states. Arrows correspond to the crossed linear polarizer orientations.

	$m = 1$		$m = -1$	
	$\sigma = 1$	$\sigma = -1$	$\sigma = 1$	$\sigma = -1$
$\frac{d\alpha}{dP}\|_{\eta_{\max}}$	-0.02	0.02	0.15	-0.16
$\frac{d\alpha}{dP}\|_{\eta_{\min}}$	-0.002	0.002	0.009	-0.009

TABLE 2.1: Table of the slope values of cross tilt angle α dependence incident field power increment corresponding executions presented in Fig. 2.8 and Fig. 2.11

bars to standard deviation. Indeed, we have measured maximal tilt in $|\alpha| \simeq 5°$ for the defects with topological charge $m = 1$ and $|\alpha| \simeq 25°$ for the defects with topological charge $m = -1$ independently of the incident circular polarization state. Since we are dealing with a power study, these results can be summarized by the slope values $d\alpha/dP$, see Tab. 2.1. In contrast to the case $\eta = \eta_{\min}$, both magnitude and sign of α exhibit meaningful relationship with the defect topological charge m, incident polarization state σ and power P, when $\eta = \eta_{\max}$.

In fact, in all cases we observe a linear dependence of α with respect to beam power P, which matches with the expected behavior assuming that spin-orbit torque $\Gamma_z^{\mathrm{soi}(\sigma)}$ given by Eq. (2.8) is at work. Moreover, the sign of α is helicity-dependent, as expected from Eq. (2.8). However, surprisingly, the expected dependence $\Gamma_z^{\mathrm{soi}(\sigma)} \propto (1 - m)$ is not clearly observed experimentally.

Indeed, a non-zero "non-noisy" helicity behavior as the power increases is found for $m = 1$, which can not be simply explained by the simple balance of optical angular momentum in axially symmetric birefringent structures as shown in Ref. [54] where it is demonstrated theoretically that the moment of radiation force density (orbital angular momentum contribution) balances locally the torque arising from spin angular momentum transfer. This would suggest no mechanical effect induced by light in the liquid crystal film. Still it should be noted that the two latter contributions of identical magnitude and opposite sign for $m = \pm 1$ do not act on the same degrees of freedom of the liquid crystal. In fact, spin angular momentum deposition acts on the orientational degree of freedom of the material, hence leading in our case to azimuthally symmetric angular deviation of director field in the plane of the film. On the other hand, orbital angular momentum deposition acts

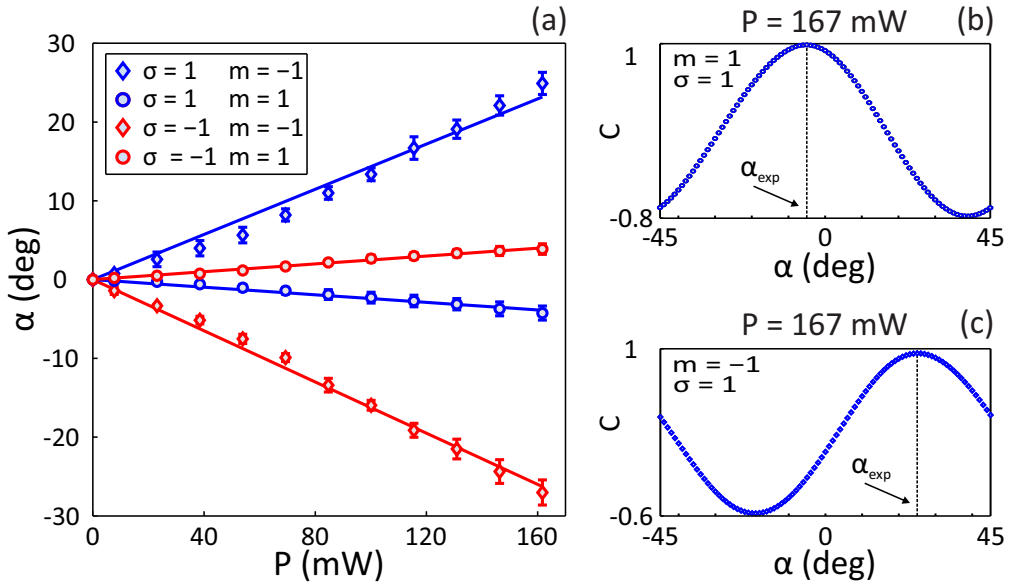

FIGURE 2.11: Cross pattern tilt angle α versus beam power with the illustration of the standard deviation (four pairs of defects $m = \pm 1$) and linear fitting that correspond to the maximal vortex generation $\eta_{\max} \simeq 87$ %, for both $m = \pm 1$ topological charges and both orthogonal incident circular polarization states $\sigma = \pm 1$. (b,c) Example of α evaluation with correlation coefficient $C(\alpha)$ between cross images at $P = 0$ and $P = 167$ mW corresponding to left-handed ($\sigma = 1$) input polarization for both $m = \pm 1$.

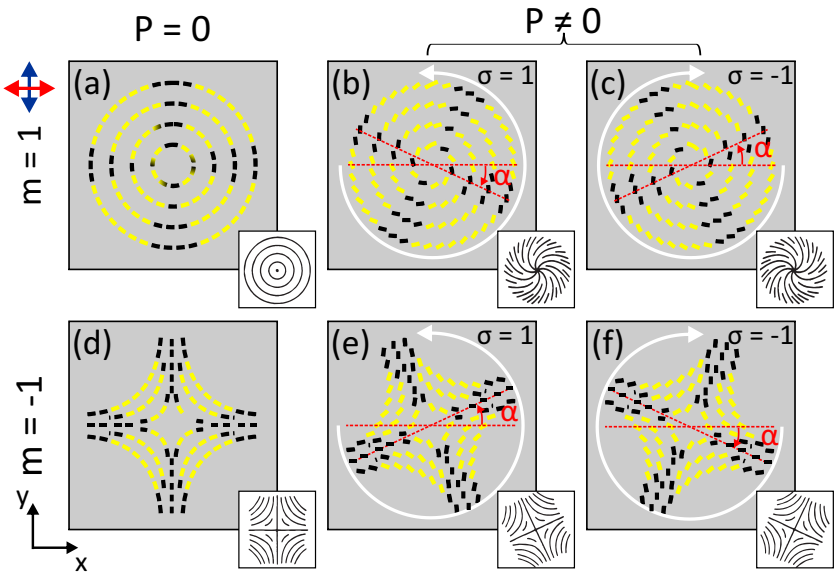

FIGURE 2.12: Illustration of α tilt handedness with association to the incident (spin) angular momentum handedness for both $m = 1$ (a,b,c) and $m = -1$ (d,e,f) and polarization states $\sigma = 1$ (b,e) and $\sigma = -1$ (c,f). Straight arrows correspond to the orientations of crossed polarizers, circular arrows to the incident beam circular polarization handedness, and darkened lines correspond to cross. Insets correspond to molecular orientation streamlines sketch.

on positional degree of freedom, hence leading to liquid crystal azimuthal flow. The consequence is that elastic distortion and flow can take place before the liquid crystal reaches its steady state. This has already been reported experimentally in Refs. [55, 56, 27] with case of radially oriented nematic droplets that can be viewed as the three dimensional analog of umbilic with $m = 1$. All this offers an explanation of helicity-dependent spin-orbit optical torque even though Eq. (2.8) predicts zero torque for that case. In addition, we emphasize that the observed dependence $\alpha \propto -\sigma P$ for $m = 1$ is consistent with above statements noting that spin angular momentum driven torque is expected to generate local in-plane director reorientation of form $\delta\Psi \propto -\sigma P$, as illustrated in Fig. 2.12.

The case of umbilics with $m = -1$ is easer to explain since in this case the dependence $\Gamma_z^{\mathrm{soi}(\sigma)} \propto \sigma(1-m)P$ implies that spin angular momentum and orbital angular momentum contributions are of the same sign. Moreover, the observed dependence $\alpha \propto \sigma P$ is consistent with spin angular momentum driven in plane director reorientation of the form $\Psi \propto \sigma P$, as illustrated in Fig. 2.12. Also the

much larger effect observed for $m = -1$ is consistent with the fact that both spin and orbital contributions works "in the same direction", hence adding up their effects.

Summarizing, the above results bring a first experimental attempt to observe directly optomechanical manifestation of the spin-orbit interaction driven optical torque.

2.3 Topological charge diversity

The above results obtained using liquid crystal defects with topological charge $m = \pm 1$ brought experimental demonstration of optical radiation torque driven by spin-orbit interaction of light. However, the use of umbilics reduces de facto our investigations to a limited number of situations. Importantly we miss the case of $m > 1$ that is expected to lead to an optical radiation torque having opposite sign to that of the (spin) angular momentum of incident polarized Gaussian beam. To test it one needs to repeat the above experiments with liquid crystal defects of another kind. To this aim, Schlieren defects (disclinations) are promising candidates at first sight. Disclinations are singular topological defects that spontaneously form in nematic liquid crystal films having planar (see Fig. 2.13) degenerate surface orientational boundary conditions [57]. They correspond to director distribution in the plane of the film that satisfy local orientational distribution of the form $\psi = m\varphi$ with m half-integer. In practice, only $-1 \leq m \leq +1$ defects are stable and observed, see Fig. 2.14. However, under specific circumstances, topological charges $m > 1$ may be observed. Indeed, by doping usual nematic liquid crystals with non-mesogenic dopants, it has been shown that disclinations with $m > 1$ appear [58]. In the context

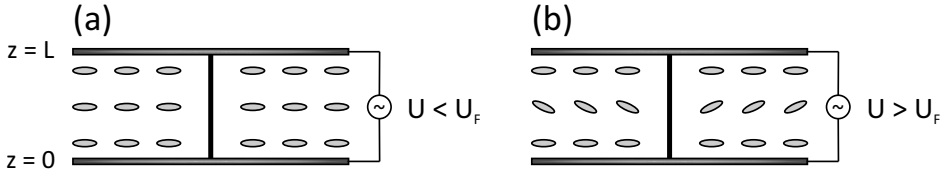

FIGURE 2.13: (a,b) Illustration of side view of nematic liquid crystal ($\epsilon_a > 0$) film of thickness L with planar anchoring below (a) and above (b) the Fréedericksz threshold voltage. The thick dark line corresponds to the center of disclination.

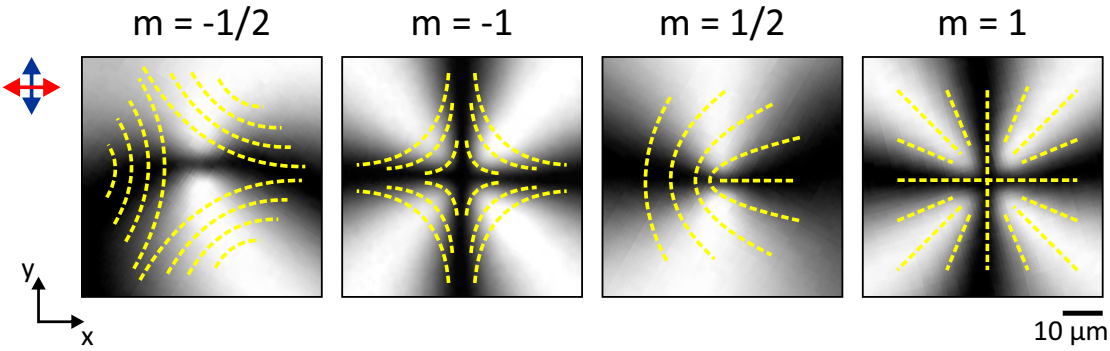

FIGURE 2.14: Dynamics of dark cross pattern corresponding to the Schlieren textures of topological charge $m = \{\pm 1/2, \pm 1\}$ observed between crossed linear polarizers: disclination at rest. Dashed lines correspond to director orientation in the plane of the film, arrows to polarizers orientation

of spin-orbit interaction of light such higher order defects have recently been shown capable of optical vortex generation with fairly good quality [29], thereby offering a chance to address spin-orbit optomechanics with $m > 1$.

Therefore we implemented the use of Schlieren defects following the approach discussed above for umbilics, starting with the simplest case of non-doped nematics, hence restricting ourselves to $-1 \leq m \leq 1$ for preliminary investigations. The samples are prepared by using bare glass substrates to form the liquid crystal film made of the mixture MLC-7023 ($\epsilon_a > 0$) 13 μm cell that has ITO electrodes. Using similar polarized microscopy procedure as for identification of umbilic topological charges (2.1.3) we collected four distinct defects characterized by $m = \{-1, -1/2, 1/2, 1\}$. Then, following the protocol to optimize spin-orbit optical torque magnitude, we apply a voltage in order to realign the director along the normal to the film (recall that $\epsilon_a > 0$ here) until half-wave plate condition is obtained. The images of prepared defects observed between crossed linear polarizers are shown in Fig. 2.14 where there is no laser beam ($P = 0$). Finally, laser is turned on. As shown in Fig. 2.15 no director field distortion is detectable up to $P = 150$ mW, in stark distinction to the case of umbilics. We thus conclude that even if there is non-zero spin orbit torque, its mechanical manifestation is null.

To explain these observations we note an important difference between umbilics and disclinations, even for a given topological charge m. Indeed, surface boundary conditions are perpendicular for umbilics while they are parallel for disclinations. In

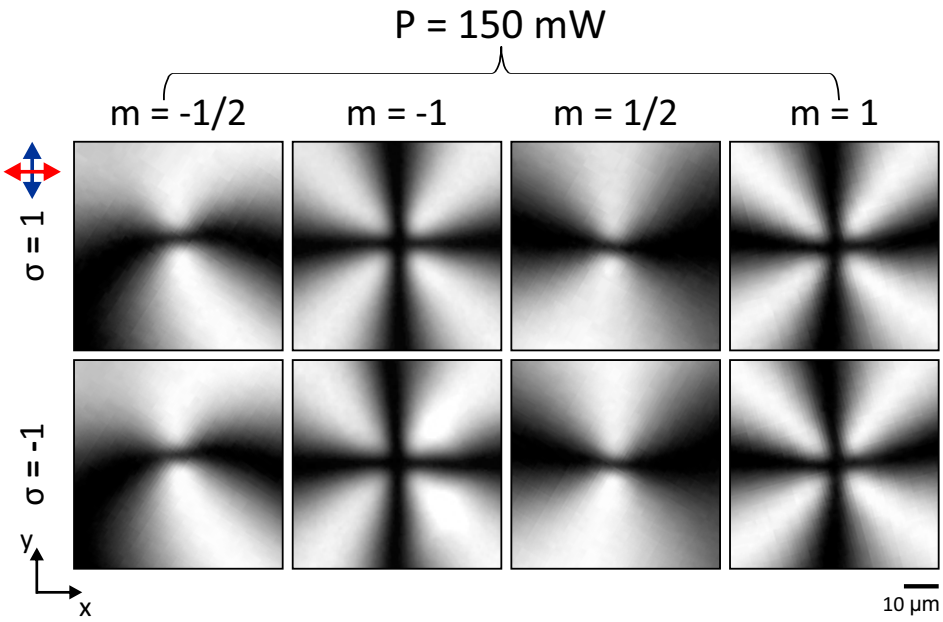

FIGURE 2.15: Dynamics of dark cross pattern corresponding to the Schlieren textures of topological charge $m = \{\pm 1/2, \pm 1\}$ observed between crossed linear polarizers under illumination of 150 mW for both incident helicities $\sigma = \pm 1$.

turn, the liquid crystal orientational structure at the glass interface is azimuthally degenerate at every point for umbilics, which is not the case for disclinations. The consequence is that the umbilics are much more prone to support twisted director field in the bulk than the disclinations. In fact, it is known from earlier studies on optical reorientation of liquid crystals that it is much more demanding to reorient optically a planar film than a homeotropic film. For instance, for linearly polarized beam at normal incidence on a uniform film, director reorientation occurs above a threshold which is several orders of magnitude higher for planar films than for homeotropic films [59]. In the present case, although our samples have space variant azimuthal director orientation, above considerations give a solid argument to understand the observed "rigidity" of disclinations.

As a matter of fact, if we aim at exploring the situation with $m > 1$, another option should be put in place. This is the purpose of the next chapter.

CHAPTER 3

Optical torque reversal: indirect observations

In the preceding chapter we have explored mechanical consequences of spin-orbit interaction of light using nematic liquid crystal defects as inhomogeneous and birefringent media. Namely, we have reported on the manifestation of an optical torque driven by spin-orbit interaction by analyzing light induced distortions of the liquid crystal molecular orientation. Nevertheless, such study was restricted to defects having topological charges $m = \pm 1$. In this chapter we extend spin-orbit optomechanics of defects to topological charge $|m| \neq 1$, by using artificially structured glass slabs fabricated via femtosecond direct laser writing. Such plates are commercially available and can be designed to have arbitrary topological charge. We purposely focus our study to topological charges $m = \{1/2, 1, 3/2\}$, which are associated with homogeneous birefringent phase retardation $\Delta = \pi$. Indeed, this choice allows addressing of optical torque reversal while passing from topological charge $m = 1/2$ to $m = 3/2$, under fixed incident optical spin angular momentum. In section 3.1 we introduce the concept of the "left-handed" optical torque and discuss its analogy with so called "negative" optical forces. Next, we present birefringent phase plates and our experimental approach to determine left-handed torque using circularly polarized beam in section 3.2. Then, in section 3.3 we present experimental demonstration with two-beam (collinear and non-collinear) interferometric approaches and analyze the torque quantitatively as well study its dependence over all involved parameters. In section 3.4 we present simplified experimental approach with a linearly polarized single beam. Finally, we generalize left-handed torque to arbitrary values of birefringent phase retardation and incident polarization state in section 3.5.

3.1 Left-handed optical radiation torque

Before introducing our concept of "left-handed" optical torque, it is relevant to present the following optomechanical context. In fact, left-handed torque echoes the concept of "negative" optical forces that have been introduced recently [60, 61]. Contrary to the conventional Keplerian intuition that objects should be pushed downstream an incident light beam, negative forces attract objects towards the source of illumination. The concept is outlined in Fig. 3.1, where the object is illuminated along the positive z direction and is pulled towards negative z direction. In general, such forces result from net forward scattering of optical linear momentum. As reviewed in Ref. [62], this is achieved by tailoring properties of the electromagnetic field, the object, and/or the environment.

The angular analog of such counterintuitive optical force corresponds to optical torque that has direction reversed to that of incident light (spin) angular momentum, and we refer to such torque as "left-handed" implying its counter-intuitive nature. Accordingly, we refer to the torque produced in common situations as "right-handed" torque. Both configurations are outlined in Fig. 3.2, considering light field carrying s_z spin angular momentum and exerting a torque Γ_z on the illuminated object. Usually, the optical torque has the sign of s_z, whatever s_z, that is $s_z\Gamma_z > 0$. Examples are the cases of absorbing objects or transparent wave-plates, as previously discussed in chapter 1. Such situation is shown in Fig. 3.2(a). In contrast, left-handed torque manifests as the torque direction opposes the direction of the incident (spin) angular momentum, that is $s_z\Gamma_z < 0$, whatever s_z. As a result, the illuminated object tends to rotate with reversed handedness to that of the incident angular momentum.

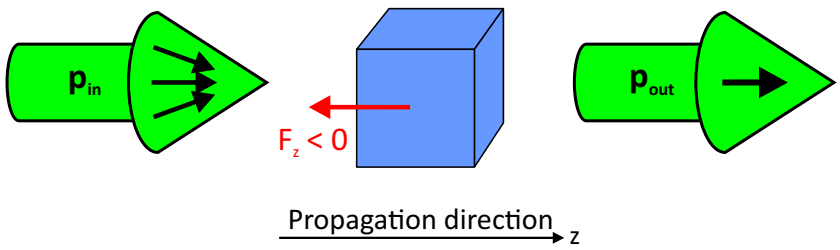

FIGURE 3.1: Concept of optical negative force, which implies pulling of the object towards the illumination source. Negative forces occur when there is a net forward scattering of the linear momentum, which may be written formally as $F_z \propto (\mathbf{p}_{\text{in}} - \mathbf{p}_{\text{out}})\mathbf{z} < 0$.

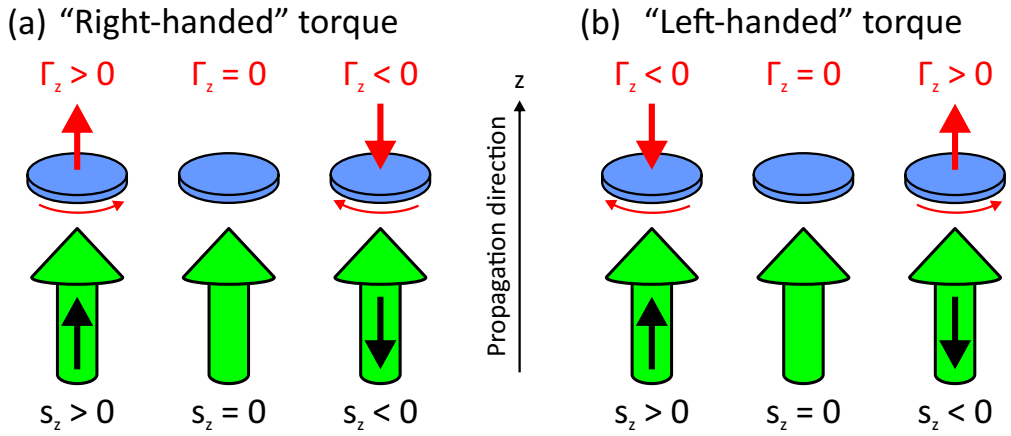

FIGURE 3.2: Schematic illustrations of the conventional (a) and non-conventional (b) manifestations of optical torques Γ_z exerted on matter by interaction with incident Gaussian beam, which carries s_z spin optical angular momentum per photon along its prorogation direction z. (a) Right-handed torque configuration, which corresponds to $s_z\Gamma_z > 0$ for any s_z. (b) Left-handed torque configuration, which corresponds to $s_z\Gamma_z < 0$ for any s_z.

Left-handed situation is shown in Fig. 3.2(b). Intriguingly, a few years ago, it has been predicted that a tightly focused circularly polarized Gaussian beam could exert a torque directed oppositely to that of the incident angular momentum on wavelength-sized oblate particles made of transparent isotropic media [63], whereas the first experimental identification actually corresponds to present chapter.

To reverse torque sign with respect to incident light angular momentum there should be a net forward scattering of angular momentum, mimicking the situation with the negative forces and linear momentum. Within present framework of azimuthally varying optical elements, it is impossible to achieve angular momentum negative balance whatever s_z based only on spin angular momentum light-matter exchanges. Indeed, let us assume $m = 0$ (hence no orbital angular momentum light-matter exchanges). In that case $l_z^{\text{in}} = l_z^{\text{out}}$ and left-handed torque implies $s_z^{\text{in}}\Gamma_z = 1 - s_z^{\text{in}}s_z^{\text{out}} < 0$. However, since $-1 \leq s_z^{\text{in}}s_z^{\text{out}} \leq 1$, the latter inequality cannot be satisfied. In contrast, for $m \neq 0$, the total angular momentum balance may be dominated by orbital contribution, hence optical torque reversal becomes possible.

More precisely, recalling the optical radiation torque expression involved in spin-orbit interaction of light, introduced earlier for the case of space-variant birefringent

slab (see section 1.3),

$$\Gamma_z^{\text{soi}} = 2\frac{P}{\omega}\sin(2\chi)(1-m)\sin^2(\Delta/2)\,, \tag{3.1}$$

and analyzing its behavior over topological charge m, we realize that the sign of the torque flips while passing from $m < 1$ to $m > 1$. We note that the latter case corresponds to torque that has opposite sign with respect to incident (spin) angular momentum of light given by $s_z = \sin(2\chi)\hbar$ angular momentum per photon, hence left-handed torque manifests. Thus, to achieve left-handed optical radiation torque our idea is to exploit spin-orbit interaction of light involving $m > 1$ topological charge defects.

3.2 Experimental approach

3.2.1 Samples: solid state q-plates

Towards experimental demonstration of optomechanical manifestation of left-handed torque, we have used space-variant birefringent glass slabs commonly referred as "q-plates", see chapter 1, which are commercially available, and can be designed to have arbitrary m topological charge value. We have purposely selected a set of plates with azimuthal optical axis distribution $\psi = m\varphi$ that corresponds to three different topological charges $m = \{1/2, 1, 3/2\}$, as shown in Fig. 3.3(a). The plates have been fabricated by Altechna R & D company using femtosecond direct laser writing of self-assembled nanostructures in the bulk of silica glass [64]. In fact, depending on parameters of focused writing laser beam self-organized stripelike structures appear with width of ~ 20 nm forming a grating wit period of 140 – 320 nm depending of the power and irradiation rate of writing laser (Fig. 3.4). Such subwavelength structuring induces form birefringence, the slow axis being oriented perpendicular to the nanograting wavevector (see Fig. 3.4), whereas fast axis is oriented parallel to the nanograting wavevector [41]. In addition, our samples are designed to have uniform birefringent phase retardation $\Delta = \pi$ that corresponds to the half-wave plate configuration for the wavelength 532 nm, that is a purity parameter $\eta = 100\%$.

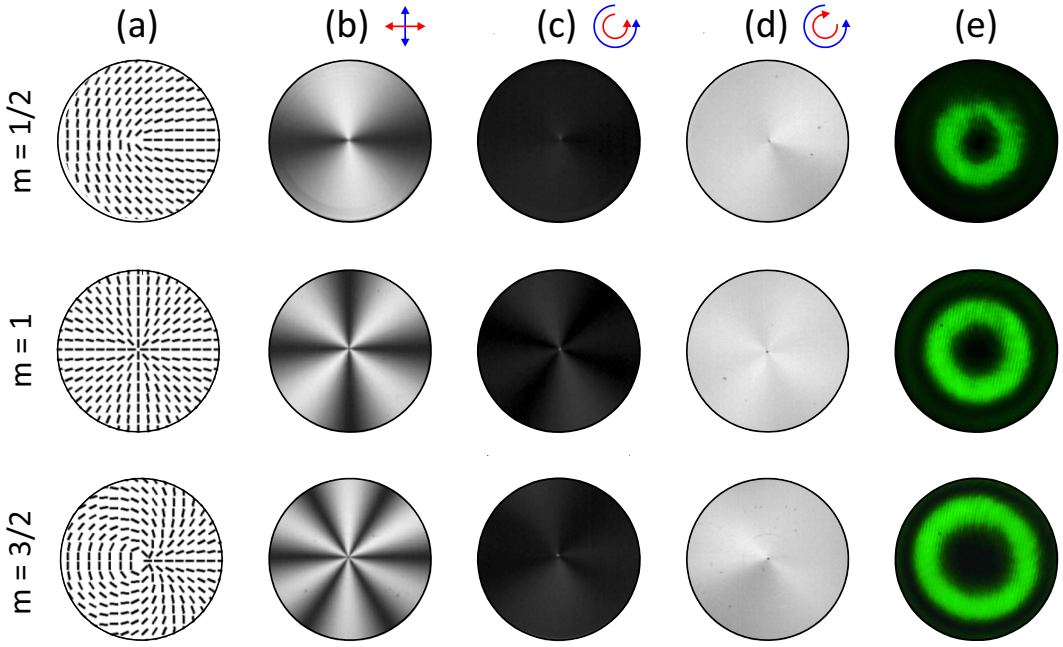

FIGURE 3.3: Design and optical characterization of azimuthally varying form birefringent glass samples that correspond to the topological charges $\{m = 1/2, 1, 3/2\}$. For each topological charge, first column (a) corresponds to slow axis in-plane spatial distribution, where segments imply local orientation. Second, third, and fourth columns correspond to polarimetric analysis performed by spatially incoherent illumination of a wavelength 532 nm, which illustrates images of the retarders placed between, crossed linear (b), parallel circular (c), and crossed circular (d) polarizers showing optical axis profile and birefringent retardation uniformity. Fifth column (e) displays output beam intensity transverse profiles that correspond to optical vortices of topological charges $\ell = \pm 2m$, considering incident circularly polarized Gaussian beam, sign depending on polarization handedness.

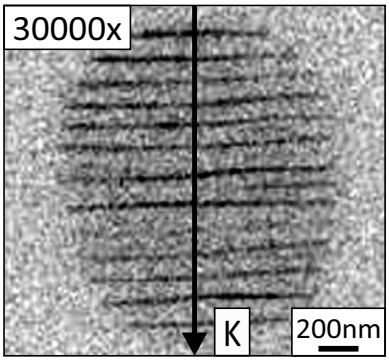

FIGURE 3.4: Scanning electron microscope image of silica glass surface showing light induced nano-grating formed by focused femtosecond laser beam irradiations. Arrow illustrates the direction of the nano-grating wavevector that is parallel to incident beam polarization direction. Adapted from Ref. [42].

First, we have characterized samples implementing polarimetric analysis with incoherent light source at considered wavelength 532 nm. The orientational profile of optical axis is experimentally observed by placing the samples between crossed linear polarizers. Resulting images are shown in Fig. 3.3(b), where dark lines correspond to places where optical axis is parallel to one of the two crossed linear polarizers. On the other hand, birefringent phase retardation uniformity is experimentally assessed by placing the samples between parallel and crossed circular polarizers - Figs. 3.3(c) and 3.3(d).

Then, we have validated the action of such plates on light experimentally, considering on-axis incident circularly polarized field, which is transformed into orthogonally polarized field carrying on axis optical phase singularity $\ell = 2\sigma m$. In practice, we have illuminated the plates with circularly polarized, paraxial Gaussian beam of wavelength 532 nm and waist radius $w \simeq 1$ mm. The output doughnut intensity transverse distribution snapshots are shown in Fig. 3.3(e). Note that the doughnut diameter increases over topological charge, while preserving similar incident beam diameter, as expected from the fact that Laguerre-Gaussian beam amplitude scales to $[r/w(z)]^{|\ell|} \exp(-r^2/w(z))$ (see Eq. (1.9)).

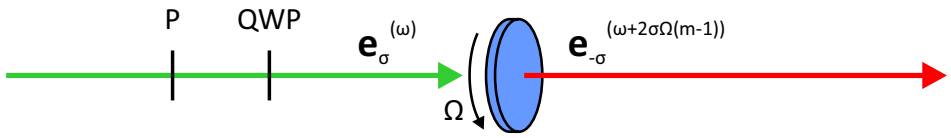

FIGURE 3.5: Scheme of the rotational Doppler frequency shift experiment: A circularly polarized Gaussian field is normally incident into birefringent retarder that rotates with constant angular velocity Ω, which is controlled by external DC motor. Optical elements are abbreviated as follows: P is linear polarizer, QWP is quarter-wave plate.

3.2.2 Detection technique: Rotational Doppler frequency shift

To detect left-handed optical torque, a univocal experimental approach consists of direct observation of light induced rotation of the sample. This would allow retrieving with ease optical torque reversal from the visual observation of the sample rotation depending on incident light polarization handedness. However, a simple estimate of the expected effect shows that the situation is challenging in practice. Indeed, let us consider an optical torque produced via a transfer of $\hbar$ angular momentum per photon to the sample, under 1 W visible light illumination. This gives $\Gamma = P/\omega \sim 10^{-16}$ Nm. On the other hand, assuming the sample is immersed in an inviscid medium and free to rotate, we find a rotation frequency ν that depends on illumination time T as $\nu(T) = \Gamma T/(\pi M R^2)$, where M is mass of the sample and R is radius. Taking into account that considered birefringent structures are embedded in slabs of radius $R = 12.7$ mm and thickness $H = 3$ mm with mass density $\rho = 2.5 \times 10^3$ kg m^{-3}, we obtain $\nu \sim 1$ mHz after three months illumination at $P = 1$ W. Clearly, with considered samples the direct experimental detection of left-handed optical radiation torque is impractical.

Still, we propose to circumvent such technical difficulty by considering indirect observations that consists to probe the mechanical consequence of the spin–orbit scattering process on light itself instead of probing mechanical effects on the sample. This is achieved by implementing a rotational Doppler frequency shift experiment [65, 66]. In practice, the sample is externally rotated (using a computer-controlled rotating stage) at controlled angular velocity Ω around incident beam propagation direction, as illustrated in Fig. 3.5. In such experiment, non-zero optical torque exerted by light on the slab causes a rotational Doppler frequency

shift $\delta\omega$ for the output light. The shift is independent of the incident light field frequency and is proportional the angular velocity of the rotating plate, in contrast to linear Doppler frequency shift [66]. Without loss of generality, we consider circularly polarized collimated Gaussian beam with the waist radius $w \simeq 1$ mm (the structured area corresponds to $R_s = 2$ mm centered on slab) normally incident on the birefringent samples. As introduced in section 1.3, this gives an optical torque $\Gamma_z^{\mathrm{soi}(\sigma)} = 2\frac{P}{\omega}\sigma(1-m)$.

To access to the rotational Doppler frequency shift, we analyze energy conservation considering light-matter as isolated system. Its total energy is thus conserved, which allows writing the following power balance

$$\Gamma_z\Omega + \frac{\delta\omega}{\omega}P = 0\,, \tag{3.2}$$

where $\omega' = \omega + \delta\omega$ is the angular frequency of the transmitted light. Accordingly, we have a direct relationship between the torque and rotational Doppler frequency shift:

$$\Gamma_z = -\frac{P}{\omega}\frac{\delta\omega}{\Omega}\,, \tag{3.3}$$

which allows us to stress that the rotational Doppler shift measurement is indeed reminiscent of the existence of an optical torque in our experiment.

Substituting the optical torque expression into Eq. (3.3) we obtain the rotational Doppler frequency shift

$$\delta\omega = 2\sigma(m-1)\Omega\,. \tag{3.4}$$

To determine $\delta\omega$, hence Γ_z, our experimental approach consists of interferometric analysis, enabling time varying phase monitoring via time varying intensity measurements, which is purpose of the following section.

3.3 Two-beam experimental demonstration and parametric study

3.3.1 On-axis two-beam experimental demonstration

First, we have implemented a two-beam approach as outlined in Fig. 3.6, where we consider a circularly polarized Gaussian beam impinging on a rotating slab with topological charge m. The reference arm of the interferometer consists of circularly polarized Gaussian beam with orthogonal polarization state to that of input beam, which ensures appearance of intensity fringes as a result of interference between superposed beams. We consider on-axis (collinear) superposition of the reference and output beams that leads to formation of $2|m|$-arm spiraling interference patterns, as introduced in section 1.1.2 and shown in present case in lower insets of Fig. 3.7.

For the sake of demonstration, the sample is rotated at angular velocity $\Omega \simeq 0.40$ rad s^{-1} and the spiraling interference patterns are recorded over period of two minutes ($T = 120$ s). Resulting spatiotemporal interference patterns are presented in Fig. 3.7(a,b,c). The patterns revolve or not depending on topological charge. Indeed, patterns rotate for $m = 1/2$ and $m = 3/2$, while the case of $m = 1$ corresponds to a static situation. Note that the sense of rotation differs for $m = 1/2$ and $m = 3/2$.

Another visual representation of spatiotemporal dynamics consist of correlation coefficients $C(t)$ between the static patterns at time $t = 0$ and t, see Fig. 3.8. Sinusoidal behavior is observed for $m = 1/2$ and $m = 3/2$, whereas it shows non-

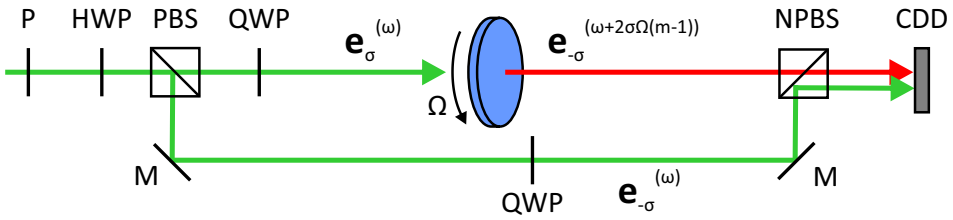

FIGURE 3.6: Scheme of rotational Doppler frequency shift experimental set-up that consists of collinear Mach–Zehnder interferometer, which we use to record interference patterns between output beam with frequency $(\omega+\delta\omega)$ and reference beam with frequency (ω). The reference beam polarization state handedness is the same as that of the output beam. The optical elements are abbreviated as follows: P is linear polarizer, HWP is half-wave plate, QWP is quarter-wave plate, M is mirror, PBS is polarizing beam splitter, NPBS is non-polarizing beam splitter, CCD is imaging device.

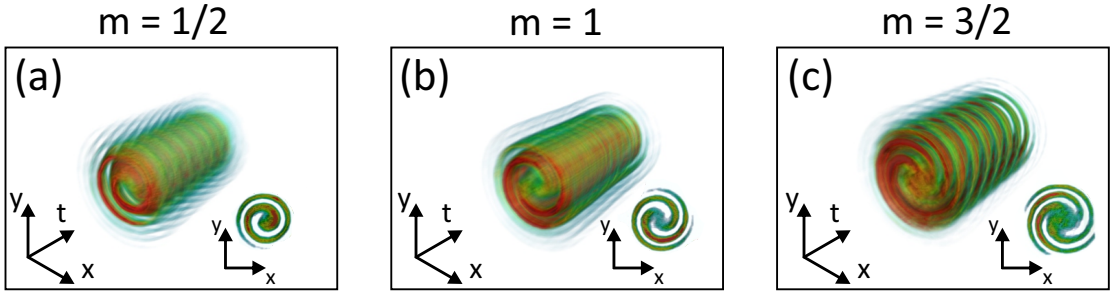

FIGURE 3.7: The interference patterns and their time evolutions resulting from collinear interferometer corresponding birefringent plates $m = 1/2$ (a) $m = 1$ (b) and $m = 3/2$ (c). Upper inset represent spatiotemporal evolutions of the interference patterns corresponding to the time duration of $T = 120$ s, whereas lower insets are static snapshots of patterns at $t = 0$ that are formed in the (x, y) plane.

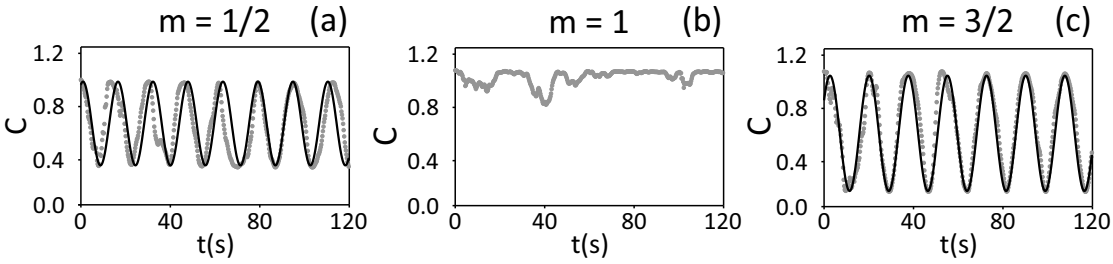

FIGURE 3.8: Time dependence of the correlation coefficient $C(t)$ between intensity patterns formed at $t = 0$ and t, where the solid lines for the $m = 1/2$ and $3/2$ refer to fit by sinusoidal function.

oscillating behavior that corresponds to case of the sample with topological charge $m = 1$. Data fitting these sinusoidal curves using trial function $C(t) = a + b\sin(\Omega_C t + c)$ gives $\Omega_C = 0.36$ rad s^{-1} when $m = 1/2$ and $\Omega_C = 0.40$ rad s^{-1} when $m = 3/2$. In fact Ω_C can be identified as the Doppler frequency shift $\delta\omega$. Indeed, let us consider interference between two co-polarized plane waves with angular frequencies ω and $\omega + \delta\omega$ and identical intensity. One gets for the intensity pattern $I = 2I_0[1 + \cos\delta\omega t]$, which demonstrates that $\Omega_C = \delta\omega$. These results are consistent with Eq. (3.4). In particular, $\delta\omega$ reverses its sign as m passes from $m = 1/2$ to $m = 3/2$, which is the signature of the optical radiation torque reversal from right-handed to left-handed. Nevertheless, this approach does not give access to sign of the rotational Doppler frequency shift, which we address in the next section.

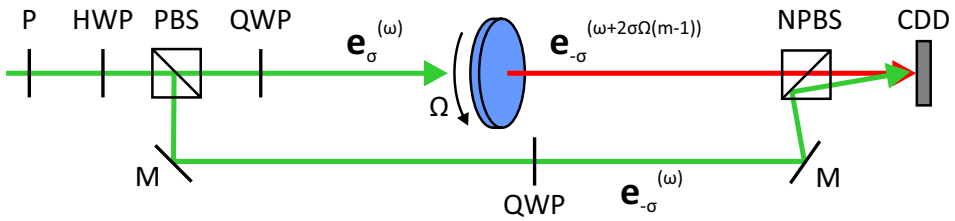

FIGURE 3.9: Scheme of the rotational Doppler frequency shift experimental set-up that corresponds to the non-collinear interference between output beam frequency $(\omega + \delta\omega)$ and reference beam with frequency (ω) that has $\mathbf{e}$ with similar circular polarization state $\mathbf{e}_{-\sigma}$.

3.3.2 Off-axis two-beam experiment and parametric study

Towards univocal determination of both sign and magnitude the rotational Doppler frequency shift, we have implemented rotational Doppler frequency shift experiment using non-collinear interference between transmitted and reference arms, as outlined in Fig. 3.9.

The resulting intensity distributions, in the (x, y) plane of the observation, correspond to $2|m|$-fork interference patterns, which are reminiscent of optical vortices carrying phase singularity $2m\sigma$. Such static patterns are illustrated in Fig. 3.10(a,b,c). As the sample rotates we observe the dynamics of the $2|m|$-fork patterns that behave differently depending on the parameters m, Ω and σ. This is illustrated by analyzing the dynamics of the oscillating intensity modulation at $x = x_0$, $I(x = x_0, y)$ as shown in Fig. 3.10(d,e,f) for the case of $\sigma\Omega > 0$. The interest of such patterns is that they allow direct identification of the sign of the frequency shift. Indeed, in present situation, the sign of the slope of patterns shown in Fig. 3.10(d,e,f) is that of $\delta\omega$.

In order to explain the frequency shift sign identification from the visual inspection of the fringing spatiotemporal patterns $I(x_0, y, t)$, let us analyze the wavevector's configuration that corresponds to interfering beams as outlined in Fig. 3.11. We refer as $k^s_{\omega'}$ to the wavevector of the output "signal" beam with the angular frequency $\omega' = \omega + \delta\omega$ and k^r_ω to the wavevector of the reference beam with the angular frequency ω. The relative angle between them, denoted as α, is positive in our experiment, see Fig. 3.11. Without loss of generality, let us assume that both output and reference fields are plane waves with similar values of amplitudes E_0 and polarization state along the x axis. The complex

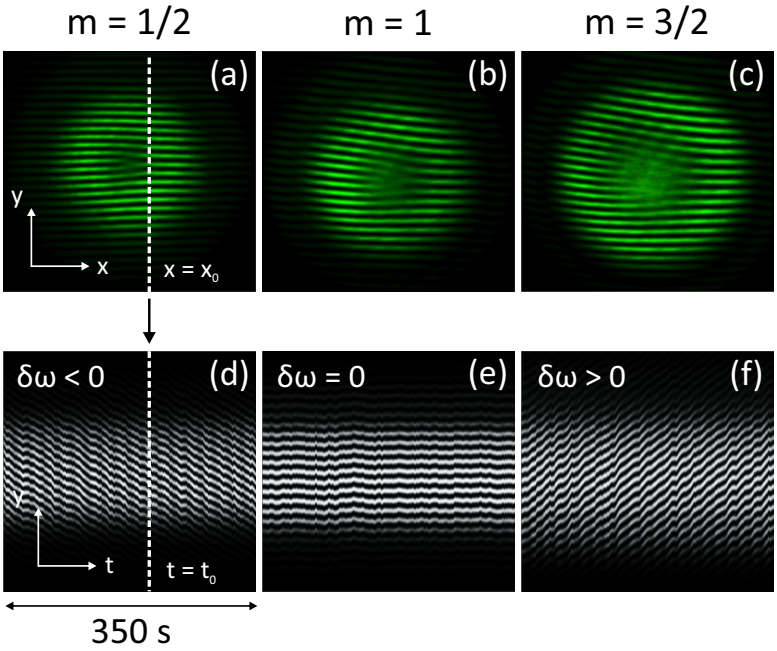

FIGURE 3.10: (a,b,c) Interference patterns formed between output beam emerged from the plates $m = \{1/2, 1, 3/2\}$ and off-axis reference beam with the similar circular polarization states $\mathbf{e}_{-\sigma}$. (d,e,f) Spatiotemporal patterns constructed from the interference patterns at $x = x_0$, $I(x_0, y, t)$ corresponding to the situation $\sigma\Omega > 0$. The drift direction implies determination of rotational Doppler frequency shift's sign, $\delta\omega > 0$, $\delta\omega = 0$ and $\delta\omega < 0$, respectively for the plates $m = \{1/2, 1, 3/2\}$.

representations of such fields correspond to $\mathbf{E}_s^{\omega'} = E_0 \exp[-i(\omega' t - k_s z)]\mathbf{e}_\sigma$ for the signal field and $\mathbf{E}_r^{\omega} = E_0 \exp[-i(\omega t - k_r \cos\alpha z + k_r \sin\alpha y)]\mathbf{e}_\sigma$ for the reference field. The intensity pattern resulting from coherent superposition of such fields in the plane of observation can be written as

$$I(x, y, t) = |\mathbf{E}_s^{\omega'} + \mathbf{E}_r^{\omega}|^2. \tag{3.5}$$

Inserting field expressions in Eq. (3.5) we get

$$I(x, y, t) = 2I_0[1 + \cos(k_r \sin\alpha y - \delta\omega t + \phi_0)], \tag{3.6}$$

where the ϕ_0 is constant phase factor that depends on the observation plane, note that $\mathbf{e}_\sigma \mathbf{e}_\sigma^* = 1$, whereas $\mathbf{e}_\sigma \mathbf{e}_{-\sigma}^* = 0$. The bright lines in the pattern $I(x, y, t)$ that correspond to spatiotemporal fringe in the (t, y) plane are given by following

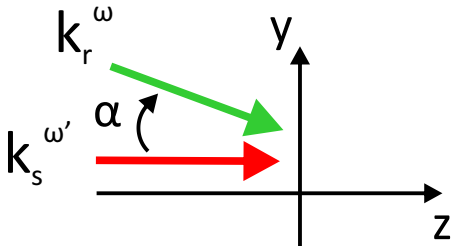

FIGURE 3.11: Scheme of the superposition of output beam emerged from the birefringent plate and tilted reference field in the (y, z) plane. Considered experimental arrangement corresponds to the $\alpha > 0$ situation where α is the angle between wave vectors of the output "signal" field $k_s^{\omega'}$ and reference arm field k_r^{ω}. Such superposition results in $2m$-fork interference patterns at the plane of observation as illustrated in Figure 3.10.

condition, $k_r \sin\alpha y - \delta\omega t + \phi_0 = 2\pi n$, where n is integer. Rewriting this condition with the following form,

$$y = Y_0 + \frac{\delta\omega}{k_r \sin\alpha} t\,, \tag{3.7}$$

where Y_0 is constant, allows us to confirm that the negative drift (towards $y < 0$) of the spatiotemporal fringes correspond to the negative frequency shift ($\delta\omega < 0$), whereas the positive drift (towards $y > 0$) of the spatiotemporal fringes correspond to the positive frequency shift ($\delta\omega > 0$), as illustrated in second row (d,e,f) of Fig. 3.10. No drift corresponds to the null frequency shift ($\delta\omega = 0$) in the case of the plate with topological charge $m = 1$. Notably, magnitude of the rotational

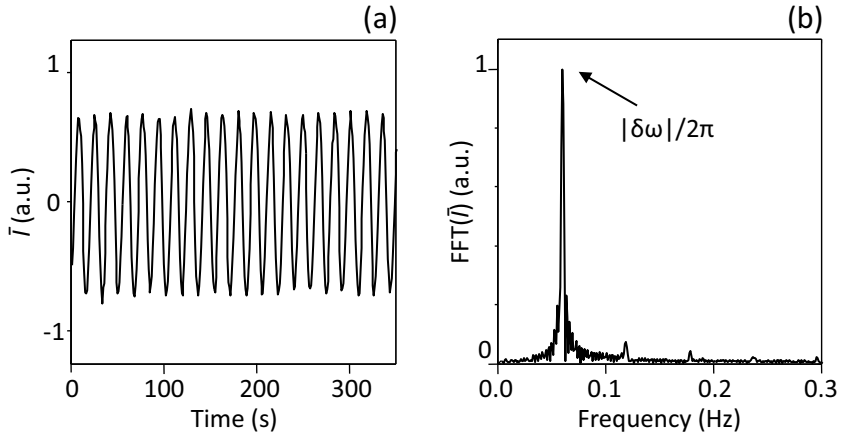

FIGURE 3.12: (a) Time-oscillating behavior of intensity signal $\bar{I}$ defined from interference patterns shown in Fig. 3.10. (b) Fast Fourier Transform (FFT) spectrum of the $\bar{I}$ that peaks at frequency $|\delta\omega|/2\pi$. The angular velocity of the plate equals to $\Omega = 0.37$ rad s^{-1}.

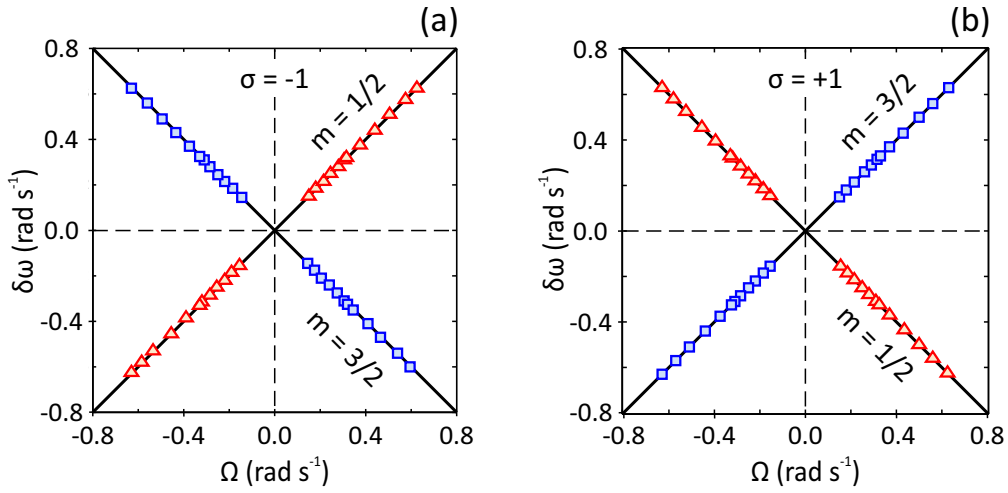

FIGURE 3.13: Rotational Doppler frequency shift dependence on the samples angular velocity Ω for $m = 1/2$ and $3/2$ and both circularly polarization handedness of the incident beam (a,b); solid lines correspond to the theoretical values given by the equation $\delta\omega = 2\sigma(m-1)\Omega$, markers correspond to experimental data.

Doppler shift also can be accessed from the spatiotemporal fringing patterns, by retrieving it from the slopes of Eq. (3.7), which however requires precise knowledge of the $k_r \sin\alpha$.

Instead, in order to determine magnitude of rotational Doppler shift we introduce the quantity

$$|\bar{I}(t)| = \int I(x_0, y, t)dy - \left\langle \int I(x_0, y, t)dy \right\rangle_t , \tag{3.8}$$

where $\langle . \rangle_t$ stands for time averaging. Corresponding intensity signal $I(x_0, y, t)$, when x_0 is large enough, can be represented by the following form,

$$I(x_0, y, t) \propto [1 + V(y)\cos(ay + \delta\omega t)]f(y) , \tag{3.9}$$

where $0 \leq V(y) \leq 1$ is the space-variant visibility of the fringes, a is a real constant with spatial periodicity of the fringing pattern, and $f(y) > 0$ is a real envelope function that depends on the reference beam intensity distribution in (x, y) plane. In the considered experiment, the value of x_0 corresponds to the beam waist value of the output field, as it can be qualitatively retrieved from the visual inspection of the patterns in first row (a,b,c) of Fig. 3.10. By inserting Eq. (3.9) in Eq. (3.8), we

get

$$\begin{aligned} \bar{I}(t) &\propto \int \cos(ay + \delta\omega t) V(y) f(y) dy \,, \\ &\propto \mathrm{Re}\left[e^{i\delta\omega t} \int e^{iay} V(y) f(y) dy \right] , \\ &\propto \cos(\delta\omega t + \arg C) \,, \end{aligned} \tag{3.10}$$

where $C = \int e^{iay} V(y) f(y) dy$ is constant. Hence, the Fast Fourier Transform (FFT) of the signal the $\bar{I}$ peaks at $\delta\omega/2\pi$, as shown in Fig. 3.12.

Implementing the above considered data analysis, we have performed a parametric study of the rotational Doppler frequency shift over the range corresponding to $|\delta\omega|/\omega \approx 10^{-17} - 10^{-16}$ for $m = \{1/2, 3/2\}$. In addition, we have considered both handedness of incident circularly polarization, $\sigma = \pm 1$. The results are summarized in Fig. 3.13 that represents the rotational Doppler frequency shift ($\delta\omega$) dependence on angular velocity of the plate (Ω). The solid lines refer to theoretical results given by Eq. (3.4), whereas markers refer to the experimental results, from which we can imply a proper agreement between experimental data and theoretical predictions. This concludes the precise experimental determination of rotational Doppler shift, which implies the quantitative identification of left-handed optical radiation torque when $m > 1$.

3.4 Single beam experiment

We have also explored left-handed radiation torque demonstration using a single beam (reference-free) rotational Doppler experiment. The experimental setup is outlined in Fig. 3.14 and consists of linearly polarized (along x axis in practice) Gaussian field that is normally incident to the rotating sample with topological charge $m = \{1/2, 1, 3/2\}$. Such field can be described as a coherent superposition of two orthogonal circularly polarized Gaussian beams with identical amplitudes. This decomposition implies that each orthogonal circularly polarized component exerts torques on the sample of equal magnitudes but opposite signs. Although the total torque exerted by linearly polarized field is zero, we will see that, the optomechanical contributions produced by independent circularly components can

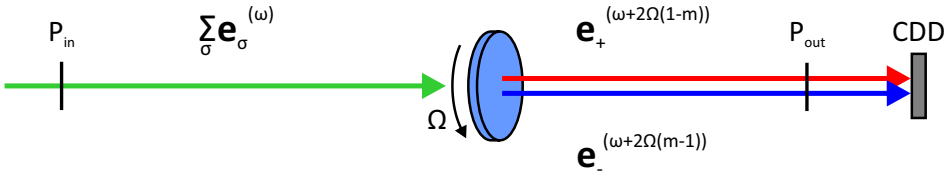

FIGURE 3.14: Scheme of the experimental set-up that corresponds to reference-free rotational Doppler frequency shift experiment used to record interference patterns between frequency shifted circularly polarized components of the output beam (common path interferometer). We consider normal incidence of linearly polarized (along x axis) Gaussian beam, with waist radius $w \simeq 1$ mm, on the rotating slab of topological charge m. The interference pattern results from the projection of output field along the y direction by using linear polarizer.

be assessed.

First, let us describe the output field after the sample at rest $\Omega = 0$

$$\mathbf{E}_{\text{out}}^{(m,\Omega=0)} = \mathbf{J}_{(m)}(1/\sqrt{2}, 1/\sqrt{2})^T = \cos(2m\varphi)\mathbf{x} + \sin(2m\varphi)\mathbf{y}, \tag{3.11}$$

where $(1/\sqrt{2}, 1/\sqrt{2})^T$ is the Jones vector of the incident linearly polarized field in circular basis $(\mathbf{e}_+, \mathbf{e}_-)$ and $J_{(m)}$ is the Jones matrix associated with the sample, as introduced in section 1.2. Such a field represents the coherent superposition of two contra-circularly polarized vortex beams with opposite topological charges $\pm 2m$, which form a field with an azimuthally varying linear polarization state. Corresponding beams are known as a vector beams; see for example Ref. [67]. Then, the idea is to place a linear polarizer aligned along the y axis after the rotating sample, as outlined in Fig. 3.14. The interference between the two orthogonal circularly polarized components from sample thus lead to intensity modulation. Indeed, a $4|m|$-fold interference pattern is obtained in the (x, y) plane as shown in lower insets of Fig. 3.15(a,b,c), which correspond to the patterns at rest. In fact, projection on y axis leads to modulation of intensity profile after polarizer that is proportional to $I \approx \sin^2(2m\varphi)$ (see Eq. (3.11)). Once the sample is rotated at constant angular velocity Ω, the intensity patterns express distinct dynamical behavior as shown in Fig. 3.15(a,b,c), where time evolutions of patterns correspond to two full rotations of the slabs ($T \simeq 30$ s). Similarly to the two-beam experiment, we observe handedness reversal between $m = 1/2$ to $m = 3/2$, and static situation for $m = 1$.

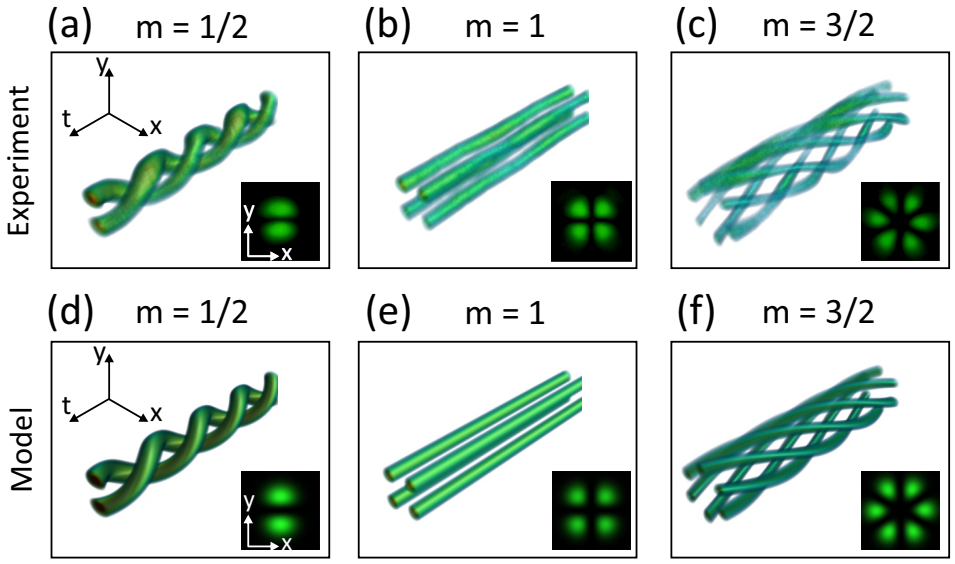

FIGURE 3.15: The spatiotemporal interference patterns and their time evolutions that correspond to twice full rotations ($T = 30s$) of the samples following to the experimental set-up outlined in Fig. 3.14. The lower insets represent interference patterns between two orthogonal circularly polarized components of the output beam formed in (x, y) plane. The first column corresponds to sample with topological charge $m = 1/2$ (a, d), second column to $m = 1$ (b, e), and third column to $m = 3/2$ (c, f); patterns in upper row are experimental data whereas patterns in lower row are model simulations.

In fact, such spatiotemporal behavior of the patterns can be described by introducing the Jones dynamical matrix that corresponds to the sample rotating with constant angular velocity Ω along z axis,

$$\mathbf{J}_{(m)} = \begin{pmatrix} 0 & e^{-2i[m\varphi+(1-m)\Omega t]} \\ e^{+2i[m\varphi+(1-m)\Omega t]} & 0 \end{pmatrix}, \tag{3.12}$$

similarly to the static Jones matrix introduced for such media in the section 1.2. The output field dynamical behavior is then obtained by applying previous the Jones matrix to the incident linear polarization Jones vector in circular basis,

$$\begin{aligned} \mathbf{E}_{\text{out}}^{(m,\Omega)} &= \mathbf{J}_{(m)}(1/\sqrt{2}, 1/\sqrt{2})^T, \\ \mathbf{E}_{\text{out}}^{(m,\Omega)} &= \cos(2[m\varphi + (1-m)\Omega t])\mathbf{x} + \sin(2[m\varphi + (1-m)\Omega t])\mathbf{y}. \end{aligned} \tag{3.13}$$

Assuming that radial dependence of the output beam is characterized by the form of Laguerre-Gaussian beam, with azimuthal index $l = 2m$ and radial index $p = 0$, the resulting intensity patterns are described as

$$I(r,t) = (r/2)^{4|m|} \exp(-2r^2/w^2) \sin^2(2[m\varphi + (1-m)\Omega t]) \tag{3.14}$$

where w is the beam waist radius. We summarize analysis in Fig. 3.15(d,e,f) as in experiment, where the lower insets correspond to the static intensity distributions while upper insets correspond to time evolutions of such intensity distributions. A fair agreement with the experimental data is obtained.

3.5 Generalization of the study

3.5.1 Influence of the birefringent phase delay

In this section we address to the question whether left-handed torque manifests in the case of the birefringent phase retardation other than half-wave plate condition discussed in previous sections, namely $\Delta \neq \pi$. In fact, as discussed in section 1.3,

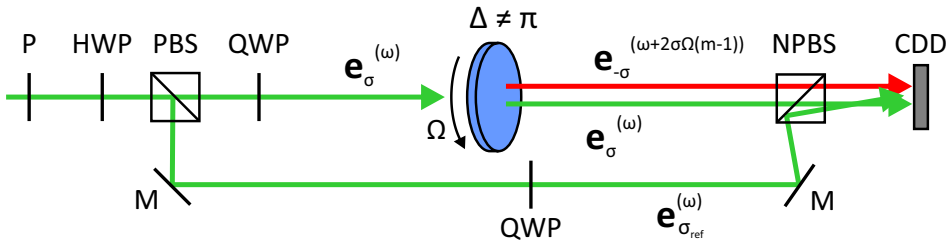

FIGURE 3.16: Scheme of the rotational Doppler frequency shift experimental set-up corresponding non-collinear interferometer with de-tuned birefringent phase delay configuration, $\Delta = 0.84\pi$. Output field is elliptically polarized and consists of superposition of two orthogonal fields with opposite circularly polarization states $\sigma = \pm 1$. Inserting a circular polarizer after output field selects one or other component to interfere with the non-collinear reference arm.

the torque expression in that case is

$$\Gamma_z^{\mathrm{soi}(\sigma)} = 2\frac{P}{\omega}\sigma(1-m)\sin^2\left(\frac{\Delta}{2}\right). \tag{3.15}$$

The factor $\eta = \sin^2(\Delta/2)$ in the above equation represents the fraction of photons that transferred angular momentum to the sample. In other words, these photons are those doing work on the slab. Thus, the energy conservation for arbitrary birefringent phase delay case must be written per "working" photons, replacing P by ηP in Eq. (3.2) that gives

$$\Gamma_z^{\mathrm{soi}}\Omega + \eta\frac{P}{\omega}\delta\omega = 0\,. \tag{3.16}$$

Then, by combining Eq. (3.15) and (3.16) one gets a rotational Doppler frequency shift expression that is unchanged with respect to the half-wave plate situation, this is Eq. (3.4).

We have explored such a situation experimentally with the same samples as used in the previous sections, by using incident wavelength 632.8 nm instead of 532 nm, thus obtaining $\Delta = (532/632.8)\pi = 0.84\pi$. We have implemented a rotational Doppler frequency shift experiment that consists of a non-collinear interferometer as outlined outlined in Fig. 3.16, where we consider the coherent superposition of the output vortex beam and reference Gaussian beam. To determine the rotational Doppler shift we have used a similar analysis as the one presented

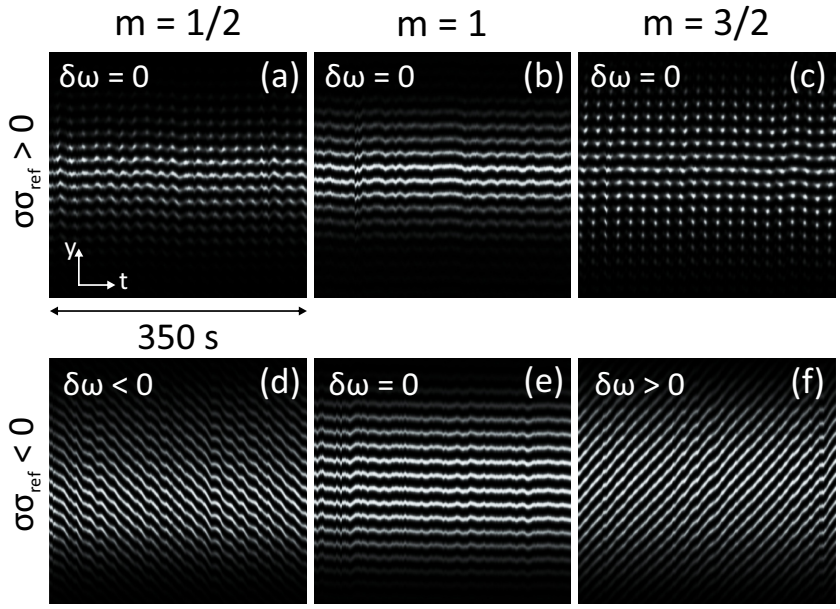

FIGURE 3.17: Spatiotemporal fringing patterns retrieved from the prerecorded interference patterns using experimental setup outlined in Fig. 3.16. First row represents $\sigma\sigma_{\text{ref}} > 0$ configuration of the input and reference arm circular polarization state corresponding to the samples $m = 1/2$ (a), $m = 1$ (b) and $m = 3/2$ (c), second row represents $\sigma\sigma_{\text{ref}} < 0$ configuration of the input and reference arm circular polarization state corresponding to the samples $m = 1/2$ (a), $m = 1$ (b) and $m = 3/2$ (c)

in section 3.3.2 independently for both output orthogonal circular polarization states $\pm\sigma$ by placing circular polarizer after the sample that selects one or another polarization component. As we superpose the output component with the reference arm of same polarization handedness ($\sigma_{\text{ref}} = \pm\sigma$) we obtain fringing patterns, as described in that section.

The results are shown in Fig. 3.17 for the samples of topological charge $m = \{1/2, 1, 3/2\}$ and two situations corresponding to the input and reference arm polarization handedness, $\sigma\sigma_{\text{ref}} > 0$ in the first row, and $\sigma\sigma_{\text{ref}} < 0$ in the second row. Indeed, photons that did not flipped their spin angular momentum, hence did not participate to spin-orbit interaction, which implies no drift of the spatiotemporal fringing pattern. In contrast, in the case of the photons that have flipped their spin, coupling with their orbital momentum, we observe positive, negative, or zero drift of the spatiotemporal fringes depending on the m, σ and Ω, as discussed in the previous section.

We have also determined $\delta\omega$ implementing the same analysis as discussed in section 3.3.2 and quantitatively validated that the rotational frequency shift is unchanged from the preceding case. Qualitatively this can be validated from comparing the spatiotemporal patterns in Fig. 3.17(d,e,f) and patterns in Fig. 3.10(d,e,f).

All the above considerations generalize the proposed concept of left-handed optical radiation torque to arbitrary values of the birefringent phase retardation associated with the medium.

3.5.2 Influence of the incident polarization state

Considering more general arbitrary elliptical polarized beam, the above results remain valid. Indeed, as we have introduced in chapter 1, any polarization can be presented as a superposition of left- and right-handed circular polarization basis, with such approach we have obtained the optical radiation torque expression involved in spin-orbit interaction of light for any superposition of left- and right-handed circular polarization states as

$$\Gamma_z^{\text{soi}} = 2\frac{P}{\omega}\sin(2\chi)(1-m)\sin^2(\Delta/2)\ . \tag{3.17}$$

We recall that spin angular momentum per photon equals $s_z = \sin(2\chi)\hbar$, where χ is ellipticity angle (see section 1.2), the sign of the incident spin angular momentum is either positive or negative depending the handedness prescribed by the rotation of electrical vector of light field, which corresponds to $0 < \chi \leq \pi/4$ and $-\pi/4 \leq \chi < 0$, respectively. Hence, the optical torque considerations discussed in the preceding sections remain qualitatively valid up to the multiplying factor $\sin(2\chi)$, and $s_z\Gamma_z^{\text{soi}} < 0$, when $m > 1$ for whatever s_z. Thus, left-handed torque manifests for arbitrary incident polarization state, and in the special case of the linear polarization when net torque is zero still the torque reversal can be revealed (see section 3.4).

CHAPTER 4

Optical torque reversal: towards direct observations

In the preceding chapter we introduced the concept of left-handed optical torque and experimentally scrutinized its manifestation by performing series of rotational Doppler frequency shift experiments. Nevertheless, the latter approach consists in indirect optomechanical observations, performed by probing consequences of an optical torque on light itself instead of matter due to impractical optomechanics of centimeter-sized macroscopic samples. In this chapter we report on experimental attempts to observe left-handed optical radiation torque in a direct manner. In section 4.1 we discuss possible experimental routes of optimization by evaluating the optical torque induced rotation of spin-orbit optical elements. We present our experimental attempts with millimeter-scale azimuthally varying birefringent glass samples in section 4.2, which correspond to miniaturized and high-order versions of previously used macroscopic samples. Then, in section 4.3, we report on design, fabrication and structural characterization of metallic micro-structures that are another type of candidate in our quest. Optical performances of fabricated samples are experimentally evaluated and discussed as part of possible optomechanical implementation. The chapter is concluded by section 4.4, where we address to a purely dielectric option at the microscale that is likely to be the one allowing the sought direct observation of torque reversal. We report on our first fabrication attempts and expected practical challenges that one has to take on in order to complete the initial goal.

4.1 General considerations and analysis

The main motivation of our investigations reported in this chapter is to observe left-handed optical radiation torque "in action", in other words our objective is to observe the light induced rotation of the spin-orbit coupler that satisfies the $\sigma f < 0$ condition, $f = \Omega/2\pi$ being the signed rotating frequency of the element under circularly polarized incident field with helicity σ. To achieve this, in what follows we analyze possible optimizations of azimuthally varying birefringent optical elements. This is done in the general framework accounting not only for the material birefringence (as done so far in previous chapters) but also for absorption effects, which includes possible linear dichroism. Indeed, as seen in section 1.1.3, absorption itself always leads to right-handed torque (see Fig. 1.7), while dichroism (polarization dependent absorbtion) is known to affect on spin-orbit interaction of light in the framework of space-variant birefringent plates, as reported in [68].

Quantitative analysis is made by considering circularly polarized plane wave $\mathbf{E}_{\text{in}} = E_0 e^{-i(\omega t - kz)}\mathbf{e}_\sigma$ that propagates through azimuthally varying birefringent plate, with thickness L whose input facet is located at $z = 0$. Introducing complex refractive index $\tilde{n}_{\parallel,\perp} = n_{\parallel,\perp} + in'_{\parallel,\perp}$ the output field at $z = L$ can be obtained in the laboratory frame using the Jones formalism as done in chapter 1 but using the complex refractive indices. Namely,

$$\mathbf{E}_{\text{out}} = E_0\, e^{-i\omega t}\, \hat{\mathbf{R}}_z(-\psi) \begin{pmatrix} e^{ik\tilde{n}_\parallel L} & 0 \\ 0 & e^{ik\tilde{n}_\perp L} \end{pmatrix} \hat{\mathbf{R}}_z(\psi)\, \mathbf{e}_\sigma\,. \tag{4.1}$$

Then we express the output field in the circular polarization basis,

$$\mathbf{E}_{\text{out}} = (\mathbf{E}_{\text{out}} \cdot \mathbf{e}^*_\sigma)\, \mathbf{e}_\sigma + (\mathbf{E}_{\text{out}} \cdot \mathbf{e}^*_{-\sigma})\, \mathbf{e}_{-\sigma}\,, \tag{4.2}$$

where asterisk refers to complex conjugation. After calculation, one gets, up to the unimportant pure phase factor $e^{-i\omega t + ikn_\perp L + i\frac{\Delta}{2}}$, a field at $z = L$

$$\mathbf{E}_{\text{out}} = E_0 \tau \left[\cos\left(\frac{\tilde{\Delta}}{2}\right) \mathbf{e}_\sigma + i \sin\left(\frac{\tilde{\Delta}}{2}\right) e^{i2\sigma m\varphi}\, \mathbf{e}_{-\sigma} \right]. \tag{4.3}$$

where $\tau = e^{-k(n'_\parallel + n'_\perp)L/2}$, and $\tilde{\Delta} = \Delta + i\Delta'$, with $\Delta' = k(n'_\parallel - n'_\perp)L$. Noticeably above

formula allows to quantify the role of absorption in the generation of optical orbital angular momentum. Indeed vortex generation purity parameter, as defined in chapter. 1 (see Eq. (1.22)), expresses here as

$$\eta = \frac{1}{2}\left[1 - \frac{\cos\Delta}{\cosh\Delta'}\right]. \tag{4.4}$$

The above expression thus points out that the purity is decreased in the presence of dichroism ($\Delta' \neq 0$) whereas the half-wave plate condition ($\Delta = \pi$ modulo 2π) remains desirable to optimize it. Also, this indicates that average absorption ($\tau \neq 1$) is not at play in purity, but only plays a role in the efficiency of the process by lowering the magnitude of the contra-circularly polarized output component $\mathbf{e}_{-\sigma}$ of Eq. (4.3).

That said, the optical torque along the beam propagation direction can be evaluated from Eq. (4.3) by writing down the angular momentum balance between input and scattered field. For the sake of generality, here we are also considering the possible presence of reflected field, which leads us to introduce the reflectance $\mathcal{R}$, the transmittance $\mathcal{T}$, and the absorbance $\mathcal{A}$, noting the relationship $\mathcal{R} + \mathcal{T} + \mathcal{A} = 1$. The next step is to evaluate the relevant quantities (P_j, s_z^j, l_z^j) with $j = (\mathrm{i}, \mathrm{t}, \mathrm{r})$ where i, t and r refer to incident, transmitted and reflected fields, and to apply the angular momentum balance. For the incident field one straightforwardly gets

$$\text{Input field} \begin{cases} P_\mathrm{i} = P\,, \\ s_z^\mathrm{i} = \sigma\hbar\,, \\ l_z^\mathrm{i} = 0\,. \end{cases}$$

For the reflected field, neglecting the corrections associated with mismatch between the amplitude reflection coefficients along and perpendicular to the local optical axis of the spin-orbit element, one can consider that the incident spin angular momentum projection along the z axis is preserved at reflection, as is the case for a usual mirror at normal incidence. This gives

$$\text{Reflected field} \begin{cases} P_\mathrm{r} = \mathcal{R}P\,, \\ s_z^\mathrm{r} = \sigma\hbar\,, \\ l_z^\mathrm{r} = 0\,. \end{cases}$$

The case of the transmitted field is then treated by noting that, from Eq. (4.3),

$$s_z^{\mathrm{t}} = \frac{\left|\cos\frac{\tilde{\Delta}}{2}\right|^2 - \left|\sin\frac{\tilde{\Delta}}{2}\right|^2}{\left|\cos\frac{\tilde{\Delta}}{2}\right|^2 + \left|\sin\frac{\tilde{\Delta}}{2}\right|^2}\sigma\hbar \tag{4.5}$$

and that, on the other hand,

$$l_z^{\mathrm{t}} = \frac{\left|\sin\frac{\tilde{\Delta}}{2}\right|^2}{\left|\cos\frac{\tilde{\Delta}}{2}\right|^2 + \left|\sin\frac{\tilde{\Delta}}{2}\right|^2} 2\sigma m\hbar\,. \tag{4.6}$$

This gives after calculations the following parameters for the transmitted field:

$$\text{Transmitted field} \begin{cases} P_{\mathrm{t}} = \mathcal{T}P\,, \\ s_z^{\mathrm{t}} = (1-2\eta)\sigma\hbar\,, \\ l_z^{\mathrm{t}} = 2m\sigma\eta\hbar\,. \end{cases}$$

Optical torque expression is thus obtained from

$$\Gamma_z = \frac{P_{\mathrm{i}}}{\hbar\omega}(s_z^{\mathrm{i}} + l_z^{\mathrm{i}}) - \frac{P_{\mathrm{r}}}{\hbar\omega}(s_z^{\mathrm{r}} + l_z^{\mathrm{r}}) - \frac{P_{\mathrm{t}}}{\hbar\omega}(s_z^{\mathrm{t}} + l_z^{\mathrm{t}}) \tag{4.7}$$

that eventually gives, making use of $\mathcal{R} + \mathcal{A} + \mathcal{T} = 1$:

$$\Gamma_z = \frac{P}{\omega}\sigma\left[\mathcal{A} + 2\mathcal{T}\eta(1-m)\right]. \tag{4.8}$$

The above expression clearly emphasizes the detrimental role of absorbance towards the observation of torque reversal since the term $\mathcal{A}$ actually corresponds to a purely "right-handed" torque contribution. In addition, low transmittance elements are not favorable while the condition $m > 1$ remains the basic requirement for torque reversal. Dichroism is also detrimental since it reduces the magnitude of purity parameter η following Eq. (4.4).

To evaluate the mechanical consequences of the above presented torque we assume that the sample is immersed in a fluid (e.g. water) and is free to rotate, which represents a typical experimental scheme to observe a direct optomechanical effect. The light induced rotation angular velocity is thus obtained at steady state

from the balance between (i) the optical radiation torque Γ_z driven by spin-orbit interaction of light and (ii) the viscous torque Γ_z^{visc}, exerted by the fluid surrounding the rotating sample, namely, $\mathbf{\Gamma}_z + \mathbf{\Gamma}_z^{\text{visc}} = 0$. Considering infinitely thin disk in the framework of hydrodynamic Stokes approximation limit (i.e. inertial effects are discarded) the viscous torque expression is [69]:

$$\mathbf{\Gamma}_z^{\text{visc}} = -\frac{32}{3}\mu R^3 \Omega \mathbf{e}_z \tag{4.9}$$

where μ is the dynamic viscosity of the fluid ($\mu \simeq 1$ mPa s for water at room temperature), R is the radius of sample, and Ω its angular frequency. Combining Eq. (4.8) and Eq.(4.9) the spinning disk rotation frequency $f = \Omega/2\pi$ is

$$f = \frac{3P\sigma}{64\pi\omega\mu R^3}\left[\mathcal{A} + 2\mathcal{T}\eta(1-m)\right]. \tag{4.10}$$

With the aim at exploring experimentally accessible situations for observing optical torque reversal, next we perform a few simulations of the dependence of the product σf, recalling that we search maximal value for $|\sigma f|$ while having $\sigma f < 0$. For a start, we consider incident power $P = 1$ W, no absorption ($\mathcal{A} = 0$, hence

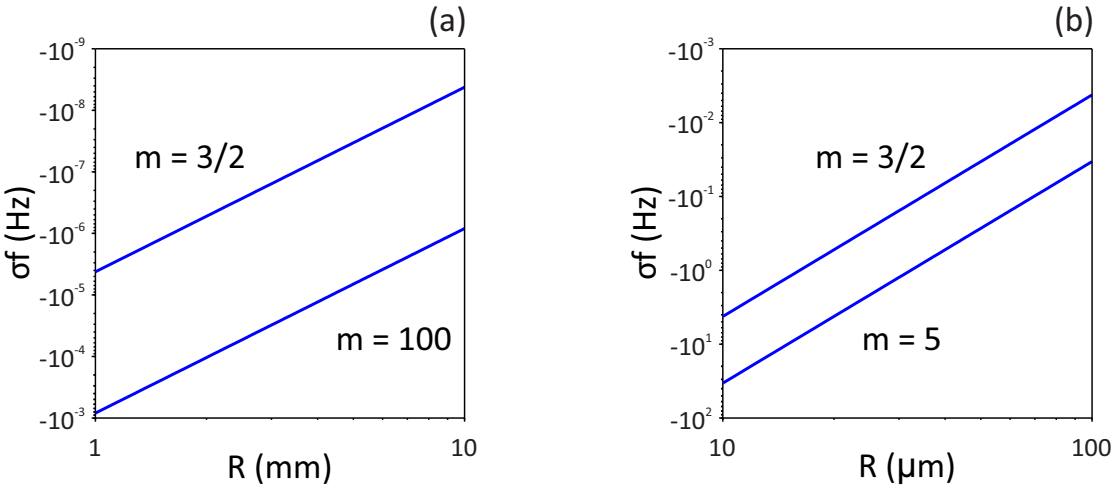

FIGURE 4.1: Dependence of σf on the radius R of the space-variant birefringent element corresponding to the range of (a) millimeter and (b) tens of micrometer for material topological charges $m = \{3/2, 100\}$ and $m = \{3/2, 5\}$. Simulations are done under $P = 1$ W, assuming $\mathcal{A} = 0$ and, $\mathcal{T} = 1$, $\Delta = \pi$ and $\Delta' = 0$.

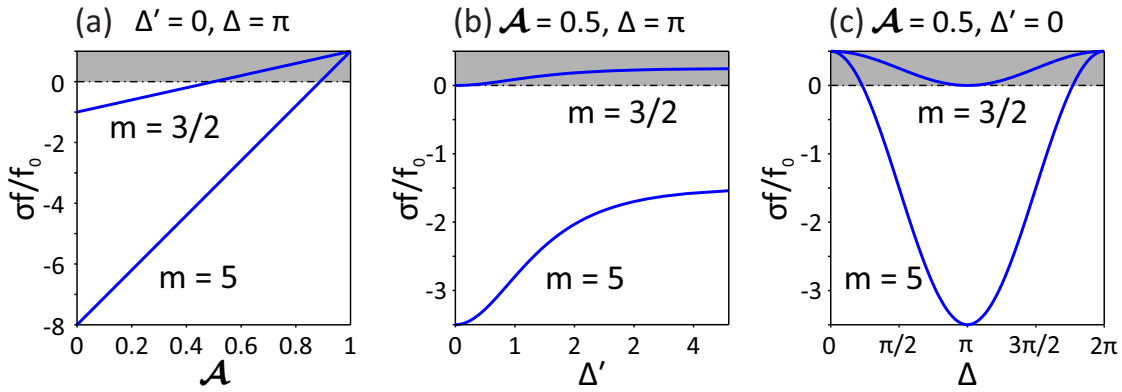

FIGURE 4.2: Dependence of $\sigma f/f_0$ on (a) absorption parameter $\mathcal{A}$ with $\Delta' = 0$ and $\Delta = \pi$, (b) dichroism parameter Δ' with $\mathcal{A} = 0.5$ and $\Delta = \pi$, and (c) birefringence phase retardation Δ with $\mathcal{A} = 0.5$ and $\Delta' = 0$. Darkened areas correspond to right-handed configuration, $\sigma f/f_0 > 0$. $\mathcal{R} = 0$ is assumed in all cases.

$\Delta' = 0$), fully transmissive element ($\mathcal{T} = 1$), and optimal half-wave plate condition ($\Delta = \pi$, hence $\eta = 1$ since $\Delta' = 0$). Figure 4.1 displays the dependence of σf on the sample radius R considering miniaturization of the samples used in chapter 3 in the sub-centimeter domain (Fig. 4.1(a)) and in the sub-millimeter domain (Fig. 4.1(b)), for the smallest topological charge m that could lead to torque reversal ($m = 3/2$) and also for high-value (up to $m = 100$). In the millimeter scale, the practical observation of sample rotation is likely only for high topological charges, for example with $m = 100$ spinning frequency of the order of mHz is expected. On the other hand, comfortable observation of light induced rotation is expected for samples with tens of micrometer size, where f frequencies of higher than Hz are readily accessible with moderate m values. Noteworthy, above choice for m values in the macro (Fig. 4.1(a)) and micro (Fig. 4.1(b)) cases is not made arbitrarily. Indeed, as shown in the next sections, this corresponds to accessible material structuring in practice.

Further investigation is performed by looking at the reduced frequency

$$\sigma f/f_0 = \mathcal{A} + 2\mathcal{T}(1 - m) \tag{4.11}$$

where $f_0 = 3P/(64\pi\omega\mu R^3)$. By doing so, we can focus on the role of the key parameter $\mathcal{A}$, Δ' and Δ, assuming $\mathcal{R} = 0$. This is summarized in Fig. 4.2 for a set of representative parameters for $m = 3/2$ and $m = 5$. The take-home message of

this analysis is the following :

- Absorption ($\mathcal{A}$) is always detrimental to optical torque reversal since absorbed incident optical spin angular momentum has a purely "right-handed" contribution to the total torque. This is illustrated in Fig. 4.2(a).
- Dichroism (Δ') is always detrimental to optical torque reversal since it lowers the amount of scattered light carrying orbital angular momentum. This is illustrated in Fig. 4.2(b).
- Birefringent phase retardation (Δ) should be set as close as possible to the half-wave condition whatever the situation. This is illustrated in Fig. 4.2(c).

To conclude, smaller is better and transparency should be privileged. Fabrication technologies allowing easy tuning of retardance will be favored, however, of course, practical restrictions may generally lead to trade-off. In the next sections, two options are considered, first at millimeter scale, then at micrometer scale.

4.2 Dielectric approach at the millimeter scale

4.2.1 Samples: high-order nanostructured glass q-plates

After the first indirect demonstration of optical torque reversal using centimeter-size nanostructured glass q-plates, our choice was to consider a miniaturization strategy combined with the use of high order topological charge m. This was done in collaboration with Altechna R & D company and spin-orbit elements with $m = \{10, 25, 50, 75, 100\}$ were fabricated by direct femtosecond laser writing technique in the bulk of silica glass. Each sample consists of a disk of radius $R = 2.5$ mm and height $H = 1$ mm. The structured part correspond to a volume defined by $R_1 < r < R_2$ with $R_1 = 250$ μm and $R_2 = 2.25$ μm, over a height $h = 74$ μm (which ensures $\Delta = \pi$), buried roughly 100 μm below the surface, as sketched in Fig. 4.3. The choice of $R_1 \neq 0$ and $R_2 < R$ allows preventing sample damage as a result of post fabrication stresses. An example with $m = 10$ is shown in Fig. 4.3(c,d,e), where azimuthal structuring of the element is validated by observations between crossed linear polarizers. Overview of a full set of sample is shown in Fig. 4.4.

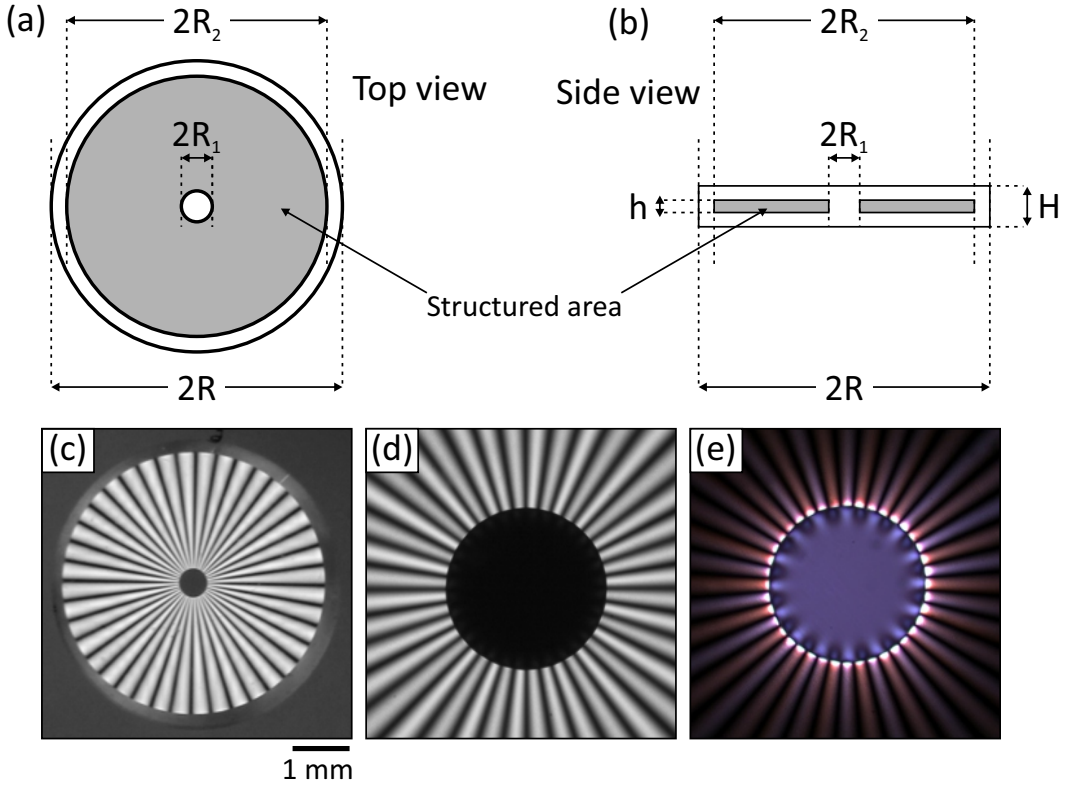

FIGURE 4.3: Illustration of the fabricated sample with diameter $2R = 5$ mm showing top view (a) and side view (b) structured regions. Not to scale. (c) Example of observation between crossed linear polarizers for $m = 10$, (d) zoomed central part, and (e) inner circle tensions distribution unveiled by adjusting the incident polarization angle and the camera exposure.

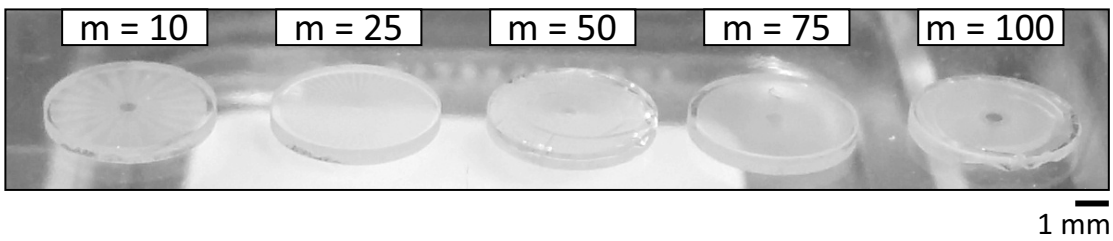

FIGURE 4.4: Image of millimeter scale spin-orbit glass elements set with topological charges $m = \{10, 25, 50, 75, 100\}$ and diameter $2R = 5$mm.

Further miniaturization of such glass samples is practically challenging since bulk structuring of sample implies minimal thickness to achieve optimal form birefringent phase retardation condition $\Delta = \pi$ without fabrication-induced surface damages.

4.2.2 Experimental approach

Recalling that observation of spinning disks ideally implies samples to be free to rotate, one needs to conceive an experimental approach that gets rid of nearby solid surface. Since it is unrealistic to consider a stable long-term experiment where buoyancy is strictly compensated using a single surrounding fluid (i.e. bulk approach), instead we propose a surface approach. The idea is to place the samples on surface of a high surface tension liquid that could hold it and in practice water is a very good candidate owing to its large surface tension and low dynamic viscosity.

Another practical restriction is to hold sample at fixed position to prevent active adjustment of the laser beam illumination and ease the spinning detection protocol. This is done by implementing a self-centered strategy, holding the sample at the bottom part of a droplet suspended upside-down on a glass substrate, as shown in Fig. 4.6(a). Indeed, gravity thus acts as an efficient way to reach perfect and stable centering. In practice, this is done by putting a droplet of water on a glass coverslip. Then the hanged droplet is put in contact (from top) with the sample sitting on an arbitrary non-sticky substrate. By doing so, "capillary tweezers" is achieved (see Fig. 4.5), and we obtained the situation sketched and shown in practice in Fig. 4.6(a,c) where the system is isolated from external air flows by a

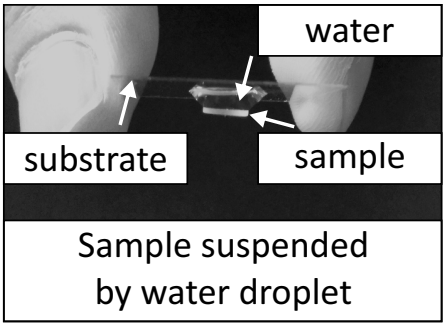

FIGURE 4.5: Image of the millimeter scale q-plate suspended by water droplet.

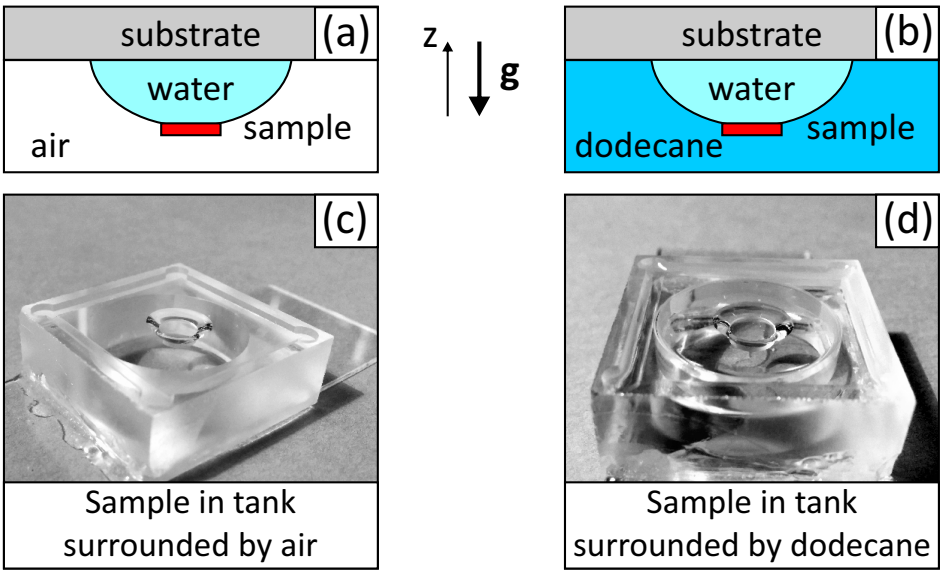

FIGURE 4.6: Illustration of experimental configuration corresponding self-centered sample suspension using water droplet due to the gravitational force ($\mathbf{g}$). (a) A tank is used to avoid air flows. (b) A tank is filled with second fluid (dodecane) to avoid air circulations. (c,d) Images of practical implementation of (a,b).

surrounding tank. Once this is set, we illuminate the sample with a circularly polarized Gaussian beam and image the sample with a white light source. However, laser assisted evaporation of the droplet prevents from stable long-term observation. We have eliminated evaporation issues by filling the tank with a liquid that is immiscible with water and has roughly similar dynamic viscosity (e.g. dodecane $\mu \simeq 1.24$ mPa s), see Fig. 4.6(b,d). Optomechanical experiment is then performed with the latter option.

Before discussing experimental results, let us estimate the frequency of the rotation associated with considered approach assuming $P = 1$ W illumination, non dissipative light-matter interaction ($\mathcal{A} = 0$), and considering maximal optical vortex generation efficiency ($\Delta = \pi$) one gets from Eq. (4.10) $f = 0.05$ mHz for $m = 100$, hence $\approx 65°$ rotation within one hour of steady state illumination. However, in practice, no rotation of sample was observed, see Fig. 4.7. This might be expected by uncontrolled effects associated with the contact line between the two liquids and sample at its periphery. We were unable to properly understand and solve this issue, which led us to consider further miniaturization of samples, as discussed in next section.

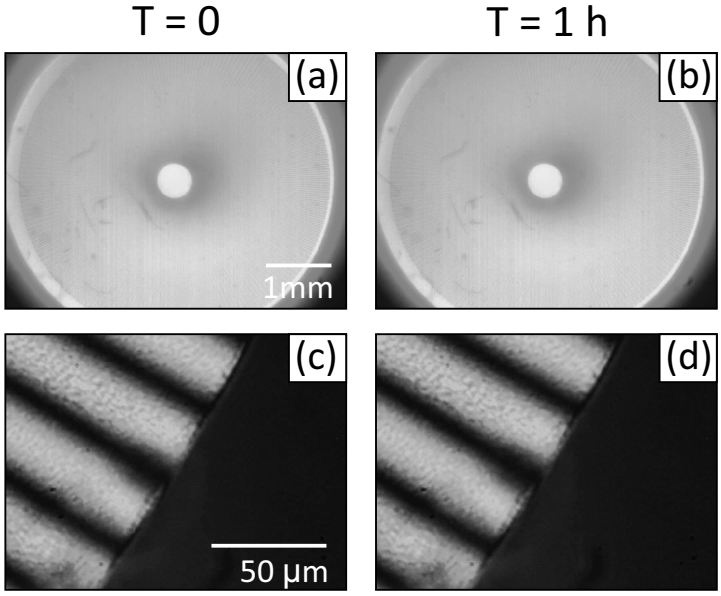

FIGURE 4.7: Images of the sample ($m = 100$) suspended by the water droplet, between almost crossed linear polarizers using (a,b) low magnification to observe full sample and (b,c) higher magnification to observe local angular displacement of the sample, since relatively modest rotation is expected. Panels (a,c) correspond to initial illumination time while panels (b,d) refer to the situation after on hour illumination ($P = 1$ W). As we can judge by itself, no displacement is observed.

4.3 Metallic approach at the micrometer scale

4.3.1 Design and fabrication of samples

To obtain micrometer scale spin-orbit couplers we have followed approach introduced in reference [19] based on material surface subwavelength structuring for mid-infrared light, by implementing it for visible light, which implies using nanofabrication tools. We opted for discrete structuring instead of continuous design to ease the practical implementation and thin gold layer (few hundreds of nm) was chosen as the material to be structured. Indeed, it has been shown that such system could provide with half-wave retardance [70], as desired in our case.

In practice, we have followed numerical analysis reported in Ref. [70], where authors studied radial and azimuthal polarization convertors and demonstrated

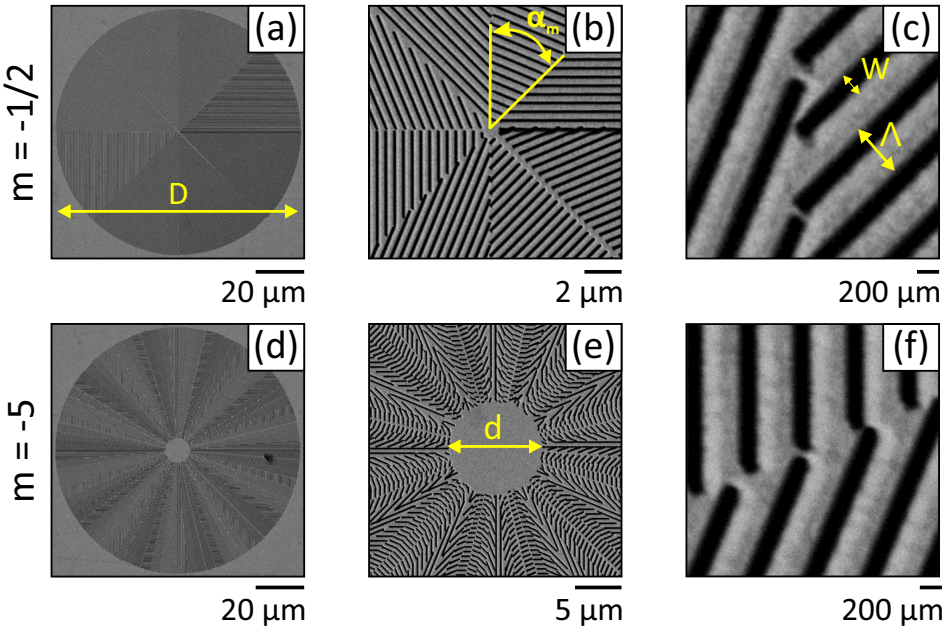

FIGURE 4.8: Scanning electron microscopy images of the metallic birefringent plates corresponding to the fundamental topological charge $m = -1/2$ (a,b,c) and high order $m = -5$ (d,e,f). The plates are fabricated over $D = 100$ μm diameter with $H = 300$ μm thickness, and 500 μm grating period with $W = 160$ nm slit width. Each structure is made of $16|m|$ sectors with angular width $\alpha_m = \pi/(8|m|)$ and $\pi/8$ angular step for the slit orientation between adjacent sectors, see panels (b) and (e). To preserve proper azimuthal resolution of high order plates, the central part is unstructured over a diameter $d = 10$ μm.

their operation with linear to radial polarization conversion at wavelength 633 nm. We have designed $D = 100$ μm diameter structures to operate at wavelength 532 nm, which correspond to the choice of gold layer thickness $H = 300$ nm, grating period $\Lambda = 500$ nm, and slit width $W = 160$ nm, expecting $\Delta = \pi$ and $\Delta' = 0$ as reported in [70]. For plates azimuthal structuring, we choose the $\alpha_m = \pi/(8|m|)$ as sector angular width and $\pi/8$ as orientation step angle between neighboring sectors. Structuring is achieved by direct ion beam lithography considering set of fundamental and high-order topological charges $|m| = \{1/2, 5\}$, using 500 μm thick BK7 glass as a substrate for metal deposition. The protocol of fabrication consists of a few steps. First, the substrate are sonicated in an acetone and a methanol bath, which removes contamination and enhances adhesion for metal deposition. Then, 5 nm thick layer of chromium is deposited on substrates by electron beam evaporation, which serves as adhesion layer. Next, substrates are magnetron sputtered with 300 nm thick gold layer using physical vapor deposition system (K.J. Lesker, AXXIS) without changing vacuum level. Finally, the coated substrates are patterned by ion beam lithography system (Raith, IonLiNE), using focused Ga^+ ions to mill designed structures.

The resulting structures that correspond to topological charges $m = -1/2$ and $m = -5$ are shown in Fig. 4.8 obtained by scanning electron microscopy observations. This allows confirming accurate fabrication regarding planned geometrical design.

4.3.2 Structural characterization

To assess the optical axis space-variant distribution of fabricated structures experimentally, we have implemented an optical characterization technique using Stokes parameters. Introduced in section 1.1, Stokes parameters allow retrieving the output beam polarization ellipse azimuth angle $\Phi(x, y)$ experimentally, hence the optical axis distribution of the structures. Indeed, $\Phi(x, y)$ differs from the local optical axis orientation angle ψ by $\pm 45°$ angle, the sign depends on the value of the birefringent phase delay and on the incident polarization handedness. In practice, following Ref. [27], we have measured Stokes parameters by placing a linear polarizer at the output of the sample and recording the output intensity profile for four orientations of the polarizer, with 45° step. The map of the output

beam polarization ellipse azimuth angle $\Phi(x, y)$ is then evaluated from the maps of Stokes parameters S_1 and S_2, following the expression $\tan(2\Phi) = S_2/S_1$. The results are depicted in Fig. 4.9 for the structures with topological charges $m = -1/2$ (a) and $m = -5$ (b). Panels in Fig. 4.9 correspond to the optical axis dependence on the polar angle φ noting that by construction we have $\Phi(\varphi) - \Phi(0) = \psi(\varphi) - \psi(0)$, while insets correspond to in-plane spatial distribution of optical axes. Experimental data is compared to expectations in panels of Fig. 4.9 where red curves correspond to ideal design behavior.

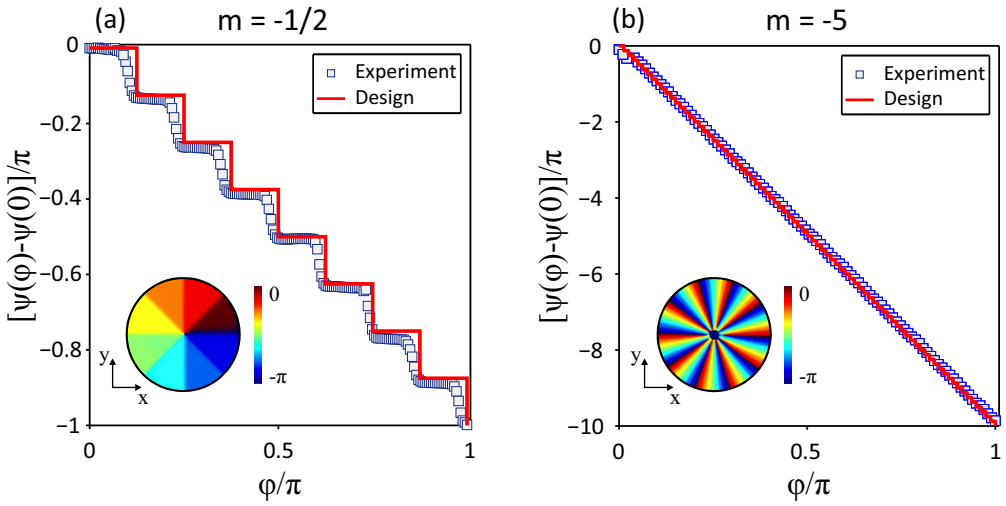

FIGURE 4.9: Experimental retrieval of segmented metallic q-plates optical axis in-plane distributions for $m = -1/2$ (a) and $m = -5$ (b). Panels show local optical axis orientation angle dependence on azimuthal angle φ, insets correspond to the optical axis orientation profiles in the plane of the samples.

4.3.3 Optical Performance

We have explored the optical performances of the fabricated spin-orbit couplers using a focused circularly polarized (with helicity σ) Gaussian laser beam at 532 nm wavelength normally incident on the structures. In order to ensure that all the incident beam is processed by the structure, we choose a beam waist radius $w \simeq 25$ μm and place the sample at the focal plane of the used lens. Such a configuration is associated with a beam divergence angle $\theta \simeq 0.4°$, which implies that our paraxial description remains valid.

The generated vortex is experimentally selected by placing after the sample a quarter-wave plate followed by a linear polarizer oriented at $-\sigma 45°$ from the quarter-wave pate slow axis (circular polarizer). By doing so, we select the contra-circularly polarized component of the output field, which is the one carrying the optical vortex. Indeed, doughnut shape intensity transverse profile is observed for both

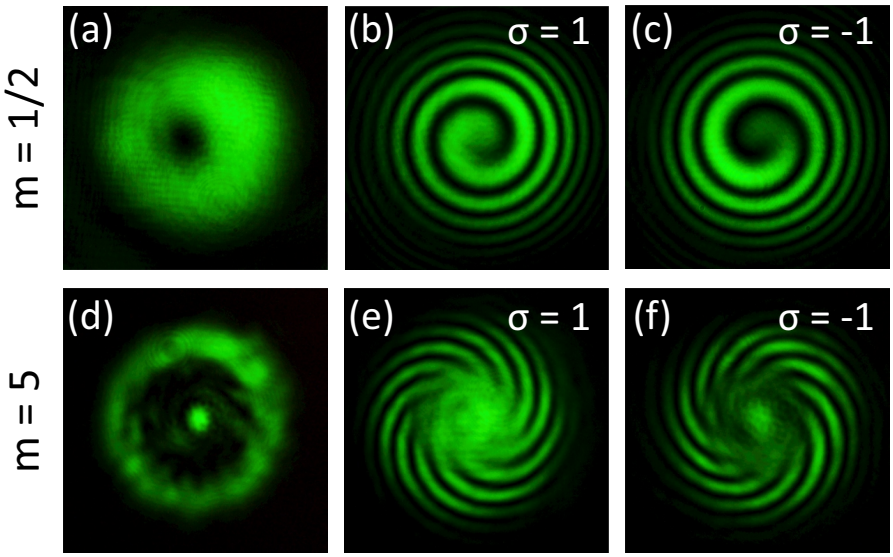

FIGURE 4.10: (a,d) Optical vortex intensity transverse distributions for metallic plates with topological charge $m = 1/2$ and $m = 5$ illuminated by normally incident circularly polarized Gaussian beam with wavelength 532 nm. (b,c,e,f) Interference patterns that result from the coherent superposition of output vortex beam and collinear reference Gaussian beam. Observed right- and left-handed $2m$-arm spiraling patterns correspond to optical phase singularity with topological charge $\ell = 2\sigma m$. Panels (b,e) and (c,f) correspond to the two orthogonal circular polarization states for the input beam, for $m = 1/2$ (b,c) and $m = 5$ (e,f).

$m = 1/2$ (Fig. 4.10(a)), and $m = 5$ (Fig. 4.10(d)). Note that the on-axis hot spot observed for $m = 5$ (Fig. 4.10(d)), is associated with the unstructured central part in the case of high-order structuring, as shown in Fig. 4.8 (e). Figure 4.10(b,c,e,f) displays transverse interference distributions that correspond to coherent on-axis superposition of the output beam and reference Gaussian beam with parallel circular polarization to that of output beam, for both $\sigma = \pm 1$ incident helicity. This allows confirming the proper generation of optical vortices with $2\sigma m$ topological charge, as expected.

Then, the performance of optical vortex generation process is evaluated following the definition of purity that can be expressed as

$$\eta = \frac{P_{-\sigma}}{P_{+\sigma} + P_{-\sigma}} . \tag{4.12}$$

where, $P_{\pm\sigma}$ stand for powers of $\pm\sigma$-polarized output beam components, which are selected placing quarter-wave plate and following polarizer respectively oriented at $\pm\sigma 45°$ from quarter-wave plate slow axis. We measure $\eta \simeq 78$ % for all fabricated structures, independently from m. Such values is a bit less than expected $\eta = 1$ value in absence of dichroism ($\Delta' = 0$), assuming $\Delta = \pi$. To clarify it, we recall that purity η actually depends on both Δ and Δ' (see Eq. (4.4)) and we decided to measure Δ' directly. To do so, we have fabricated a 100×100 μm^2 square shaped area of straight grating structure with identical thickness, grating period, and slit width as the spin-orbit elements. Considered structure allows to determine dichroic parameter Δ' by measuring $P_{\parallel,\perp}$ powers of the output beam after placing linear polarizer with parallel and perpendicular orientation to the grating wavevector, namely, $\Delta' = -\log[(P_\parallel/P_\perp)^{1/2}]$). Then, from the knowledge of η and Δ' Eq. (4.4) gives access to the birefringent phase retardation Δ. We find $\Delta' \simeq 0.05$, which implies $\Delta \simeq 0.7\pi$ or 1.3π. This indicates that fabricated spin-orbit couplers are associated with 30 % difference from expectations, which is probably related with non-uniformity of the slit width due to the thermal drifting associated with long fabrication time (few hours for each structure).

In addition, we have explored the optical vortex generation performances of fabricated structures in the visible domain, using a halogen lamp as a polychromatic source of illumination. To this aim, in practice we have prepared secondary white

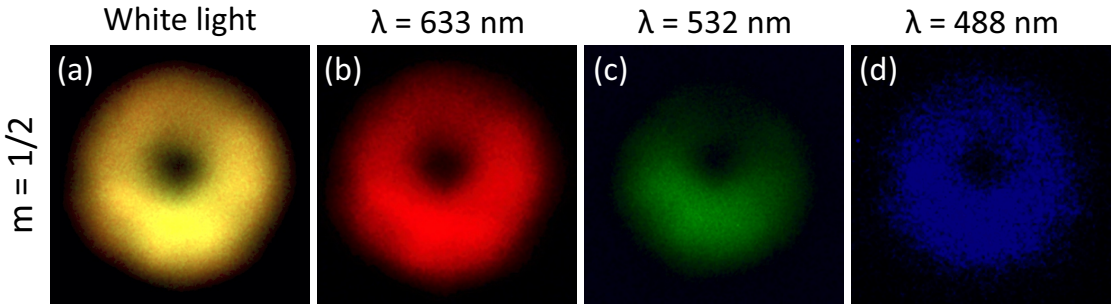

FIGURE 4.11: Polychromatic optical vortex intensity transverse distribution generated using halogen lamp, and its three, red, green, and blue, spectral components selected using bandpass filters with 3 nm half-maximum transmission spectrum; for the structure with the topological charge $m = 1/2$.

light source by using 100 μm diameter pinhole that allows increasing the spatial coherence of the source, which ensures better formation of the characteristic doughnut intensity pattern of vortex beam. Resulting white light vortex beam intensity transverse distribution is shown in Fig.4.11(a) for $m = 1/2$. Using a set of bandpass filters with 3 nm full-width half-maximum transmission spectrum, the underlying spectral vortex content can be also revealed, see Fig.4.11(b,c,d). We note that yellowish color of polychromatic vortex in Fig.4.11(a) implies dispersive character of the gold metallic structure, which suggests wavelength-dependent optical vortex generation process. In order to evaluate the wavelength dependence of the spin-orbit coupling, we have measured the purity η of the process in the visible domain, by using a set of nine bandpass filters. The filters have 10 nm full-width half-maximum transmission spectrum and their central wavelength values are separated by 50 nm. In addition, we have measured purity with using 532 nm wavelength interference filter of 3 nm full-width half maximum transmission spectrum, which gives a purity value $\eta \simeq 70$ % that is a bit lower than the one measured with 532 nm laser illumination. The results for $m = 1/2$ are presented in Fig. 4.12, which demonstrates a rather broadband behavior of the fabricated structures.

In order to appreciate the obtained experimental results, we have reviewed discussions in literature related to use of metallic plates as spin-orbital couplers in the visible domain. First, referring again to Ref. [70], whose numerical developments we have used to design our structures, a quantitative comparison is not straightforward,

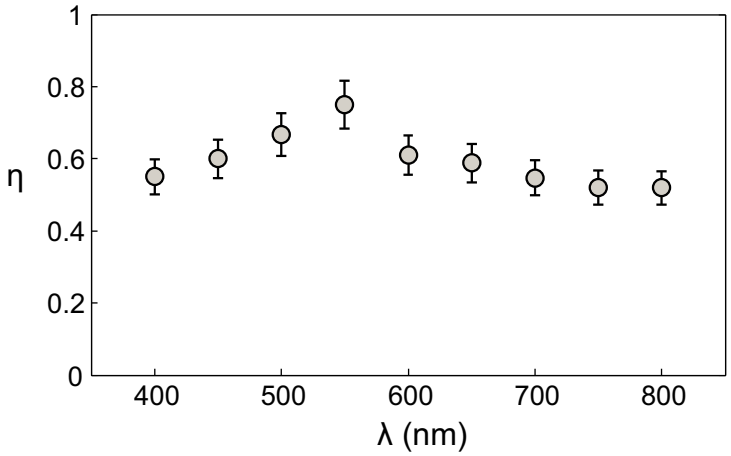

FIGURE 4.12: Optical vortex purity η dependence on wavelength in the visible domain for the structure with topological charge $m = 1/2$.

since there is lack of precise information in this reference. Next, apart from using space-variant gratings, there are several studies on spin-orbit induced optical beam tailoring with use of plasmonic nano-antennas of various shapes [71, 72, 73]. In particular, in Ref. [43], the authors report on L-shape nanoantennas using metallic structures in the near infrared range $760 - 790$ nm. Initially, they have reported on purity experimental value $\eta \simeq 10$ %, and recently they reported on improvement up to 35 % in Ref. [44]. In this context, our experimental attempts to fabricate optical vortex generators in visible domain thus appear fairly good. From the theoretical point of view, we also note a recent study that deals with optical vortex generation using metallic nanowires at 1.5 μm wavelength. Indeed, authors of Ref. [74] report on purity of 90 % for topological charge $\ell = 1$ and 97 % for topological charge $\ell = 2$.

4.3.4 Towards optomechanics experiment

With the aim at using fabricated metallic samples in an optomechanical experiment, let us first evaluate their expected rotation frequency. Recalling the general analysis reported in section 4.1, steady state rotation frequency and input beam helicity product of spin-orbit element immersed in liquid equals

$$\sigma f = f_0 \left[\mathcal{A} + 2\mathcal{T}\eta(1-m)\right] , \tag{4.13}$$

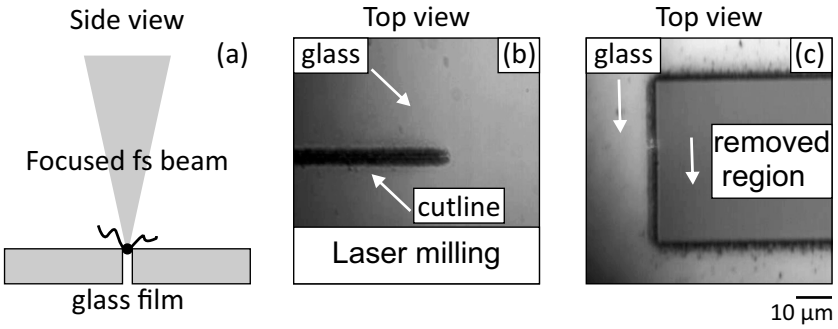

FIGURE 4.13: Practical illustration of possible femtosecond laser milling of glass layers. (a) Sketch of laser cut in glass film using focused laser beam. (b) Image of laser straight cut line. (c) Glass film after removal of glass region.

with $f_0 = \frac{3P}{64\pi\omega\mu R^3}$. Considering gold average reflectance equal $\mathcal{R} \simeq 80$ % (neglecting difference between parallel and perpendicular components) at operating wavelength 532 nm and experimentally measured transmission $\mathcal{T} = 2$ %, we obtain $\sigma f \simeq 7$ mHz for sample $m = 1/2$ and $\sigma f = 2$ mHz for sample $m = 5$, under $P = 1$ W illumination. Although the magnitude of latter frequencies corresponds to a few revolutions of samples within one hour of experimental time, $\sigma f > 0$ corresponds to the "right-handed" situation. Metallic microstructures are therefore not obvious candidates towards direct observation of optical torque reversal. An option could be to increase the topological charge m, indeed similar sample fabricated with topological charge with $m = 10$ would be associated with $\sigma f = -4$ mHz, hence being a "left-handed" situation. Nevertheless, the release of the sample from substrate is another technical difficulty that can not be ignored within the metallic approach. Indeed, recalling that gold layer is in practice coated on 100 μm-thick glass substrate, which is equal to the diameter of the samples, and assuming that "structure + substrate" can be cut and released, one would obtain a bulky cylinder, instead of disk shape. This will cause serious mechanical stability issues for optical manipulation. To handle such technical difficulties an approach could be to consider thinner substrates such as $1 - 10$ μm thick commercially available glass films. This would allow to obtain disk like samples, that could be cut through glass film using femtosecond laser milling. An example of such process using 10 μm glass film is illustrated in Fig. 4.13. However, in view of the anticipated technical difficulties, we decided to move to a purely dielectric option discussed this in the next section.

4.4 Dielectric approach at the micrometer scale

In contrast to metallic samples, dielectric samples are associated with substantially higher transmittance and can be fabricated using ultra thin substrates, which allows to design smaller structures with disk shape geometry. In practice we used silicon nitride membranes that are commercially available with various thicknesses in the typical range of 100 – 1000 nm. To design spin-orbit dielectric structures, we have used the same approach as for metallic structures, namely space-variant optical axis structuring from subwavelength gratings, using discrete azimuthal orientation of the optical axis. We opted for 500 nm thick membranes, which results from a trade-off between fabrication time and vortex generation purity. Indeed, thicker structures are preferable to reach optimal half-wave plate phase retardation condition while this is at expense of fabrication time and reproducibility. Practically, the slit dept is limited to 350 nm height in order to preserve mechanical integrity of the structures. Subwavelength grating period is $\Lambda = 500$ nm and slit width is $W = 250$ nm. Figure 4.14 shows scanning electron microscopy image of fabricated structure with topological charge $m = -5$, and radius $R = 15$ μm.

Expected product σf accessible with the latter design, preserving our assumptions of incident circularly polarized plane wave, dielectric structure immersed in

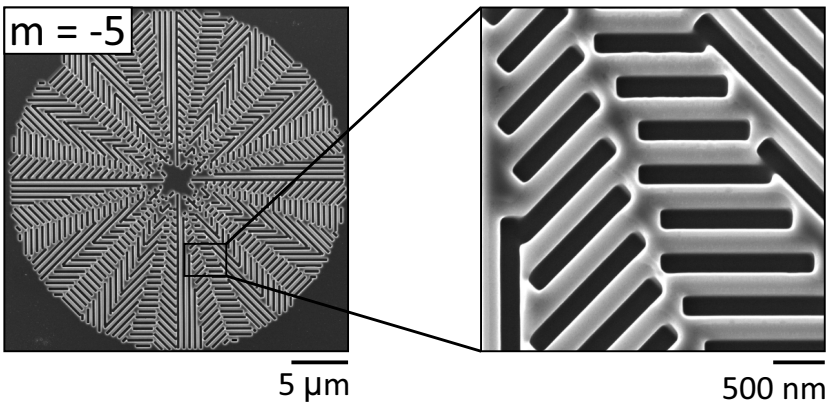

FIGURE 4.14: Scanning electron microscopy images of fabricated dielectric space-variant birefringent plate with topological charge $m = -5$ red fabricated using ion-beam lithography.

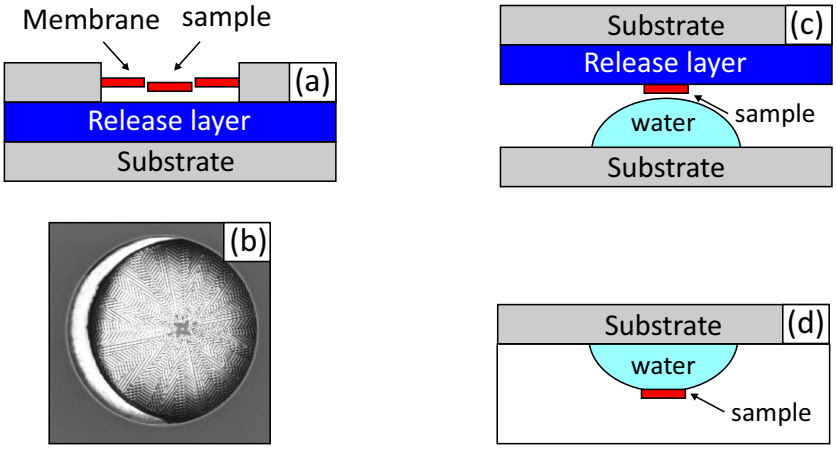

FIGURE 4.15: Illustration of the release protocol of dielectric structures. (a) Membrane (red) deposited on the top of a water-releasable layer (blue) is milled through (white slits) thus leaving spin-orbit element to fall on the release layer. (b) Top view of sample after milling leaving membrane. (c) Once release layer is in contact with water, water droplet forms on the sample substrate and releases the spinner. (c) Side view of final stage that leads to self-centered microstructure suspended by water droplet.

water, and assuming ideal transmission $\mathcal{T} = 1$, hence $\mathcal{R} = 0$ and $\mathcal{A} = 0$, expresses as

$$\sigma f = 2 f_0 \eta (1 - m) \,. \tag{4.14}$$

The remaining parameter in order to determine the gauge light-induced rotation rate is thus the purity η, which requires the knowledge of the form birefringence. The latter is estimated from Ref. [2] that gives for our design $W/\Lambda = 1/2$

$$n_\parallel - n_\perp = \frac{(n_1 + n_2)(n_2 - n_1)^2}{2(n_1^2 + n_2^2)} \tag{4.15}$$

where n_1 and n_2 are refractive indices of the nanomembrane and surrounding medium (here water). Thus, using $n_1 = 2$ for silicon nitride and $n_2 = 1.3$ for water Eq. (4.15) gives a form birefringence $n_\parallel - n_\perp = 0.4$, hence $\eta = \sin^2\left[\frac{\pi}{\lambda}(n_\parallel - n_\perp)L\right] = 0.5$ taking $\lambda = 532$ nm and $L = 350$ nm, $n_1 + n_2 = n_\perp + n_\parallel$. With such parameters, we obtain for $m = |5|$ $\sigma f = -18$ mHz for incident power $P = 100$ mW. Observation of optical torque reversal thus seems accessible in practice.

To perform the optomechanical experiment the last step is to consider release of structure in water. For this purpose, the implementation of dielectric structures

allows using the following protocol. First, the membrane is coated with polyvinyl alcohol polymer that acts as water-releasable layer, which dries after a few minutes forming a solid layer. Then, the structure is milled through from the membrane that is deposited on the top of the latter layer, and subsequently fall and stick on after full cut. Finally, once release layer is brought with contact with water it dissolves leaving structure to fall by gravity. The process is sketched in Fig 4.15. By doing so, one thus obtain self-centered spin-orbit micro-element free to rotate and the aimed optomechanical experiment can be performed. Indeed, such actions are under continued development at present day.

Conclusion

In this work we focused our attention on the mechanical consequences of the fact that light may carry spin and orbital angular momentum. Namely, the appearance of an optical torque enabling angular displacement or rotation of objects; in practice, micro-objects. In chapter 1, we reported on different kinds of situations involving optical spin or/and orbital angular momentum that could be partly or totally transferred to matter. In particular, we have addressed the situation when spin and angular momentum contributions are coupled as light interacts with matter, which is the so called spin-orbit interaction of light. Such spin-orbit optomechanics, which has not been experimentally addressed so far, is actually the main point of this work that encompass the prediction of counterintuitive optomechanical phenomenon, the optical torque reversal, and experimental realizations of it as explored in chapters 2, 3 and 4 from various point of view.

In chapter 2, we proposed and reported on the first direct observation of optical spin-orbit radiation torque using liquid crystal topological defects as optical spin-orbit couplers. Polarimetric analysis of light induced liquid crystal molecular ordering allows us to unambiguously identify the predicted effects whatever the helicity of the driving light field and the topological charges ±1 of the chosen liquid crystal defects (umbilics) [75]. However, since the observations were limited to unit charge material topological defects, the most striking of our predictions that is the existing of optical torque reversal was not accessible to our experiments. An attempt was made using another kind of defects whose charge could be possibly higher enough to ensure observation of optical torque reversal. However, fundamental limitations have been unveiled and further investigations were carried out by changing the material system.

This has been explored in chapter 3 with the introduction of solid state space-variant birefringent nanostructured glass slabs. Actually, we succeeded to demon-

strate experimentally the mechanical manifestation of optical torque reversal with such media. The difficulty associated with the use of macroscopic samples was circumvented by looking at the effect of matter on light instead of detecting the effect of light on matter. Experimentally this has been achieved by introducing rotational Doppler frequency shift experiments relying on one- or two-beam, on-axis or off-axis interferometric approaches to measure frequency shift. A quantitative thorough study firmly confirmed all our predictions [76, 77]. Nevertheless, such indirect approach left open the challenge that consists of the direct observation of optical torque reversal.

The challenge has been taken on in chapter 4, where analysis of required realistic experimental conditions is performed. This led us to consider miniaturized spin-orbit elements with possibly high topological charge values. From this knowledge, fabrication and characterization of millimeter and micrometer scale spin-orbit optical elements has been performed [78, 79]. As this thesis work ends, we can say that the suitable candidate has been eventually defined and it is likely that the direct observation of optical torque reversal will be reported soon, in the framework of an ongoing thesis work.

Bibliography

[1] B. Saleh and M. Teich, *Fundametals of photonics 2nd edition* (Wiley, 2007).

[2] M. Born and E. Wolf, *Principles of optics* (Cambridge University Press, 1999).

[3] J. Poynting, "The wave motion of revolving shaft, and a suggestion as to angular momentum in a beam of circularly polarised light", *Proceedings of Royal Society A* 560 (1909).

[4] A. T. O'Neil, I. MacVicar, L. Allen, and M. J. Padgett, "Intrinsic and extrinsic nature of the orbital angular momentum of a light beam", *Physical Review Letters* **88**, 053601 (2002).

[5] L. Allen, M. W. Beijersbergen, R. J. C. Spreeuw, and J. P. Woerdman, "Orbital angular momentum of light and the transformation of Laguerre-Gaussian laser modes", *Physical Review A* **45**, 8185 (1992).

[6] M. S. Soskin and M. Vasnetsov, "Singular optics", *Progress in Optics* **42**, 219 (2001).

[7] L. Allen, S. M. Barnett, and M. J. Padgett, *Optical angular momentum* (Institute of Physics Publishing, 2003).

[8] M. E. J. Friese, T. A. Nieminen, N. R. Heckenberg, and H. Rubinsztein-Dunlop, "Optical torque controlled by elliptical polarization", *Optics Letters* **23**, 1 (1998).

[9] H. He, M. E. J. Friese, N. R. Heckenberg, and H. Rubinsztein-Dunlop, "Direct observation of transfer of angular momentum to absorptive

particles from a laser beam with a phase singularity", *Physical Review Letters* **75**, 826 (1995).

[10] M. E. J. Friese, J. Enger, H. Rubinsztein-Dunlop, and N. R. Heckenberg, "Optical angular-momentum transfer to trapped absorbing particles", *Physical Review A* **54**, 1593 (1996).

[11] N. B. Simpson, K. Dholakia, L. Allen, and M. J. Padgett, "Mechanical equivalence of spin and orbital angular momentum of light: an optical spanner", *Optics Letters* **22**, 52 (1997).

[12] R. A. Beth, "Mechanical detection and measurement of the angular momentum of light", *Physical Review* **50**, 115 (1936).

[13] E. Santamato, B. Daino, M. Romagnoli, M. Settembre, and Y. R. Shen, "Collective rotation of molecules driven by the angular momentum of light in a nematic film", *Physical Review Letters* **57**, 2423 (1986).

[14] E. Santamato, G. Abbate, P. Maddalena, L. Marrucci, and Y. R. Shen, "Laser-induced nonlinear dynamics in a nematic liquid-crystal film", *Physical Review Letters* **64**, 1377 (1990).

[15] M. E. J. Friese, N. R. Heckenberg, and H. Rubinsztein-Dunlop, "Optical alignment and spinning of laser-trapped microscopic particles", *Nature* **397**, 348 (1998).

[16] E. Santamato, A. Sasso, B. Piccirillo, and A. Vella, "Optical angular momentum transfer to transparent isotropic particles using laser beam carrying zero average angular momentum", *Optics Express* **10**, 871 (2002).

[17] B. Piccirillo, C. Toscano, F. Vetrano, and E. Santamato, "Orbital and spin photon angular momentum transfer in liquid crystals", *Physical Review Letters* **86**, 2285 (2001).

[18] V. Garcés-Chávez, K. Volke-Sepulveda, S. Chávez-Cerda, W. Sibbett, and K. Dholakia, "Transfer of orbital angular momentum to an optically trapped low-index particle", *Physical Review A* **66**, 063402 (2002).

[19] G. Biener, A. Niv, V. Kleiner, and E. Hasman, "Formation of helical beams by use of Pancharatnam-Berry phase optical elements", *Optics Letters* **27**, 1875 (2002).

[20] M. Stalder and M. Schadt, "Linearly polarized light with axial symmetry generated by liquid-crystal polarization converters", *Optics Letters* **21**, 1948 (1996).

[21] L. Marrucci, C. Manzo, and D. Paparo, "Optical spin-to-orbital angular momentum conversion in inhomogeneous anisotropic media", *Physical Review Letters* **96**, 163905 (2006).

[22] S. C. McEldowney, D. M. Shemo, and R. A. Chipman, "Vortex retarders produced from photo-aligned liquid crystal polymers", *Optics Express* **16**, 7295 (2008).

[23] S.-W. Ko, Y.-Y. Tzeng, C.-L. Ting, A. Y.-G. Fuh, and T.-H. Lin, "Axially symmetric liquid crystal devices based on double-side photo-alignment", *Optics Express* **16**, 19643 (2008).

[24] S. Nersisyan, N. Tabiryan, D. M. Steeves, and B. R. Kimball, "Fabrication of liquid crystal polymer axial waveplates for UV-IR wavelengths", *Optics Express* **17**, 11926 (2009).

[25] S. Slussarenko, A. Murauski, T. Du, V. Chigrinov, L. Marrucci, and E. Santamato, "Tunable liquid crystal q-plates with arbitrary topological charge", *Optics Express* **19**, 4085 (2011).

[26] S. R. Nersisyan, N. V. Tabiryan, D. Mawet, and E. Serabyn, "Improving vector vortex waveplates for high-contrast coronagraphy", *Optics Express* **21**, 8205 (2013).

[27] E. Brasselet, N. Murazawa, H. Misawa, and S. Juodkazis, "Optical vortices from liquid crystal droplets", *Physical Review Letters* **103**, 103903 (2009).

[28] B. Son *et al.*, "Optical vortex arrays from smectic liquid crystals", *Optics Express* **22**, 4699 (2014).

[29] C. Loussert, U. Delabre, and E. Brasselet, "Manipulating the orbital angular momentum of light at the micron scale with nematic disclinations in a liquid crystal film", *Physical Review Letters* **111**, 037802 (2013).

[30] E. Brasselet and C. Loussert, "Electrically controlled topological defects in liquid crystals as tunable spin-orbit encoders for photons", *Optics Letters* **36**, 719 (2011).

[31] E. Brasselet, "Tunable optical vortex arrays from a single nematic topological defect", *Physical Review Letters* **108**, 087801 (2012).

[32] P. Pieranski, B. Yang, L. J. Burtz, A. Camu, and F. Simonetti, "Generation of umbilics by magnets and flows", *Liquid Crystals* **40**, 1593 (2013).

[33] E. Brasselet, Y. Izdebskaya, V. Shvedov, A. S. Desyatnikov, W. Krolikowski, and Y. S. Kivshar, "Dynamics of optical spin-orbit coupling in uniaxial crystals", *Optics Letters* **34**, 1021 (2009).

[34] E. Brasselet, "Singular optical reordering of liquid crystals using Gaussian beams", *Journal of Optics* **12**, 124005 (2010).

[35] E. Brasselet, "Spin-orbit optical cross-phase-modulation", *Physical Review A* **82**, 063836 (2010).

[36] M. E. Ketara and E. Brasselet, "Observation of self-induced optical vortex precession", *Physical Review Letters* **110**, 233603 (2013).

[37] B. Yang and E. Brasselet, "Arbitrary vortex arrays realized from optical winding of frustrated chiral liquid crystals", *Journal of Optics* **15**, 044021 (2013).

[38] R. Barboza, U. Bortolozzo, G. Assanto, E. Vidal-Henriquez, M. G. Clerc, and S. Residori, "Vortex induction via anisotropy stabilized light-matter interaction", *Physical Review Letters* **109**, 143901 (2012).

[39] R. Barboza, U. Bortolozzo, G. Assanto, E. Vidal-Henriquez, M. G. Clerc, and S. Residori, "Harnessing optical vortex lattices in nematic liquid crystals", *Physical Review Letters* **111**, 093902 (2013).

[40] I. Budagovsky, A. Zolotḱo, D. Korshunov, M. Smayev, S. Shvetsov, and M. Barnik, "Generation of spiral dislocation of wave front in absorbing nematic liquid crystal", *Optics and Spectroscopy* **119**, 280 (2015).

[41] M. Beresna, M. Gecevčius, P. G. Kazansky, and T. Gertus, "Radially polarized optical vortex converter created by femtosecond laser nanostructuring of glass", *Applied Physics Letters* **98**, 201101 (2011).

[42] Y. Shimotsuma, P. G. Kazansky, J. Qiu, and K. Hirao, "Self-organized nanogratings in glass irradiated by ultrashort light pulses", *Physical Review Letters* **91**, 247405 (2003).

[43] F. Bouchard, I. De Leon, S. A. Schulz, J. Upham, E. Karimi, and R. W. Boyd, "Optical spin-to-orbital angular momentum conversion in ultra-thin metasurfaces with arbitrary topological charges", *Applied Physics Letters* **105**, 101905 (2014).

[44] S. A. Schulz, J. Upham, F. Bouchard, I. De Leon, E. Karimi, and R. W. Boyd, dans *Photonic Crystals and Plasmonics*, Proceedings 6th International Conference of Metamaterials (Meta, New York, USA, 2015), p. 721.

[45] N. V. Tabiryan, A. V. Sukhov, and B. Y. Zel'dovich, "Orientational optical nonlinearity of liquid crystals", *Molecular Crystals and Liquid Crystals* **136**, 1 (1986).

[46] E. Brasselet, "Singular optical manipulation of birefringent elastic media using nonsingular beams", *Optics Letters* **34**, 3229 (2009).

[47] P. G. de Gennes and J. Prost, *The physics of liquid crystals* (Clarendon Press, 1995).

[48] P. Oswald and P. Pieransky, *Nematic and cholesteric liquid crystals: concepts and physical properties Illustrated by Experiments* (Taylor & Francis, CRC, Boca Raton, FL, 2005).

[49] R. B. Meyer, "Point disclinations at a nematic-isotropic liquid interface", *Molecular Crystals and Liquid Crystals* **16**, 355 (1972).

[50] A. Saupe, "Disclinations and properties of the director field in nematic and cholesteric liquid crystals", *Molecular Crystals and Liquid Crystals* **21**, 211 (1973).

[51] A. Rapini, "Umbilics: static properties and shear-induced displacements", *Journal of Physics* **34**, 629 (1973).

[52] I. Dierking, O. Marshall, J. Wright, and N. Bulleid, "Annihilation dynamics of umbilical defects in nematic liquid crystals under applied electric fields", *Physical Review E* **71**, 061709 (2005).

[53] M. G. Clerc, E. Vidal-Henriquez, J. D. Davila, and M. Kowalczyk, "Symmetry breaking of nematic umbilical defects through an amplitude equation", *Physical Review E* **90**, 012507 (2014).

[54] I. Jánossy, "Electromagnetic torque and force in axially symmetric liquid-crystal droplets", *Optics Letters* **33**, 2371 (2008).

[55] N. Murazawa, S. Juodkazis, and H. Misawa, "Characterization of bipolar and radial nematic liquid crystal droplets using laser-tweezers", *Journal of Physics D: Applied Physics* **38**, 2923 (2005).

[56] E. Brasselet, N. Murazawa, S. Juodkazis, and H. Misawa, "Statics and dynamics of radial nematic liquid-crystal droplets manipulated by laser tweezers", *Physical Review E* **77**, 041704 (2008).

[57] S. Chandrasekhar, *Liquid Crystals* (Cambridge University Press, Cambridge, England, 1992).

[58] N. V. Madhusudana and R. Pratibha, "Studies on high strength defects in nematic liquid crystals?", *Molecular Crystals and Liquid Crystals* **103**, 31 (1983).

[59] E. Santamato, G. Abbate, P. Maddalena, and Y. R. Shen, "Optically induced twist Fréedericksz transitions in planar-aligned nematic liquid crystals", *Physical Review A* **36**, 2389 (1987).

[60] S. Lee, Y.Roichman, and D. Grier, "Optical solenoid beams", *Optics Express* **18**, 6988 (2010).

[61] S. Sukhov and A. Dogariu, "On the concept of "tractor beams"", *Optics Letters* **35**, 3847 (2010).

[62] A. Dogariu, S. Sukhov, and J. J. Saenz, "Optically induced "negative forces"", *Nature Photonics* **7**, 24 (2013).

[63] S. H. Simpson and S. Hanna, "Optical trapping of spheroidal particles in Gaussian beams", *Journal of the Optical Society of America A* **24**, 430 (2007).

[64] Y. Shimotsuma, P. G. Kazansky, J. Qiu, and K. Hirao, "Self-organized nanogratings in glass irradiated by ultrashort light pulses", *Physical Review Letters* **91**, 247405 (2003).

[65] P. J. Allen, "A radiation torque experiment", *American Journal of Physics* **34**, 1185 (1966).

[66] B. A. Garetz, "Angular doppler effect", *Journal of the Optical Society of America* **71**, 609 (1981).

[67] C. Maurer, A. Jesacher, S. Fürhapter, S. Bernet, and M. Ritsch-Marte, "Tailoring of arbitrary optical vector beams", *New Journal of Physics* **9**, 78 (2007).

[68] E. Brasselet, "Optical angular momentum conversion in a nanoslit: comment", *Optics Letters* **38**, 3890 (2013).

[69] V. G. Levich, *Physicochemical hydrodynamics* (Englewood Cliffs, N.J., Prentice-Hall, 1962).

[70] K. Iwami, M. Ishii, Y. Kuramochi, K. Ida, and N. Umeda, "Ultrasmall radial polarizer array based on patterned plasmonic nanoslits", *Applied Physics Letters* **101**, 161119 (2012).

[71] N. Yu and F. Capasso, "Flat optics with designer metasurfaces", *Nature Materials* **13**, 139 (2014).

[72] Y. Zhao, X.-X. Liu, and A. Alù, "Recent advances on optical metasurfaces", *Journal of Optics* **16**, 123001 (2014).

[73] P. Genevet and F. Capasso, "Holographic optical metasurfaces: a review of current progress", *Reports on Progress in Physics* **78**, 024401 (2015).

[74] C. Huang, X. Chen, A. O. Oladipo, N. C. Panoiu, and F. Ye, "Generation of subwavelength plasmonic nanovortices via helically corrugated metallic nanowires", *Scientific Reports* **5**, 13089 (2015).

[75] D. Hakobyan and E. Brasselet, "Optomechanics of liquid crystal defects", (in preparation).

[76] D. Hakobyan and E. Brasselet, "Left-handed optical radiation torque", *Nature Photonics* **8**, 610 (2014).

[77] D. Hakobyan and E. Brasselet, "Optical torque reversal and spin-orbit rotational Doppler shift experiments", *Optics Express* **23**, 31230 (2015).

[78] D. Hakobyan, H. Magallanes, G. Seniutinas, S. Juodkazis, and E. Brasselet, "Tailoring orbital angular momentum of light in the visible domain with metallic metasurfaces", *Advanced Optical Materials* **4**, 306 (2016).

[79] G. Seniutinas, G. Gervinskas, J. Anguita, D. Hakobyan, E. Brasselet, and S. Juodkazis, "Nano-proximity direct ion beam writing", *Nanofabrication* **2**, 54 (2016).